MATERIALS APPROACHES FOR TRANSPARENT ELECTRONICS

Chukwudi E. Iheomamere

Dissertation Prepared for the Degree of

DOCTOR OF PHILOSOPHY

UNIVERSITY OF NORTH TEXAS

December 2021

APPROVED:

Nigel Shepherd, Major Professor
Andrey Voevodin, Committee Member
Richard F. Reidy, Committee Member
Mohamed El Bouanani, Committee Member
Francis D'Souza, Committee Member
Vijay Vasudevan, Chair of the Department of Materials Science and Engineering
Hanchen Huang, Dean of the College of Engineering
Victor Prybutok, Dean of the Toulouse Graduate School

Iheomamere, Chukwudi E. *Materials Approaches for Transparent Electronics*. Doctor of Philosophy (Material Science and Engineering), December 2021, 87 pp., 10 tables, 52 figures, numbered chapter references.

This dissertation tested the hypothesis that energy transferred from a plasma or plume can be used to optimize the structure, chemistry, topography, optical and electrical properties of pulsed laser deposited and sputtered thin-films of ZnO, *a*-BO_xN_y, and few layer 2H-WS_2 for transparent electronics devices fabricated without substrate heating or with low substrate heating. Thus, the approach would be compatible with low-temperature, flexible/bendable substrates. Proof of this concept was demonstrated by first optimizing the processing-structure-properties correlations then showing switching from accumulation to inversion in ITO/*a*-BO_xN_y/ZnO and ITO/*a*-BO_xN_y/2H-WS_2 transparent MIS capacitors fabricated using the stated processes. The growth processes involved the optimization of the individual materials followed by growing the multilayer stacks to form MIS structures. ZnO was selected because of its wide bandgap that is transparent over the visible range, WS_2 was selected because in few-layer form it is transparent, and *a*-BO_xN_y was used as the gate insulator because of its reported atomic smoothness and low dangling bond concentration. The measured semiconductor-insulator interfacial trap properties fall in the range reported in the literature for SiO_2/Si MOS structures.

X-ray photoelectron spectroscopy (XPS), Hall, photoluminescence, UV-Vis absorption, and X-ray diffraction (XRD) measurements investigated the low-temperature synthesis of ZnO. All films are nanocrystalline with the (002) XRD planes becoming more prominent in films grown with lower RF power or higher pressure. Low power or high chamber pressure during RF magnetron sputtering resulted in a slower growth rate and lower energetic conditions at the substrate. Stoichiometry improved with RF power. The measurements show a decrease in carrier concentration from 6.9×10^{19} cm^{-3} to 1.4×10^{19} cm^{-3} as power increased from 40 W to 120 W, and

an increase in carrier concentration from 2.6×10^{19} cm^{-3} to 8.6×10^{19} cm^{-3} as the deposition pressure increased from 3 to 9 mTorr. The data indicates that in the range of conditions used, bonding, stoichiometry, and film formation are governed by energy transfer from the plasma to the growing film.

XPS characterizations, electrical measurements, and atomic force microscopy (AFM) measurements reveal an increase in oxygen concentration, improved dielectric breakdown, and improved surface topography in *a*-BO_xN_y films as deposition pressure increased. The maximum breakdown strength obtained was ~8 $MVcm^{-1}$, which is comparable to a-BN. Metal-Insulator-Metal (MIM) structures of *a*-BO_xN_y grown at 10 and 15 mTorr suggest a combination of field-enhanced Schottky emission and Frenkel-Poole emission are likely transport mechanisms in *a*-BO_xN_y. In comparison, better fitted data was gotten for field enhanced Schottky emission which suggests the more dominant mechanism. The static dielectric constant range is 3.26 – 3.58 for 10 and 15 mTorr films. Spectroscopic ellipsometry and UV-Vis spectroscopy measured a bandgap of 3.9 eV for 15 mTorr grown *a*-BO_xN_y.

2H-WS_2 films were grown on both quartz and *a*-BO_xN_y which revealed that the XRD (002) planes became more prominent as substrate temperature increased to 400 ºC. AFM shows nano-grains at lower growth pressure. Increasing the growth pressure to 1 Torr resulted in the formation of larger particles. XPS chemical analysis reveals improved sulfur to tungsten ratios as pressure increased. Sulfur deficient films were n-type, whereas sulfur rich conditions produced p-type films.

Frequency dependent C-V and G-V measurements revealed an interface trap concentration (N_{it}) of 7.3×10^{10} cm^{-2} and interface state density (N_{ss}) of 7.5×10^{12} $eV^{-1}cm^{-2}$ for the transparent ITO/*a*-BO_xN_y/ZnO MIS structures, and approximately 2 V was required to switch the *a*-BO_xN_y/ZnO interface from accumulation to inversion. Using 2H-WS_2 as the channel material, the ITO/*a*-BO_xN_y/2H-WS_2 required approximately 4 V to switch from inversion to accumulation

in both n and p-channel MIS structures. Interface trap concentrations (N_{it}) of 1.6×10^{12} cm^{-2} and 3.2×10^{10} cm^{-2}, and interface state densities (N_{ss}) of 1.6×10^{12} $eV^{-1}cm^{-2}$ and 6.5×10^{12} $eV^{-1}cm^{-2}$ were calculated for n and p-channel 2H-WS_2 MIS structures, respectively. The data from these studies validate the hypothesis and demonstrate the potential of ZnO, *a*-BO_xN_y, and few layer 2H-WS_2 for transparent electronics.

ACKNOWLEDGMENTS

Greatest gratitude to God almighty for the blessings of grace and perseverance to see the completion of this dissertation. Gratitude to Prof. Nigel Shepherd for being a wonderful mentor, Prof. Andrey Voevodin for his intellectual contributions and collaborative works during the processes. Grateful to Prof. Richard F. Reidy for unlimited access to his laboratory and Ph.D. committee members Profs. Mohamed El Bouanani and Francis D'Souza for the advice offered. Special acknowledgment to my past and present teammates: Dr. Urmilaben P. Rathod, Mr. Corey Arnold, Mr. Renzo Sanchez, and Mrs. Shambhavi Sakri. Dr. David Garrett and Mr. Craig Collins for their technical supports when I was building the PVD systems for this work. I appreciate encouraging messages from family and friends while pursuing this work. Special gratitude to my lovely daughter Ms. Amari Chika Iheomamere, for understanding the importance of this work.

TABLE OF CONTENTS

Page

LIST OF TABLES

Page

LIST OF FIGURES

Page

CHAPTER 1

INTRODUCTION

1.1 Motivation

With evolving interest in consumer electronics, electronic technology has transitioned from button keys to touchscreen interaction in cellphones, and from bulky display units to flat-screen units [1]. The goal is for industries to design visually appealing products that meet improved device performance. For example, Samsung in 2010 released her largest 3D 70" Ultra Definition (UD) using oxide semiconductor, and Apple's IGZO display panels used in iPad Air and iPhones. Next-generation consumer electronic devices project towards complete see-through. By sandwiching wide bandgap materials on transparent substrates [2]; varied electronic and optical properties/applications are achievable through manipulation of charge transport/injection or propagation of electromagnetic waves through structures. Wide bandgaps transparent conducting oxides like ITO and ZnO [3,4] as channel material, and highly insulating materials with high or low dielectric constants can be structured for different electronic applications [5,6]. Important requirements in the selection of materials for these heterostructures are cost and availability, chemical and interfacial stability of the structure, and ease of fabrication. ZnO, *a*-BO_xN_y, and a few-layered WS_2 meet the stated requirement.

Graphene show impressive electrical properties [7] and mechanical flexibility for flexible electronics [8,9]; however, its lacking intrinsic bandgap limits its application as a semiconductor material in 2D miniaturized electronic and optoelectronic applications. For example, the inability to switch off graphene-based transistors [10]. To solve the challenging problem of graphene in electronics; the study of transition metal dichalcogenides TMDCs advanced new opportunities for nanometer-scale electronic devices. Because most TMDCs transition from indirect to direct

bandgap as thickness reaches a few to single layer thickness, this makes 2D TMDCs potential candidates in electronic and optoelectronic applications without altering electronic properties [11]. Although TMDCs' bandgap values start around the red wavelength regions, the thickness of a few to single layers allows for penetration of higher photon energy thereby making these materials transmissive and potentially applicable in thin films transparent electronics [12].

Physical vapor deposition (PVD) technique ushers the benefit of processing time management, minimal impurities, large-area synthesis, thin film uniformity, and variability in process condition (i.e. temperature, pressure, etc). The stated benefits of PVD form the basic requirement of economic large-scale synthesis of materials studies in this work. This work employs low-temperature processing of ITO/*a*-BO_xN_y/ZnO/Ag and ITO/*a*-BO_xN_y/WS_2/Ag MIS structure for transparent transistors. A rectifying current/voltage measurement and a capacitance switch from accumulation to depletion and inversion is the measured figure of merit to prove the hypothesis.

1.2 Contribution of Dissertation

Listed below are the contributions of this work:

- Effect of sputtering power and pressure in low-temperature RF magnetron sputtering of ZnO
- The effect of intrinsic non-stoichiometric defects in optical and electrical properties of low-temperature RF magnetron sputtered ZnO.
- The effect of chamber pressure on surface morphology, chemistry and dielectric breakdown in RF magnetron synthesized a-BOxNy thin films.
- Effect of substrate temperature on structure XRD preferred orientation of pulsed laser deposited 2H-WS2.
- Effect of argon chamber pressure on the structure, surface topography, structure, and chemistry of pulsed laser deposited 2H-WS2.

- Electric analysis of transparent ITO/a-BOxNy/ZnO/Ag and ITO/a-BOxNy/WS2/Ag MIS capacitors.

1.3 Thesis Outline

The design of this work is shown in Figure 1.1. Chapter 1 covers the motivation/hypothesis, the overall contribution of this work to the scientific community, and the outline of this work.

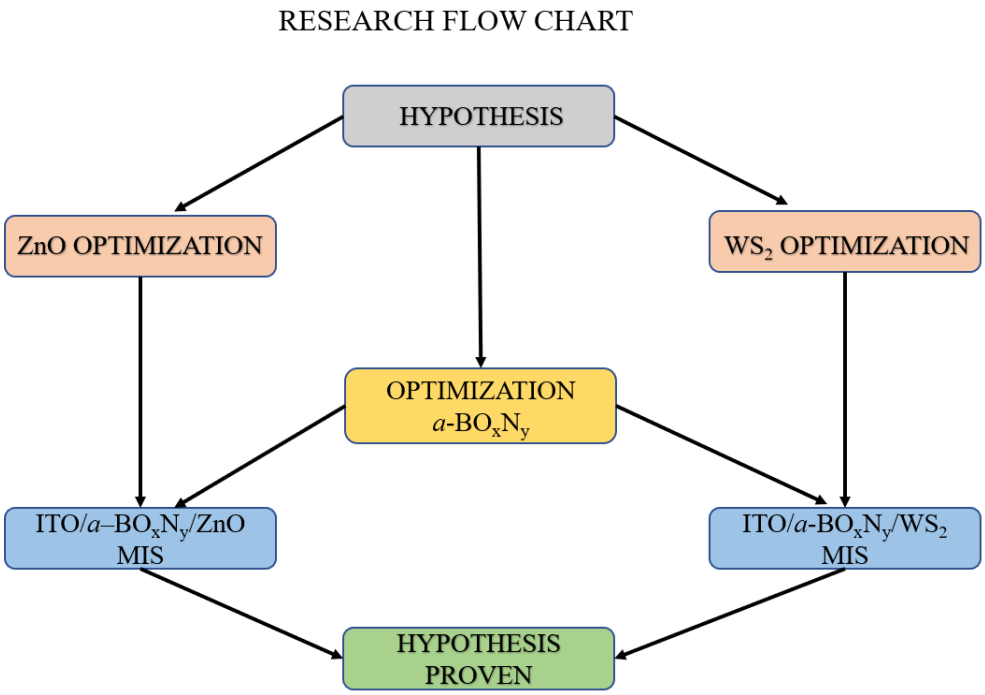

Figure 1.1: Research Flow Chart

Chapter 2 discusses what has already been reported in the literature. This includes literature reviews in transistors, materials of studies ZnO, BN base materials, and Transition metal dichalcogenides with emphasis on WS_2. Chapter 3 introduces the fundamentals of processing and characterization methods used for the growth materials studies in this work, details the experimental method of the processes used in the growth and fabrications of materials and heterostructures studies here. Chapter 4 covers the result of low-temperature growth of ZnO.

Chapter 5 covers the result of the low-temperature growth of *a*-BO_xN_y. Chapter 6 covers the result of the low-temperature growth of WS_2. Chapter 7 covers the result of the electrical characterization and comparisons of ITO/*a*-BO_xN_y/ZnO/Ag and ITO/*a*-BO_xN_y/WS_2/Ag MIS capacitors. Chapter 8 covers the conclusion section and recommended future work.

1.4 Hypothesis

Energy transferred from a plasma or plume during low temperature RF magnetron sputtering and pulsed laser deposition can be used to optimize film structure, chemistry, topography, optical and electrical properties of ZnO, *a*-BO_xN_y, and a few layers 2H-WS_2 for transparent electronics applications. Prove of this concept is demonstrated by showing a capacitance-voltage switch from accumulation to inversion in ITO/*a*-BO_xN_y/ZnO and ITO/*a*-BO_xN_y/WS_2 MIS Capacitors fabricated using the stated physical vapor technique processes.

1.5 Dissertation Objective

The goal of this work is to characterize materials using spectroscopy, microscopy, optical and electrical characterizations for analysis of:

- RF magnetron sputtered to ZnO thin films as potential channel materials for transparent transistors.
- PLD processed few layers 2H-WS_2 as a channel material for transparent transistors.
- RF magnetron sputtered *a*-BO_xN_y as a dielectric insulator for transparent electronic
- ITO/*a*-BO_xN_y/ZnO/Ag and ITO/ *a*-BO_xN_y /WS_2/Ag MIS structures for transparent electronics.

1.6 References

[1] W. John F., Transparent electronics, Science (80-.). 300 (n.d.) 1245–1246.

[2] W. J.F., Transparent electronics: Schottky barrier and heterojunction considerations, Thin Solid Films. 516 (n.d.) 1755–1764. https://doi.org/10.1016/j.tsf.2007.06.164.

[3] H. H., O. H., O. M., U. K., H. M., Frontier of transparent conductive oxide thin films, Vacuum. 66 (n.d.) 419–425.

[4] L. S., L. A., K. S., L. S., G. C., K. G., Optical and structural properties of ZnO for transparent electronics, Thin Solid Films. 516 (n.d.) 1345–1349. https://doi.org/10.1016/j.tsf.2007.03.171.

[5] Z. Yong-Hui, M. Zeng-Xia, L. Hui-Li, D. Xiao-Long, Review of flexible and transparent thin-film transistors based on zinc oxide and related materials, Chinese Phys. B. 26 (n.d.) 047307. https://doi.org/10.1088/1674-1056/26/4/047307.

[6] F. Elvira, B. Pedro, M. Rodrigo, Oxide semiconductor thin-film transistors: a review of recent advances, Adv. Mater. 24 (n.d.) 2945–2986.

[7] N. Kostya S., G. Andre K., M. Sergei V., J. De-eng, Z. Yanshui, D. Sergey V., G. Irina V., F. Alexandr A., Electric field effect in atomically thin carbon films, Science (80-.). 306 (n.d.) 666–669.

[8] H. Tae-Hee, K. Hobeom, K. Sung-Joo, L. Tae-Woo, Graphene-based flexible electronic devices, Mater. Sci. Eng. R Reports. 118 (n.d.) 1–43. https://doi.org/10.1016/j.mser.2017.05.001.

[9] Y. Rui, L. Yu-Qing, H. Yi-Long, H. Dong-Dong, Z. Yong-Lai, Y. Zheng, Laser Fabrication of Graphene-Based Flexible Electronics, Adv. Mater. 32 (n.d.) 1901981. https://doi.org/10.1002/adma.201901981.

[10] S. Frank, Graphene transistors, Nat. Nanotechnol. 5 (n.d.) 487–496.

[11] M. Stephen J., W. Robert M., Atomically-thin layered films for device applications based upon 2D TMDC materials, Thin Solid Films. 616 (n.d.) 482–501. https://doi.org/10.1016/j.tsf.2016.08.068.

[12] J. Nanotechnology, W. Tang, R. Ss, R. Nm, Madridge Electronic & Optical properties of transition-metal dichalcogenides, 2 (2017) 59–65. https://doi.org/10.18689/mjnn.2017-110.

CHAPTER 2

LITERATURE REVIEW

2.1 Overview of Thin Film Transistors (TFT) and MIS/MOS Capacitor

Although Julius Lilienfeld in 1926 patented the first Field Effect Transistor (FET), it was not until the 1930s that researchers started looking at possibilities of solid-state transistors. With the first Bell Lab's official solid-state transistor dated back to 1948, they reported the successful work of John Bardeen and Walter Brattain. Bardeen and Brattain's work (investigating semiconductor surface states) preceded the fabrication of the MOSFET and later the first TFT was fabricated in 1962 [1]. 1973 welcomed the first TFT Liquid Display Crystal LCD [2]. The 1990s introduced organic semiconductors as channel layers, with electron mobilities comparable to a-Si [3], which was an innovation amongst other works that is the motivation behind flexible devices. Recent studies are demonstrating TFT transitioning to completely transparent electronics.

TFTs are typically structured as top-gated or bottom-gated with subdivisions of top or bottom electrodes are shown in Figure 2.1.

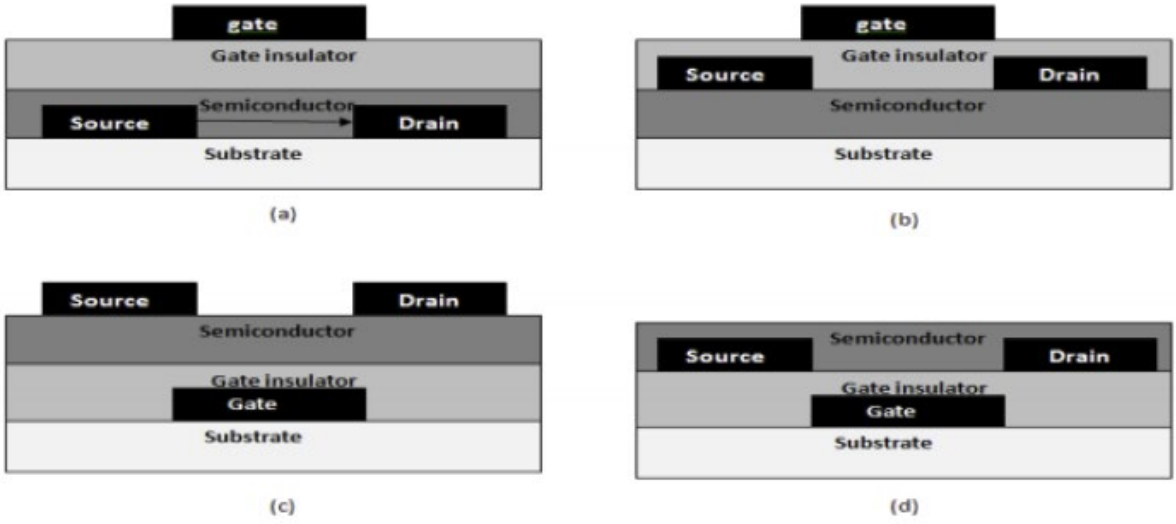

Figure 2.1: TFT Structure: (a) Top-gate, bottom contacts, (b) Top-gate, Top contacts, (c) Bottom-gate, Top contacts and (d) Bottom-gate, bottom contacts [4,5].

The major differences between a MOSFET and TFT include their fabrication processes; MOSFET technology includes layered fabrication process, e.g. ion implantation, layer growth from substrate i.e. thermal oxides, deposition, etc. while TFT requires just depositions. Although MOSFET fabrication offers better crystallinity than TFT; TFT can be fabricated on any substrate. After the first TFT-LCD, TFT applications have broadened to commercially available flat-panel X-ray detectors, resistive pressure sensors used in touch screens, electronic-skin sensors, and TFT biosensors, etc [6–8]. Metal-insulator/oxides-semiconductor (MOS/MIS) capacitors (Figure 2.2) are the building blocks of MOSFET and TFT transistors. A simple MIS capacitor comprises a sandwich of an insulator between a metallic conducting gate and a semiconductor. The semiconductor layer must have an ohmic connection to the power supply.

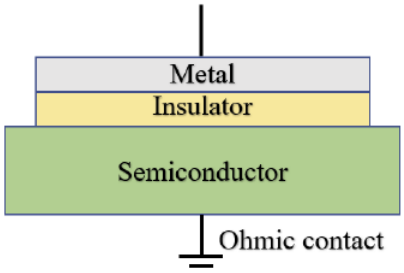

Figure 2.2: MIS Capacitor Structure

To simplify the fundamental principles of an MIS capacitor, let us consider a simple parallel plate capacitor. The parallel plate capacitor is described as two conducting metallic/metal-like plates separated by an insulator. With the left and right plate bias positively and negatively respectively, each corresponding plate will store equal charges with opposite sign conventions. The equations of a parallel plate capacitor can be summarized from Eqs. 2.1 to 2.3.

$$Q = CV \qquad \text{Eq. 2.1}$$

$$C = \frac{\varepsilon}{t} \qquad \text{Eq. 2.2}$$

$$\xi = \frac{V}{t} \qquad \text{Eq. 2.3}$$

where Q is the charge stored, C is the capacitance of the insulator, V is the voltage applied across plates, t is the thickness of the insulating layer, ε is the permittivity of the insulator and ξ is electric field across plates.

The MIS capacitor is identical to a simple parallel plate capacitor with a difference of replacing one of the metal plates with a semiconductor. Substituting one end of a metal plate with semiconductor results in variable capacitance behavior as voltage changes across the MIS capacitor. As the magnitude of the voltage across the MIS structure changes from positive to negative and vice-versa, depending on the carrier type of the semiconductor, capacitance regions change from accumulation of charge to depletion and further to inversion of charge. This is clearly illustrated with a simple band diagram (Figure 2.3).

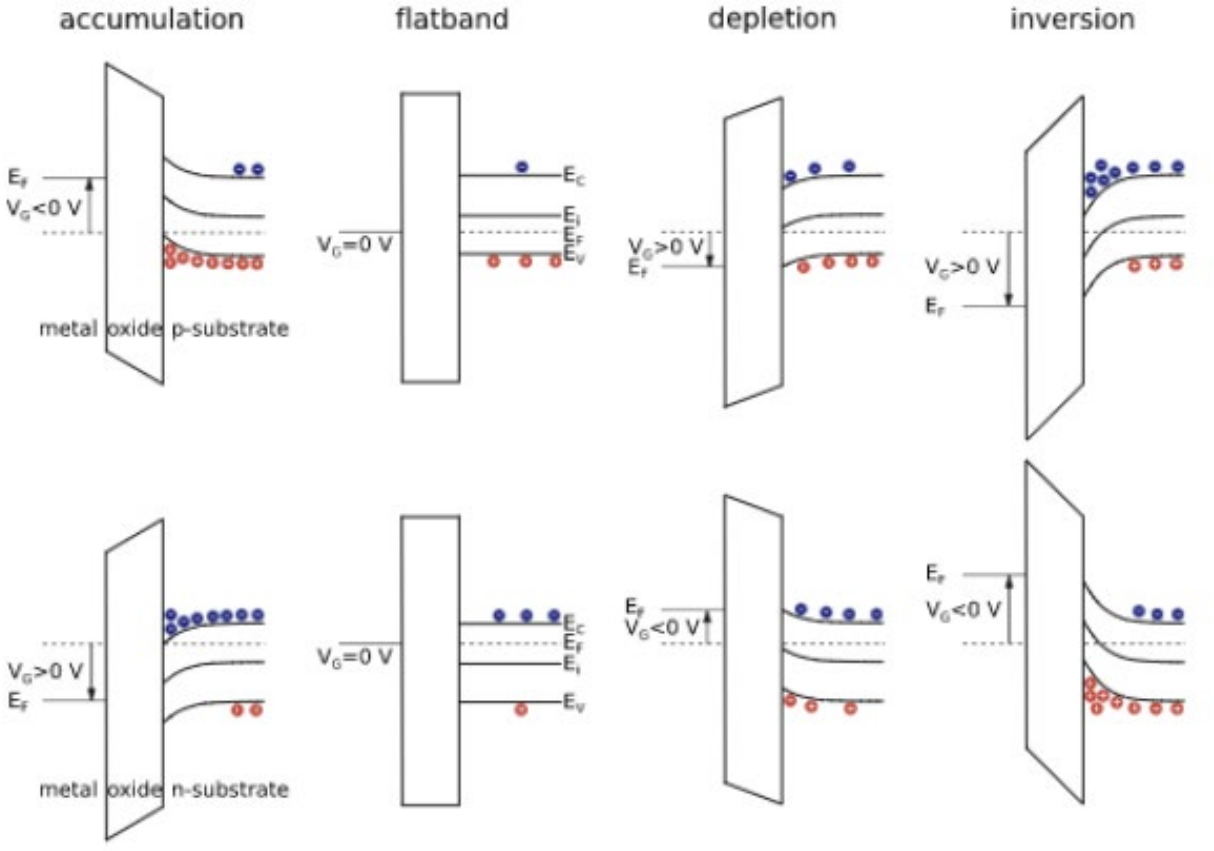

Figure 2.3: Band structure of MOS/MIS capacitor. Image adapted from [https://www.iue.tuwien.ac.at/phd/ullmann/3.html]

A typical MIS structure behaves like the parallel plate capacitor stated above. For an MIS structure with a p-type substrate; with a negative voltage applied the metal plate results in negative charges accumulated at the metal plate and an equally positive charge on the semiconductor. As illustrated in the band diagram in Figure 2.3, the semiconductor band bends downward away from the interface. This region is called the accumulation region and capacitance in the accumulation region results from the insulator as described by equation 2.2.

Applying a positive voltage to the metal plate of an MIS structure with a p-type substrate also results in a positive charge at the metal, and as a result of the generated negative charge at the semiconductor, the semiconductor region begins to deplete charge at the interface. This is the depletion region and the width of the depletion increases with an increase of positive voltage on the metal plate. Capacitance in the depletion region is typically lower than that of the accumulation; this is because of the contribution of depletion width and insulator thickness resulting in a total increase in thickness. The capacitance during depletion of an MIS structure is a series of insulator capacitance and depletion layer capacitance of the semiconductor: $\frac{1}{C} = \frac{1}{C_{ins}} + \frac{1}{C_{dep}}$. At a point when the semiconductor region is completely depleted, a negative charge is accumulated at the interface of the insulated/semiconductor. This region is termed Inversion and the p-type semiconductor behaves as an n-type and vice-versa.

The maximum depletion layer thickness can be calculated from equations 2.4 and 2.5 by approximating the surface potential (ϕ_s) at the interface of the insulator and semiconductor equal two times the Fermi potential (ϕ_f).

$$\phi_f = V_t \ln\left(\frac{N_d}{N_i}\right) \qquad \text{Eq. 2.4}$$

$$Wmax = \left\{\frac{2\epsilon_s (2\phi_f)}{eN_d}\right\}^{0.5} \qquad \text{Eq. 2.5}$$

where: *Wmax*: Space Charge Layer, $\phi_f = (E_f - E_i)$: Fermi Potential, N_d: Extrinsic Carrier Concentration, N_i: Intrinsic Carrier Concentration, ϵ_s: permittivity of semiconductor, e: charge of an electron, V_t: Thermal Voltage = $k_B T/e$, where k_B: Boltzmann Constant and T is Temperature in Kelvin.

2.2 Capacitance: Voltage Characteristics of an MIS Capacitor

The capacitance is measured as a function of applied DC voltage and is obtained as a combination of a small signal AC voltage alongside applied DC voltage.

Figure 2.4 depicts capacitance-voltage characteristics of an MIS structure with a p-type semiconductor. As stated above, both accumulation and inversion region capacitance are insulator capacitance, but on the other hand, a CV measurement is significantly affected by the frequency of the AC voltage across the MIS structure. Typically, high frequency affects the response of change in the inversion layer.

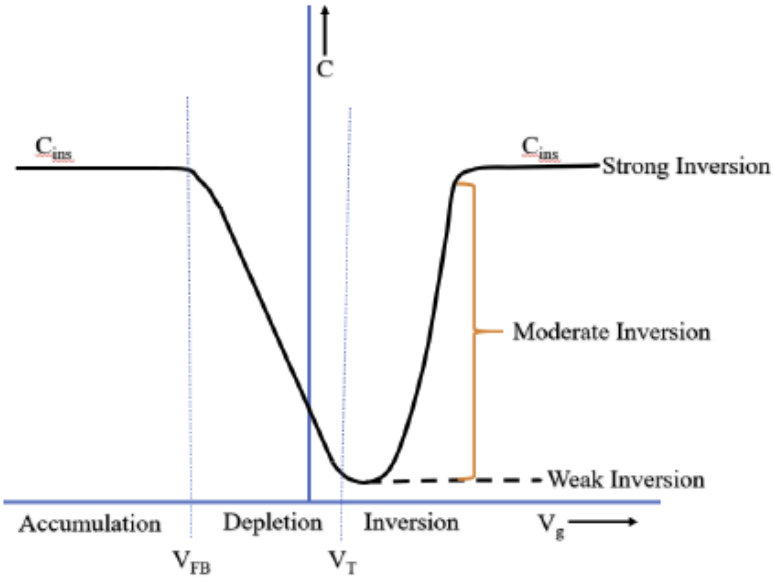

Figure 2.4: Capacitance-Voltage plot of MIS-structure (p-type semiconductor).

In a real MIS structure, undesired charges within the insulator or at the insulator-semiconductor interface can be observed by CV measurement. These charges are either fixed

oxide charges or interface trapped charges. Fixed oxide charges are known to shift the position of threshold voltage the flat-band voltage of an MIS capacitor, but are not a function of applied gate bias. Because fixed oxide charges are independent of gate voltage, the shape of a CV curve with fixed oxide charges remains the same after every voltage shift. The flat-band voltage will shift to a positive charge for a negative fixed oxide and vice versa. Because of the discontinuity of the periodicity of the semiconductor structure at the interface of the insulator-semiconductor, electronic states also known as interface states are generated. The interface states can allow charge transport to and from the semiconductor resulting in possible trapped charges. The interface states are a function of the gate bias and will result in a distorted CV curve.

2.3 Materials of Study

This work has investigated PVD processes of ZnO, WS_2, and *a*-BO_xN_y. Semiconducting ZnO and BN-based insulators have bandgaps large enough to transmit visible light. BN-based insulators are atomically smooth and free of dangling bonds. In WS_2, the growth of a few layers with thickness less than the penetration depth will transmit visible wavelengths. Overall the above-stated materials are chemically stable; therefore, device stability is promising. ZnO has a direct bandgap transition while BN-based compound and WS_2 attain direct band transition as thickness approach monolayer. Cost plays a big role in material selection and device fabrication.

2.4 ZnO as Transparent Conducting Oxides (TCO); Towards Transparent Transistors

ZnO occurs in polymorphs of wurtzite [9], zinc blend [10], or rocksalt [11] as depicted in Figure 2.5. With the wurtzite structure being the more favorable thermodynamically stable polymorph at atmospheric conditions. The wurtzite structure has a hexagonal unit cell and belongs to the $p6_3mc$ space group. ZnO Zinc blende structure ($F\bar{4}3m$ space group) can be achieved by growth on a cubic substrate while rocksalt structure with space group Fm3m can be

achieved by increased hydrostatic pressure during growth high as 10 GPa [12] and also a reported wurtzite-rocksalt transition upon compression [13]. The metastable rocksalt structure reverses back to wurtzite upon decompression [14,15]. ZnO is a direct bandgap material with a bandgap value of ~3.3 eV and a 60 meV excitonic binding energy shows good potential in optoelectronic applications [16]. Experimental band structure of wurtzite ZnO has been reported using various emission techniques [17,18]. In their work, Preston et al have used angular-dependent resonant x-ray emission spectroscopy to study O k-edge band structure of wurtzite ZnO [19] shown (Figure 2.6). Advantages of ZnO as a direct wide bandgap material include low noise generation in electronic devices, it can sustain large electric field without joule heating, and also high power device applications. This is associated with the diminished phonon activities during electron transition from the valence to the conduction band.

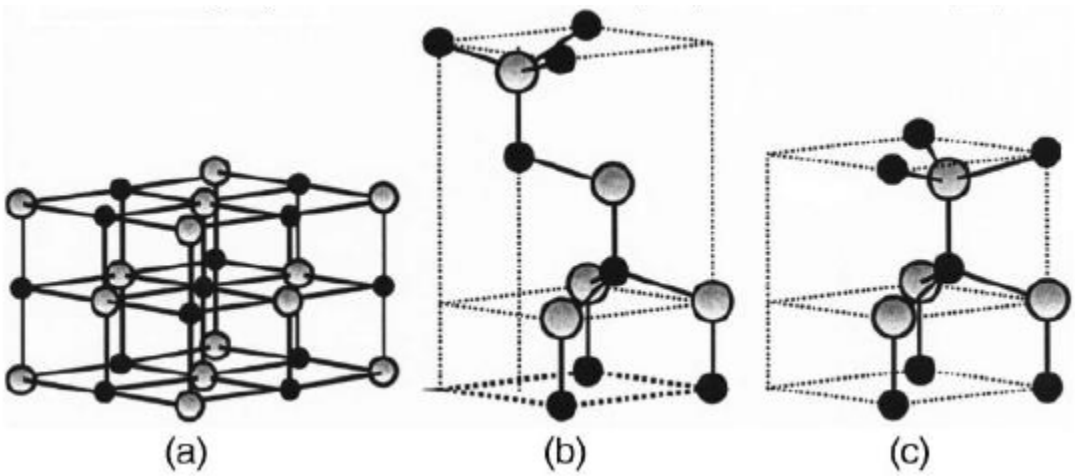

Figure 2.5: ZnO Polymorphs: (a) Rocksalt, (b) Zinc blende, (c) Wurtzite structure [20].

For transistor applications, to achieve significantly good response time, the semiconductor needs to have high carrier mobility. Electron mobility could be hampered by various scattering mechanisms: Phonon scattering which is a result of charge interacting with lattice vibration, piezoelectric scattering which are fields generated from strain within the phonon of the semiconductor structure, ionized impurity scattering which is association

coulombic deflection of impurity carriers, grain boundary scattering, and electron-electron scattering. It is expected that improved crystallinity, controlled doping or impurity levels play a significant role in improving mobility. Carrier mobility is also affected by temperature is because elevated device temperature can generate hot electrons from the valence to the conduction band of the semiconductor. Hot electrons increase the probability of electron to electron collision thereby diminishing the mobility.

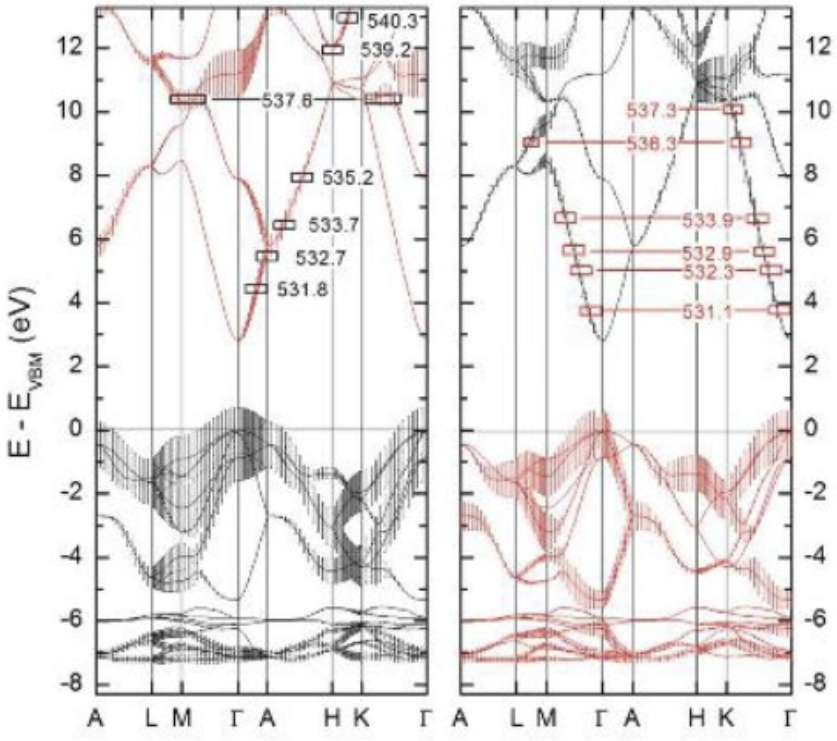

Figure 2.6: Wurtzite ZnO Band structure [19].

Growth of ZnO thin films has been reported using MBE [21], CVD [22], PLD [23], sol-gel [24], and sputtering [25,26]. It is important to note that the choice of the substrate plays a significant role in the crystallinity of the ZnO films. The major consideration in substrate selection includes lattice matching, crystalline structure, and thermal expansivity as compared to the growth film. A significant lattice mismatch will result in induced strain in the growing film. Table 2.1 reports the lattice properties and thermal conductivities of various substrates in ZnO

film growth. And to demonstrate the significance of lattice-matched substrate in ZnO growth, Ghosh and Basak were able to show in their work that GaN the lowest lattice mismatch substrate, produced ZnO films with better crystallinity, preferred oriented (002), and low electrical resistivity [27].

Table 2.1: Lattice parameter of ZnO as compared to the various substrate [20].

Material	Crystal structure	Lattice parameters a (Å) c (Å)	Lattice mismatch (%)	Thermal-expansion coefficient, α (K^{-1}) α_a (10^{-6}) α_c (10^{-6})
ZnO	Hexagonal	3.252 5.213	···	2.9 4.75
GaN	Hexagonal	3.189 5.185	1.8	5.17 4.55
AlN	Hexagonal	3.112 4.980	4.5	5.3 4.2
α-Al_2O_3	Hexagonal	4.757 12.983	(18.4% after 30° in-plane rotation)	7.3 8.1
6H-SiC	Hexagonal	3.080 15.117	3.5	4.2 4.68
Si	Cubic	5.430	40.1	3.59
$ScAlMgO_4$	Hexagonal	3.246 25.195	0.09	
GaAs	Cubic	5.652	42.4	6.0

ZnO in its natural state shows n-type carrier conduction, this is because of the presence of intrinsic non-stoichiometric defects like Zn interstitials (Zn_i) or oxygen vacancies (V_o). The presence of both intrinsic and extrinsic defects results in an increased ionized impurity scattering mechanism, thereby resulting in the reduction of carrier mobility. By reducing the number of point defects during growth in MBE grew ZnO films, Tsukazaki et al demonstrated significantly high mobility of 5000 $cm^2\ V^{-1}\ s^{-1}$ at 50 K and 440 $cm^2\ V^{-1}\ s^{-1}$ at 300 K for ZnO films with residual carrier concentrated of 4×10^{14} and 9×10^{15} cm^{-3} [28]. These values are much higher than the reported values of pure single crystal ZnO [29].

X-ray photoelectron spectroscopy (XPS) and photoluminescence spectroscopy (PL) are widely used techniques for chemical analysis and to study defect states in ZnO. XPS and PL analysis can be used to explain the electronic behavior in ZnO. As shown in Figure 2.7 (a) and (b) XPS spectra of ZnO. The core elemental scan contains spectra of O 1s and Zn 2p. The Zn 2p is split into $2p_{3/2}$ and $2p_{1/2}$ with a 22.97 eV separation [30]. Hsieh et al studied the chemistry of rf sputtered ZnO films on a SiO_2/Si substrate [31]. They have performed post-annealing between 600 – 900ºC at a 75 mTorr pressure with varying oxygen concentrations (0, 20, and 100%). Using Mg k_α as the x-ray source and XPS spectra calibrated to 284.6 eV binding energy for C 1s, they studied deconvoluted constituents in an O 1s spectrum.

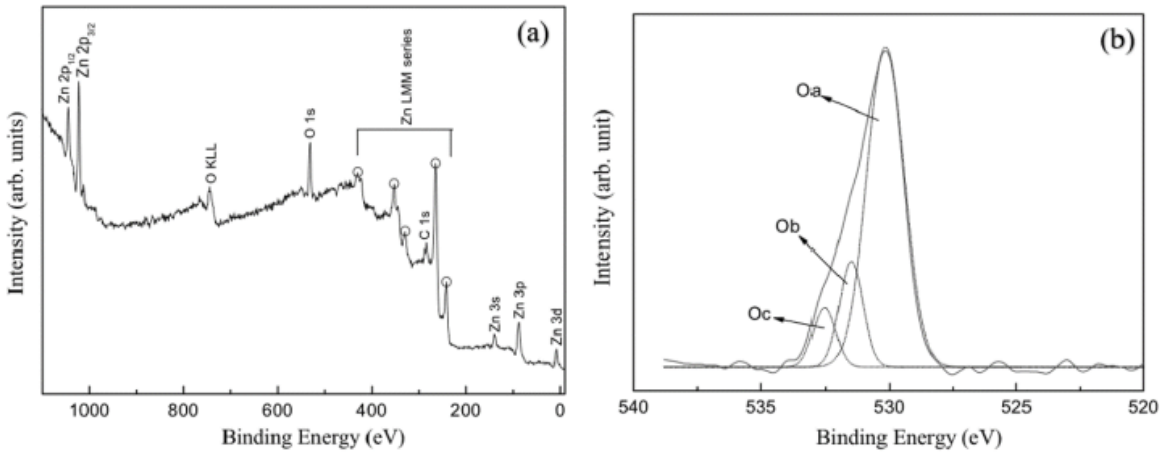

Figure 2.7: XPS Data for ZnO: (a) Survey spectrum, (b) O 1s spectrum [31].

Region Oa with binding energy 530.2 eV is attributed to O^{-2} oxidation state that is stoichiometrically bonded to Zn in ZnO, Ob with 531.4 eV was attributed to an O^{-2} oxidation state in the oxygen deficit region, while Oc with energy at 532.6 was attributed to O in OH groups. XPS data are similar to hydrothermally grown ZnO nanowires [32]. For sol-gel prepared ZnO nanoparticles, the XPS spectrum also shows asymmetry with a 527.8 eV region corresponding to stoichiometrically bonded O in ZnO and a 530.2 eV region corresponding to an oxygen deficit region in ZnO [33]. The presences of OH and C impurities, the non-stoichiometric

and stoichiometric regions result in asymmetry in O 1s XPS spectrum. The consistent asymmetry in the O 1s spectrum is arguably a significant influence in n-type conduction in undoped ZnO [34]. Under equilibrium conditions oxygen vacancies formation are governed by the defect equation: $ZnO = Zn_{Zn}^{x} + V_{O}^{\cdot\cdot} + 2e^{-} + \frac{1}{2}O_2$.

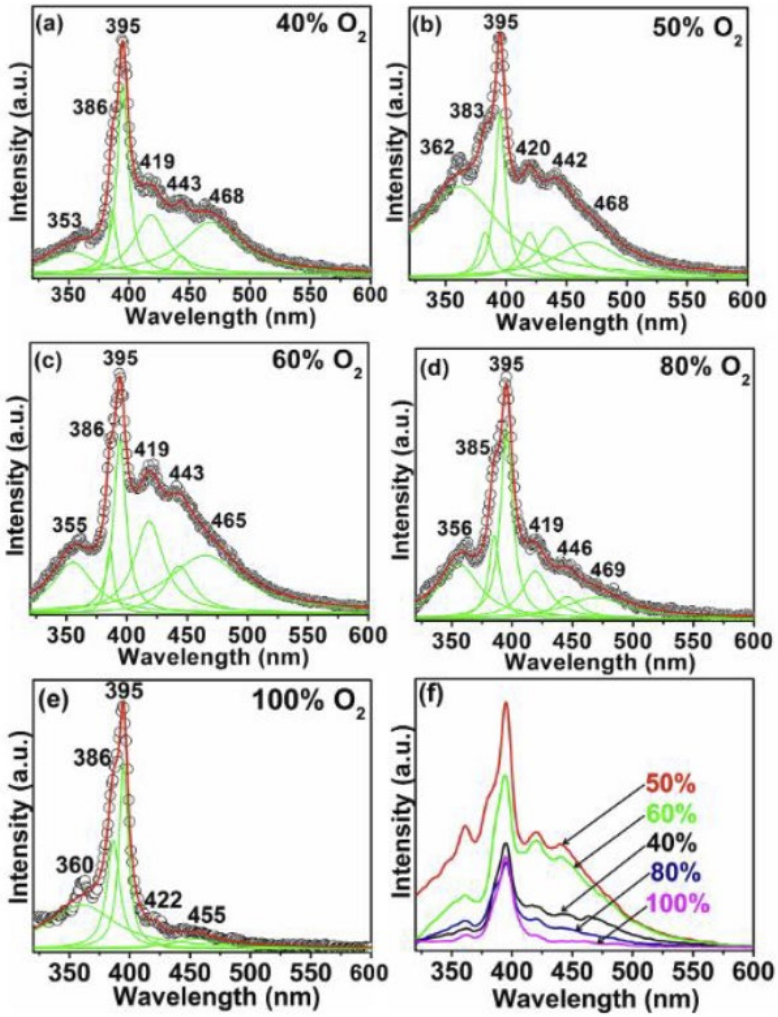

Figure 2.8: PL spectra of ZnO films with different oxygen content [35].

Kunj and Sreenivas have varied oxygen content in ZnO films grown on glass [35]. They have used PL to characterize grown ZnO samples and deconvoluted PL spectrum identified various emissions as depicted in Figure 2.8. PL emissions in ZnO are near bandgap emission (NBE) and Deep level emission (DLE). It is reported that NBE emission is a single excitonic

emission [36] but Kunj and Sreenivas observe splitting in NBE located in the UV range, and Xiao reported that increased broadening(resulting in splitting) in the NBE as a result of the reduction in grain sizes [37]. In the DLE, the peak located at 468 nm is not observed in the ZnO sample grown in 100% oxygen and has been associated with an oxygen vacancy. The peak at ~419 has been reported to be contributed from Zn interstitials in the literature [38,39].

2.5 Boron Nitride Based Dielectric

A variety of dielectrics, both high and low *k*, are being considered for use as gate insulators in transparent electronics [40,41]. Here, boron nitride (BN) has emerged as an attractive candidate because of its good surface topography, and a surface that is relatively free of dangling bonds and electronic traps [42]. Structurally, BN occurs as cubic *c*-BN, wurtzite *w*-BN, hexagonal *h*-BN, rhombohedral *r*-BN, turbostratic *t*-BN, and an amorphous form *a*-BN. *c*-BN and *h*-BN are the two most equilibrium stable structures of BN with sp^3 and sp^2 bonding respectively [43]. Atomic and lattice positions of the various phase of BN is summarized in Table 2.1.

Table 2.2: Structural data of various BN phases [44].

Phase	*a* (Å) [18]	*c* (Å) [18]	Space group	Atom positions
hBN [19]	2.5043	6.6562	$P6_3/mmc$ (194)	B: (0,0,0), (2/3,1/3,1/2) N: (2/3,1/3,0),(0,0,1/2)
rBN [20]	2.5042	9.99	R3m (160)	B: (0,0,0),(2/3,1/3,1/3), (1/2,2/3,2/3) N: (2/3,1/3,0),(1/3,2/3,1/3), (0,0,2/3)
cBN [1,21]	3.6153		$F\bar{4}3m$ (216)	B: (0,0,0), (1/2,1/2,0), (0,1/2,1/2), (1/2,0,1/2) N: (1/4,1/4,1/4), (3/4,3/4,1/4),(1/4,3/4,3/4), (3/4,1/4,3/4)
wBN [21,22]	2.5505	4.210	$P6_3mc$ (186)	B: (0,0,0), (1/3,2/3,1/2) N: (0,0,3/8), (1/3,2/3,7/8)

Its hexagonal polytype is of interest for use in 2D semiconductor systems because of its layered structure, and aforementioned excellent surface properties. Chemical analysis using XPS

suggests B 1s peak appears at 190.38 eV and N 1s appears at 397.88 eV [45] shown in Figure 2.9. Because *a*-BN is predominantly sp^2 bonded, XPS data is identical to *h*-BN [46].

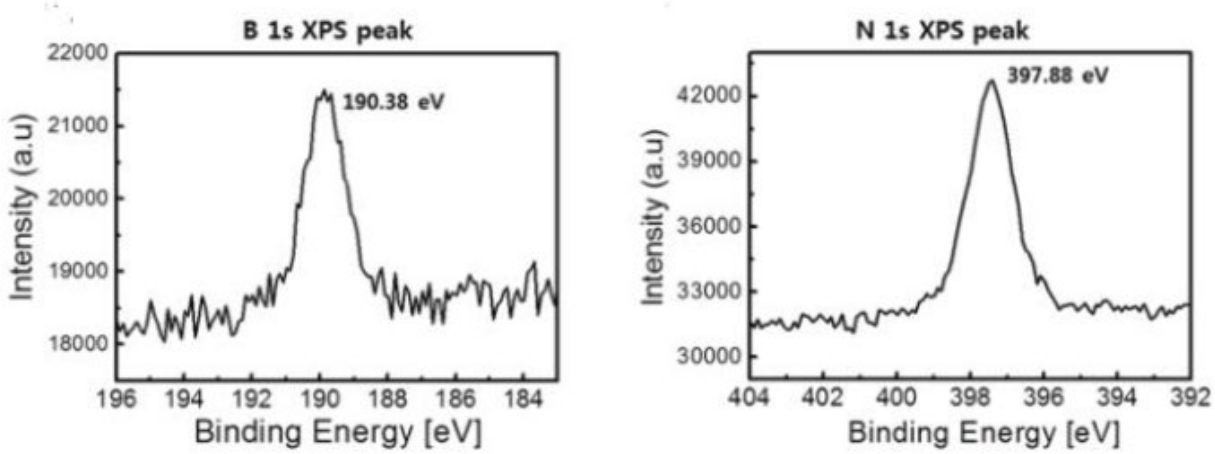

Figure 2.9: XPS of core elements in h-BN [45].

Dean et al have reported almost an order of magnitude higher mobility for exfoliated graphene on *h*-BN substrates compared to SiO_2 substrates [42], and Lee et al have shown that *h*-BN is a superior encapsulant to HfO_2 for MoS_2 based transistors [47]. It should be noted that the synthesis of *h*-BN typically involves high temperatures and that the aforementioned demonstrations involved exfoliated *h*-BN films. Experiments have shown that intentional incorporation of carbon during BN synthesis results in hybrid BNC structures which are a promising area for bandgap engineering of BN compounds [48], and it has been suggested that oxygen narrows the bandgap of BN nanotubes [49]. While crystalline BN films generally exhibit excellent chemical and thermal stability, and good atomic smoothness, their specific structural, electrical, and optical properties vary significantly [44,50,51] depending on polymorph, bonding state (sp^2 or sp^3), and incorporated chemical impurities [52,53]. Efforts to target specific phases and properties of hexagonal and cubic BN by tuning growth conditions are ongoing [54–56].

Amorphous boron nitride (*a*-BN_x) can be grown at significantly lower temperatures than

h-BN, which makes its synthesis compatible with a variety of other materials and substrates [57]. Thus, a-BN_x has gained attention for use as substrates for graphene transistors [58], as a protective layer [59,60], and a gate dielectric [61,62]. *a*-BN_x and *h*-BN are predominantly sp^2 bonded [63,64], and with bandgap values, in the 3.2 -5.9 eV [65–68] range, the material is transparent over the complete visible spectrum. Bulk *h*-BN is characterized by an indirect bandgap [69–71], although recent work has shown a transition to direct bandgap when in monolayer form [72,73]. A variety of conduction mechanisms have been reported for films grown by different methods. Table 2.3 summarizes various insulator conduction mechanisms.

Table 2.3: Conduction mechanisms in insulators [74].

Conduction Mechanism	Current Density Expression	Electric Field and Temperature Dependency [b]
Schottky Emission	$J_{SE} = \frac{4\pi q m^*(kT)^2}{h^3}\exp\left[\frac{-q(\phi_B - \sqrt{qE/4\pi\varepsilon})}{kT}\right]$	$J_{SE} \propto T^2\exp\left(A\frac{\sqrt{E}}{T} - B\right)$
Fowler-Nordheim (F-N) Tunneling	$J_{FN} = \frac{q^2}{8\pi h\phi_B}E^2\exp\left(\frac{-8\pi\sqrt{2qm^*}}{3hE}\phi_B^{3/2}\right)$	$J_{FN} \propto E^2\exp\left(\frac{-A}{E}\right)$
Direct Tunneling	$J_{DT} \approx \exp\left\{\frac{-8\pi\sqrt{2q}}{3h}(m^*\phi_B)^{1/2}\kappa \cdot t_{ox,eq}\right\}$	$J_{DT} \propto \exp(-A \cdot \kappa t_{ox,eq})$
Poole-Frenkel (P-F) Emission	$J_{PF} = q\mu N_C E\exp\left[\frac{-q(\phi_T - \sqrt{qE/\pi\varepsilon})}{kT}\right]$	$J_{PF} \propto E \cdot \exp\left(A\frac{\sqrt{E}}{T} - B\right)$
Space-charge-limited Conduction (SCLC) [a]	$J_{SCLC} = \frac{9}{8}\varepsilon_i\mu\theta\frac{V^2}{d^3}$	$J_{SCLC} \propto E^2$
Ionic Conduction	$J_{ionic} \propto \frac{E}{T}\exp\left\{\frac{-\Delta G^*}{kT}\right\}$	$J_{ionic} \propto \frac{E}{T}\exp\left(\frac{-A}{T}\right)$
Ohmic Conduction	$J_{ohmic} = \sigma E = q\mu N_C E\exp\left[\frac{-(E_C - E_F)}{kT}\right]$	$J_{ohmic} \propto E \cdot \exp\left(\frac{-A}{T}\right)$
Nearest Neighbor Hopping (NNH)	$J_{NNH} = \sigma_0\exp\left(\frac{-T_0}{T}\right) \cdot E$	$J_{VRH} \propto E \cdot \exp\left(\frac{-A}{T}\right)$
Variable-range Hopping (VRH)	$J_{VRH} = \sigma_0\exp\left(\frac{-T_0}{T}\right)^{\frac{1}{4}} \cdot E$	$J_{VRH} \propto E \cdot \exp\left(\frac{-A}{T}\right)^{\frac{1}{4}}$
Trap-assisted Tunneling (TAT)	$J_{TAT} = A\exp\left(\frac{-8\pi\sqrt{2qm^*}}{3hE}\phi_T^{3/2}\right)$	$J_{TAT} \propto \exp\left(\frac{-A}{E}\right)$

[a] High field only, low field follows Ohm's Law; [b] A & B are constants.

Novikov and Gritsenko reported on the conduction mechanism in 100 nm *a*-BN_x films grown on Si substrates by pyrolysis between 400-600^o C [75]. They studied Al/BN/Si MIS structures where the Al metal was thermally evaporated and showed that multiphonon trap ionization adequately described the measured behavior over a wide range of temperatures [28]. In contrast, Voskoboynikov et al proposed that Frenkel-type mechanisms in the bulk were responsible for the transport in low-temperature pyrolytic BN [76]. In other reports, Schmolla and Hartnagel proposed space charge limited conduction was the dominant mechanism in *a*-BNx thin films grown by organic plasma-enhanced chemical vapor deposition [77], while Ong et al proposed that phonon-assisted charge hopping between states near the Fermi energy was the dominant transport mechanism in *a*-BN_x samples grown by ion beam assisted sputtering [78]. The charge transport mechanism in *a*-BN_x remains unsettled. Amorphous *a*-$BOxN_y$ films of variable compositions were recently reported to possess comparable breakdown strength and bandgap to *a*-BN_x [79].

2.6 2-H WS_2 Semiconductors

WS_2 exhibits three different phases shown in Figure 2.10: octaheral (1T) phase, trigonal prismatic (2H) phase, and the rhombohedral (3R) phases. In bulk form, the 1T and 2H phases exist as strongly bonded monolayers that a held by weak Van der Waal forces [80]. The 1T phase has a distorted structure and is metallic which the 2H is semiconducting. 2H-WS_2 has been reported to have an indirect bandgap of ~1.2 eV in the bulk form [81], but a transition to a direct bandgap of 1.9 eV in the monolayer [80]. A single crystal of 2H-WS_2 belong to the $P6_3/mmc$ space group while a single layer of 2H-WS_2 has a $P\bar{6}m2$. It is reported that the lattice constant for a single crystal 2H-WS_2 is a = 3.153 Å and c = 12.323 Å [82]. The growth process of WS_2 films includes CVD, ALD, sputtering, PLD. Because WS_2 has a small effective electronic mass

as compared to other transition metal dichalcogenides, it is theoretically projected to exhibit higher mobility [83,84].

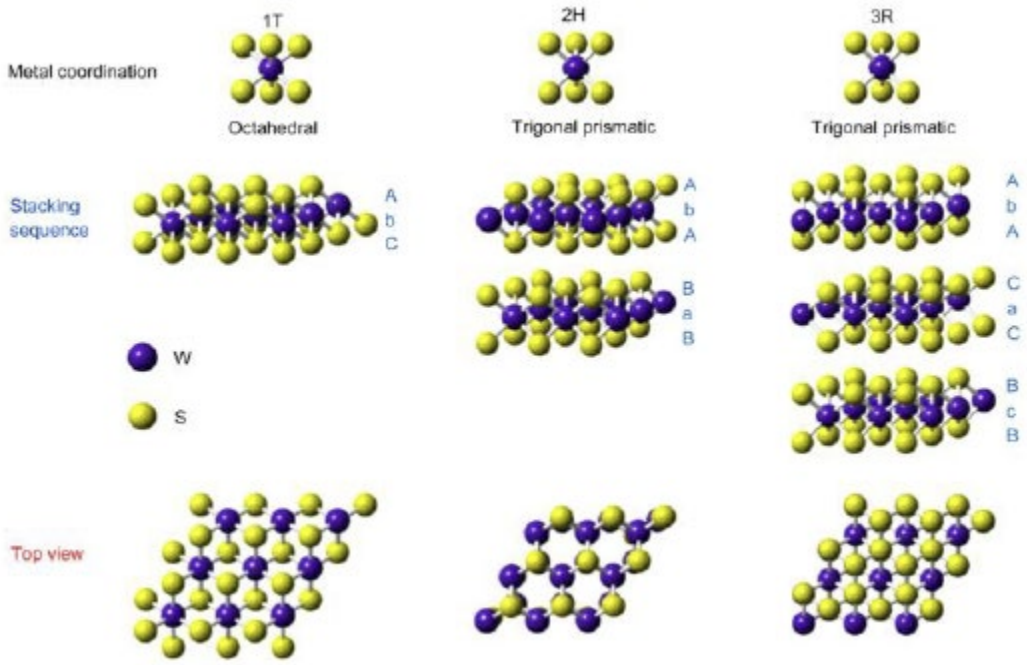

Figure 2.10: Phases of WS_2 [85].

CVD growth of WS_2 includes direct sulfurization of tungsten oxides or W metal [86,87]. In direct sulfurization, the sulfur vapor is transported by an inert gas to the already deposited oxide or metal where the chemical reaction occurs. Other CVD techniques involve the reaction of tungsten base compounds like $W(CO)_6$, WCl_6, or $WOCl_4$ with sulfur supplies from H_2S, $HS(CH_2)_2SH$, or $HSC(CH_3)_3$ [88,89]. In ALD growth of WS_2, $W(CO)_6$ has been reported as the precursor and H_2S the reactant [90]. Other works have synthesis ALD grown WS_2 with WF_6 and H_2S in H_2 plasma [91]. Sputtering of WS_2 has not been effective in synthesizing stoichiometric WS_2 films, results show that the best S/W ratio of 1.5 was achieved at higher sputter pressure [92]. This could be associated with the higher vapor pressure of S atoms. The incorporation of H_2S in plasma has been reported to increase the S/W ratio to ~1.8 [93]. Because of the advantage of almost congruent ablation of target material in PLD growth resulting in equaling chemical

composition of target and film growth on the substrate; PLD grown WS_2 is an emerging area of interest [94–96]. In PLD processing of WS_2, it has been observed that low power density results in improved sulfur concentration and but also diminishing crystallinity [97]. There have been reported success in doping of PLD films by incorporation of dopant during target fabrication [98]. Also, PLD-grown WS_2 films have been shown to have carrier mobility significantly higher than CVD grown making PLD processed WS_2 a better choice of process for high response electronic devices [84]. Chemical analysis of WS_2 thin films using x-ray photoelectron spectroscopy XPS as shown in Figure 2.11 reports a split in both W4f and S2p spectra. $W4f_{7/2}$ located at binding energy 32.9 eV while $W4f_{5/2}$ located 35.1 eV; S $2p_{3/2}$ 161.7 eV is located at a binding energy of [94,97,99,100].

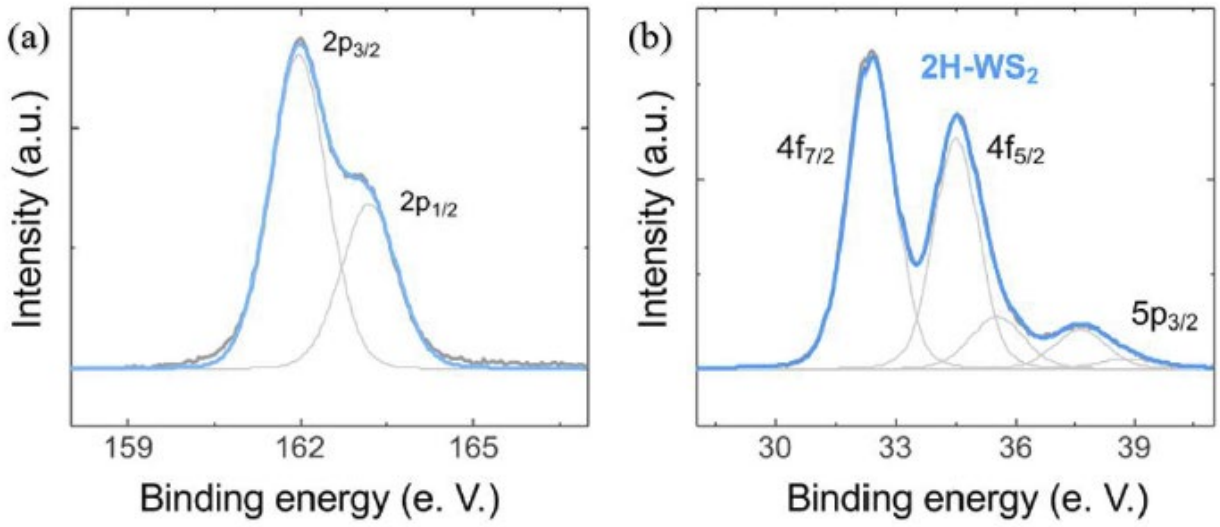

Figure 2.11: XPS Spectra of WS2: (a) S2p, (b) W4f [94].

With the application of density function theory (DFT) and local density approximate (LDA); the band-structure is estimated for both single crystal and single layer 2H-WS_2 shown in fig. 2.12 (a) and (b). As shown in Figure 2.12(a), the conduction band minimum lies between K and Γ point of the Brillouin zone and a corresponding bandgap ~1.2 eV suggesting indirect transition in bulk. On the other hand, Figure 2.12(b) shows that for a monolayer 2H-WS_2, the

conduction band minimum is at the K point with energy 1.6 eV corresponding to the bandgap of a monolayer WS_2.

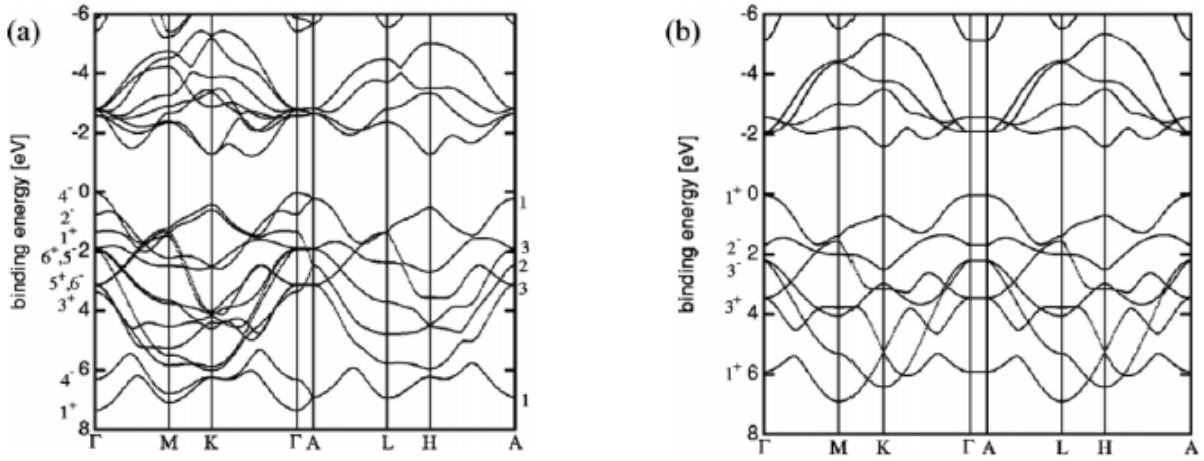

Figure 2.12: Band structure of 2H-WS_2 (a) Single-crystal, (b) Single layer [81].

In electronic devices, WS_2 has been successfully shown to serve as a channel material in light-emitting transistors; in one of the instances, WS_2 was stacked in with an ionic liquid gated material [101]. High room temperature mobility (83 $cm^2 V^{-1} s^{-1}$) transistors comprising of a stack of WS_2 and high k Al_2O_3 have been reported with mechanically exfoliated single-layer WS_2 and ALD grown Al_2O_3 [102]. Other groups have also reported high photocurrent generations from WS_2 base transistors with photoresponse exceeding that of MoS_2 base phototransistors [103], and high responsive WS_2 base flexible photodetectors with WS_2 room temperature carrier mobility of 50 $cm^2 V^{-1} s^{-1}$ [104].

2.7 References

[1] W. Paul K., The TFT a new thin-film transistor, Proc. IRE. 50 (n.d.) 1462–1469.

[2] B. T. P., A. Juris A., D. G. Douglas, A 6 x 6 inch 20 lines-per-inch liquid-crystal display panel, IEEE Trans. Electron Devices. 20 (n.d.) 995–1001. https://doi.org/https://doi.org/10.1109/T-ED.1973.17780.

[3] B. William F., H. Douglas E., T. William W., A history of the invention of the transistor and where it will lead us, IEEE J. Solid-State Circuits. 32 (n.d.) 1858–1865.

[4] H. Lars, Electrolyte-gated organic thin-film transistors, n.d.

[5] S. Anchal, M. Charu, S. Jatinder, Performance Evaluation of Thin Film Transistors: History, Technology Development and Comparison: A Review, Int. J. Comput. Appl. 89 (n.d.) 36–40.

[6] T.-M. Agnès, I. Satoshi, S. Bertrand-David, C. Grant A., T. Takuya, F. Hiroyuki, T. Hiroshi, Review on thin-film transistor technology, its applications, and possible new applications to biological cells, Jpn. J. Appl. Phys. 55 (n.d.) 04EA08.

[7] E. Daniel, C. Nathan, B. Warwick, D. Paul C., Z. Xiaojing, Organic thin-film transistor (OTFT)-based sensors, Electronics. 3 (n.d.) 234–254.

[8] X. Chen, C. Longlong, L. Tongkuai, Z. Zhihan, Z. Tingting, L. Xifeng, Z. Jianhua, Highly sensitive flexible pressure sensor by the integration of microstructured PDMS film with a-IGZO TFTs, IEEE Electron Device Lett. 39 (n.d.) 1073–1076.

[9] A. S. C., B. J. L., Remeasurement of the structure of hexagonal ZnO, Acta Crystallogr. Sect. B Struct. Crystallogr. Cryst. Chem. 25 (n.d.) 1233–1236.

[10] A. ABMA, J. C., Review of zincblende ZnO: Stability of metastable ZnO phases, J. Appl. Phys. 102 (n.d.) 4.

[11] J. J. E., H. A. C., Hartree-Fock study of phase changes in ZnO at high pressure, Phys. Rev. B. 48 (n.d.) 7903.

[12] B. Carl H., W. William B., R. Rustum, New high-pressure polymorph of zinc oxide, Science (80-.). 137 (n.d.) 993–993.

[13] D. Serge, High-density phases of ZnO: Structural and compressive parameters, Phys. Rev. B. 58 (n.d.) 14102.

[14] K. H., P. W., K. M., S. W., S. M., H. U., K. G. M., M. D. W., D. T. P., B. P., S. K., P. M. P., Lattice dynamics and hyperfine interactions in ZnO and ZnSe at high external pressures, Phys. Rev. B. 53 (n.d.) 11425–11438. https://doi.org/10.1103/PhysRevB.53.11425.

[15] W. Y., Z. Y., C. W. J., L. G. L., J. J. Z., L. Y. C., L. J., H. T. D., Mn effect on wurtzite-to-cubic phase transformation in ZnO, J. Phys. Chem. Solids. 66 (n.d.) 1775–1778.

[16] D. Aleksandra B., L. Yu Hang, Optical properties of ZnO nanostructures, Small. 2 (n.d.) 944–961.

[17] Z. G., J. K., Experimental band structure of ZnO, Solid State Commun. 54 (n.d.) 701–704.

[18] K. P. D. C., V. Tim D., S. A., Z.-P. J., M. B., J. P. H., F. F., M.-S. V., B. F., M. Chris F., Valence-band electronic structure of CdO, ZnO, and MgO from x-ray photoemission spectroscopy and quasi-particle-corrected density-functional theory calculations, Phys. Rev. B. 79 (n.d.) 205205.

[19] P. A. R. H., R. B. J., P. L. F. J., D. A., S. K. E., S. A., F. F., B. F., C. J., D. S. M., Band structure of ZnO from resonant x-ray emission spectroscopy, Phys. Rev. B. 78 (n.d.) 155114.

[20] Ö. Ü., A. Ya. I., L. C., T. A., R. M. A., D. S., A. V., C. S.-J., M. H., A comprehensive review of ZnO materials and devices, J. Appl. Phys. 98 (2005) 041301. https://doi.org/10.1063/1.1992666.

[21] J. M. A. L., F. Shizuo, R. W. H., H. W. C., C. J. W., S. J. F., MBE growth and properties of ZnO on sapphire and SiC substrates, J. Electron. Mater. 25 (n.d.) 855–862.

[22] P. M., B. E., R. E., D. M., and G. R., Optical and structural investigation of ZnO thin films prepared by chemical vapor deposition (CVD), Thin Solid Films. 403 (n.d.) 485–488.

[23] Z. Jun-Liang, L. Xiao-Min, B. Ji-Ming, Y. Wei-Dong, G. Xiang-Dong, Structural, optical and electrical properties of ZnO films grown by pulsed laser deposition (PLD), J. Cryst. Growth. 276 (n.d.) 507–512.

[24] A. George, B. Aneeqa, W. Paul H., B. Donal DC, A. Thomas D., Electronic properties of ZnO field-effect transistors fabricated by spray pyrolysis in ambient air, Appl. Phys. Lett. 95 (n.d.) 133507.

[25] C. P. F., M. R. S., R. M. H., N. G., Transparent ZnO thin-film transistor fabricated by rf magnetron sputtering, Appl. Phys. Lett. 82 (2003) 1117–1119. https://doi.org/10.1063/1.1553997.

[26] W. Walter, C. Sheng-Yuan, Physical and structural properties of ZnO sputtered films, Mater. Lett. (n.d.) 6.

[27] G. R., B. D., F. Shinobu, Effect of substrate-induced strain on the structural, electrical, and optical properties of polycrystalline ZnO thin films, J. Appl. Phys. 96 (n.d.) 2689–2692.

[28] T. A., O. A., K. M., High-mobility electronic transport in ZnO thin films, Appl. Phys. Lett. 88 (n.d.) 152106.

[29] L. David C., R. Donald C., S. J. R., J. R. L., L. Cole W., C. G., H. W. C., Electrical properties of bulk ZnO, Solid State Commun. 105 (n.d.) 399–401.

[30] C. Jill, K.J. Roger C., Handbook of X-ray photoelectron spectroscopy, Perkin-Elmer Corp. 40 (n.d.) 221.

[31] H. P.-T., C. Y.-C., K. K.-S., W. C.-M., Luminescence mechanism of ZnO thin film investigated by XPS measurement, Appl. Phys. A. 90 (n.d.) 317–321.

[32] P. Natalie O. V., H. Ian, R. Akshay, W. Mark W. B., D. Caterina, M. Rajaram Sakharam, B. James S., L. Rami R. M., G. Neil C., M. Hidetoshi, F. Richard H., S. Henry J., W. Mark E., Efficient ZnO Nanowire Solid-State Dye-Sensitized Solar Cells Using Organic Dyes and Core−shell Nanostructures, J. Phys. Chem. C. 113 (2009) 18515–18522. https://doi.org/10.1021/jp904919r.

[33] Z. Ali Khorsand, A.A. Nur Suhaili, H. Abdul Manaf, K. Frouzan, XPS and UV–vis studies of Ga-doped zinc oxide nanoparticles synthesized by gelatin based sol-gel approach, Ceram. Int. 42 (n.d.) 13605–13611.

[34] I. Chukwudi E., A. Corey L., R. Urmilaben P., O. Khalil D., V. Andrey A., S. Nigel D., Bonding and stoichiometry in low-energy radio frequency magnetron sputtered ZnO thin films on flexible substrate, Vacuum. 183 (n.d.) 109869. https://doi.org/10.1016/j.vacuum.2020.109869.

[35] K. Saurabh, S. K., Residual stress and defect content in magnetron sputtered ZnO films grown on unheated glass substrates, Curr. Appl. Phys. 16 (n.d.) 748–756.

[36] W. L. W., W. F., T. D. X., L. W. J., F. L., K. C. Y., Z. M., Effects of Na content on structural and optical properties of Na-doped ZnO thin films prepared by sol–gel method, J. Alloys Compd. 623 (n.d.) 367–373.

[37] X. S. S., Z. L., L. Y. H., L. J. S., Nanocrystalline ZnO films prepared by pulsed laser deposition and their abnormal optical properties, Appl. Surf. Sci. 283 (n.d.) 781–787.

[38] J. B. J., I. S., L. S. Yl, Violet and UV luminescence emitted from ZnO thin films grown on sapphire by pulsed laser deposition, Thin Solid Films. 366 (n.d.) 107–110.

[39] H. Deng-Lu, Z. Rui-Bin, W. Yan-Yan, Z. Cong-Mian, P. Cheng-Fu, T. Gui-De, Room temperature ferromagnetism in Ni-doped ZnO films, Curr. Appl. Phys. 10 (n.d.) 124–128.

[40] Z. Yong-Hui, M. Zeng-Xia, L. Hui-Li, D. Xiao-Long, Review of flexible and transparent thin-film transistors based on zinc oxide and related materials, Chinese Phys. B. 26 (n.d.) 047307. https://doi.org/10.1088/1674-1056/26/4/047307.

[41] F. Elvira, B. Pedro, M. Rodrigo, Oxide semiconductor thin-film transistors: a review of recent advances, Adv. Mater. 24 (n.d.) 2945–2986.

[42] D. Cory R., Y. Andrea F., M. Inanc, L. Chris, W. Lei, S. Sebastian, W. Kenji, T. Takashi, K. Phillip, S. Kenneth L., Boron nitride substrates for high-quality graphene electronics, Nat. Nanotechnol. 5 (n.d.) 722–726.

[43] B. F. P., W. R. H., Direct Transformation of Hexagonal Boron Nitride to Denser Forms, J. Chem. Phys. 38 (n.d.) 1144–1149. https://doi.org/10.1063/1.1733815.

[44] M. P. B., M. K. F., M. D. L., Review of advances in cubic boron nitride film synthesis, Mater. Sci. Eng. R Reports. 21 (n.d.) 47–100.

[45] K. Gwangwoo, J. A-Rang, J. Hu Young, L. Zonghoon, K. Dae Joon, S. Hyeon Suk, Growth of High-Crystalline, Single-Layer Hexagonal Boron Nitride on Recyclable Platinum Foil, Nano Lett. 13 (2013) 1834–1839. https://doi.org/10.1021/nl400559s.

[46] H. Seokmo, L. Chang-Seok, L. Min-Hyun, L. Yeongdong, M. Kyung Yeol, K. Gwangwoo, Y. Seong In, I. Kyuwook, K. Ki-Jeong, S. Tae Joo, Ultralow-dielectric-constant amorphous boron nitride, Nature. 582 (n.d.) 511–514.

[47] L. Gwan-Hyoung, C. Xu, K. Young Duck, A. Ghidewon, Z. Xian, L. Chul-Ho, Y. Fan, W. Kenji, T. Takashi, K. Philip, Highly stable, dual-gated MoS2 transistors encapsulated by hexagonal boron nitride with gate-controllable contact, resistance, and threshold voltage, ACS Nano. 9 (n.d.) 7019–7026.

[48] C. Lijie, S. Li, J. Chuanhong, J. Deep, W. Dangxin, L. Yongjie, S. Anchal, W. Z. F., S. Kevin, B. Luis, Atomic layers of hybridized boron nitride and graphene domains, Nat. Mater. 9 (n.d.) 430–435.

[49] S. Ram Sevak, Influence of oxygen impurity on electronic properties of carbon and boron nitride nanotubes: A comparative study, AIP Adv. 5 (n.d.) 117150.

[50] S. Li, C. Lijie, L. Hao, S. Pavel B., J. Chuanhong, N. Jie, K. Alexander G., K. Dmitry G., L. Jun, Y. Boris I., A. Pulickel M., Large Scale Growth and Characterization of Atomic Hexagonal Boron Nitride Layers, Nano Lett. 10 (2010) 3209–3215. https://doi.org/10.1021/nl1022139.

[51] T. J., W. N. E., O. T. E., Turbostratic Boron Nitride, Thermal Transformation to Ordered-layer-lattice Boron Nitride, J. Am. Chem. Soc. 84 (n.d.) 4619–4622. https://doi.org/10.1021/ja00883a001.

[52] P. M. I., B. Mădălina-Gabriela, Structure and properties modifications in boron nitride. Part I: Direct polymorphic transformations mechanisms, UPB Sci. Bull., Ser. B. 69 (n.d.) 35–42.

[53] Z. J., C. Q., L. X., H. Z., L. W., M. Y., G. Q., G. W., Z. G., Plasma induced sp2 to sp3 transition in boron nitride, Chem. Phys. Lett. 399 (n.d.) 451–455. https://doi.org/10.1016/j.cplett.2004.10.050.

[54] K. Daniel J., M. Russell, Phase control of cubic boron nitride thin films, J. Appl. Phys. 72 (1992) 504–513. https://doi.org/10.1063/1.351881.

[55] J. Chuanhong, L. Fang, S. Kazu, I. Sumio, Fabrication of a Freestanding Boron Nitride Single Layer and Its Defect Assignments, Phys. Rev. Lett. 102 (n.d.) 195505. https://doi.org/10.1103/PhysRevLett.102.195505.

[56] H. Jianyu Y., Y. Hidehiro, M. Hirotaro, HRTEM and EELS studies on the amorphization of hexagonal boron nitride induced by ball milling, J. Am. Ceram. Soc. 83 (n.d.) 403–409.

[57] G. Nicholas R., M. Christopher, J. Michael L., H. Jianjun, F. Timothy S., V. Andrey A., Temporally and spatially resolved plasma spectroscopy in pulsed laser deposition of ultra-thin boron nitride films, J. Appl. Phys. 117 (n.d.) 165305.

[58] U. Md Ahsan, G. Nicholas, S. Amol, N. Rachel, J. Michael, V. Andrey, K. Goutam, Mobility enhancement in graphene transistors on low temperature pulsed laser deposited boron nitride, Appl. Phys. Lett. 107 (n.d.) 203110.

[59] S. Benjamin, G. Nicholas, K. Sergiy, D. Albert V., V. Andrey A., Hexagonal MoTe 2 with Amorphous BN Passivation Layer for Improved Oxidation Resistance and Endurance of 2D Field Effect Transistors, Sci. Rep. 8 (2018) 8668. https://doi.org/10.1038/s41598-018-26751-4.

[60] A.F. Rigosi, C.I. Liu, N.R. Glavin, Y. Yang, H.M. Hill, J. Hu, A.R. Hight Walker, C.A. Richter, R.E. Elmquist, D.B. Newell, Electrical Stabilization of Surface Resistivity in Epitaxial Graphene Systems by Amorphous Boron Nitride Encapsulation, ACS Omega. 2 (2017) 2326–2332. https://doi.org/10.1021/acsomega.7b00341.

[61] A. Qasim, L. Hongwei, S. Jianjun, C. Yuanpeng, X. Xiaochuan, A. Aqrab ul, L. Jianxun, D. Guotong, Growth and characterization of amorphous boron nitride dielectric films on Si via RF sputtering at room temperature, Mater. Lett. 227 (n.d.) 284–288. https://doi.org/10.1016/j.matlet.2018.05.099.

[62] J. Lee, J.-H. Ryu, B. Kim, F. Hussain, C. Mahata, E. Sim, M. Ismail, Y. Abbas, H. Abbas, D.K. Lee, M.-H. Kim, Y. Kim, C. Choi, B.-G. Park, S. Kim, Synaptic Characteristics of Amorphous Boron Nitride-Based Memristors on a Highly Doped Silicon Substrate for Neuromorphic Engineering, Cite This ACS Appl. Mater. Interfaces. 12 (2020) 33916. https://doi.org/10.1021/acsami.0c07867.

[63] Z. R., H. M., S. M.B., Properties of amorphous boron nitride thin films, J. Non. Cryst. Solids. 198–200 (n.d.) 403–406. https://doi.org/10.1016/0022-3093(95)00748-2.

[64] K. Sean W., P. Michelle M., O. Joseph W., C. A. N., B. Justin, B. Jeff, F. Marc, K. Markus, F. Benjamin, Valence and conduction band offsets at amorphous hexagonal boron nitride interfaces with silicon network dielectrics, Appl. Phys. Lett. 104 (2014) 102901. https://doi.org/10.1063/1.4867890.

[65] N. Katsumitsu, Preparation and Properties of Amorphous Boron Nitride Films by Molecular Flow Chemical Vapor Deposition, J. Electrochem. Soc. 132 (1985) 1757–1762. https://doi.org/10.1149/1.2114206.

[66] S. Michael, P. Qing, H. Merle, S. Jodie, M. J. Matthew, Optical characterization of nanocrystalline boron nitride thin films grown by atomic layer deposition, Thin Solid Films. 571 (n.d.) 51–55.

[67] G. Nicholas R., M. Christopher, J. Michael L., H. Jianjun, H. Phillip T., H. Al M., B. Austin T., G. Christopher A., D. Michael F., M. Michael E., H. Drew M., F. Timothy S., V. Andrey A., Amorphous Boron Nitride: A Universal, Ultrathin Dielectric For 2D

Nanoelectronics, Adv. Funct. Mater. 26 (n.d.) 2640–2647. https://doi.org/https://doi.org/10.1002/adfm.201505455.

[68] H. D. M., D. G. L., E. P. C., Optical properties of pyrolytic boron nitride in the energy range 0.05—10 eV, Phys. Rev. B. 30 (n.d.) 6051.

[69] C. Guillaume, V. Pierre, G. Bernard, Hexagonal boron nitride is an indirect bandgap semiconductor, Nat. Photonics. 10 (n.d.) 262–266.

[70] C. A., P. M., B. A., J. H. J. F., F. Arthur J., Electronic interlayer states in hexagonal boron nitride, Phys. Rev. B. 32 (n.d.) 6997.

[71] A. B., L. S., R. P., A. M., Huge excitonic effects in layered hexagonal boron nitride, Phys. Rev. Lett. 96 (n.d.) 026402.

[72] W. Darshana, W. Leigh, V. de W. Chris G., Monolayer to bulk properties of hexagonal boron nitride, J. Phys. Chem. C. 122 (n.d.) 25524–25529.

[73] E. Christine, V. Pierre, P. Thomas, S. A., M. C. J., C. T. S., E. L., F. C. T., B. P. H., N. S. V., Direct band-gap crossover in epitaxial monolayer boron nitride, Nat. Commun. 10 (n.d.) 1–7.

[74] L. Ee Wah, I. Razali, Conduction mechanism of valence change resistive switching memory: a survey, Electronics. 4 (n.d.) 586–613.

[75] N. Yu N., G. V. A., The charge transport mechanism in amorphous boron nitride, J. Non. Cryst. Solids. 544 (n.d.) 120213.

[76] V. V. V., G. V. A., E. V. M., L. V. E., E. F. L., Structure and electrophysical properties of boron nitride thin films, Phys. Status Solidi. 34 (1976) 85–94. https://doi.org/10.1002/pssa.2210340106.

[77] S. W., H. H.L., Amorphous BN films produced in a double-plasma reactor for semiconductor applications, Solid. State. Electron. 26 (n.d.) 931–939. https://doi.org/10.1016/0038-1101(83)90069-2.

[78] O. C.W, C. K.F, C. C.L, Optical absorption and transport mechanisms of dual ion-beam-deposited boron-rich boron nitride films, Thin Solid Films. 388 (n.d.) 217–225. https://doi.org/10.1016/S0040-6090(01)00763-5.

[79] A. Corey L., I. Chukwudi E., D. Maddox, G. Spencer, G. Nicholas R., M. Christopher, S. Nigel D., V. Andrey A., Composition, dielectric breakdown, and bandgap of ultra-thin amorphous boron oxynitride produced by magnetron sputtering, Vacuum. 188 (n.d.) 110211.

[80] W. Qing Hua, K.-Z. Kourosh, K. Andras, C. Jonathan N., S. Michael S., Electronics and optoelectronics of two-dimensional transition metal dichalcogenides, Nat. Nanotechnol. 7 (n.d.) 699–712. https://doi.org/10.1038/nnano.2012.193.

[81] K. A., T. S., E. V., P. C., J. W., Electronic band structure of single-crystal and single-layer WS 2 : Influence of interlayer van der Waals interactions, Phys. Rev. B. 64 (n.d.) 205416. https://doi.org/10.1103/PhysRevB.64.205416.

[82] S. W. J., D.B. J. L., J. F., Crystal structures of tungsten disulfide and diselenide, J. Solid State Chem. 70 (n.d.) 207–209.

[83] L. Leitao, K. S. Bala, O. Yijian, G. Jing, Performance limits of monolayer transition metal dichalcogenide transistors, IEEE Trans. Electron Devices. 58 (n.d.) 3042–3047.

[84] Y. J D, Z. Z Q, S. J M, Y. G W, Stable, high-responsive and broadband photodetection based on large-area, (n.d.) 25.

[85] L. Wen, X. Jun-Lei, L. Hai-Peng, J. Quan-Li, Z. Hai-Jun, Tungsten disulfide: synthesis and applications in electrochemical energy storage and conversion, Tungsten. (n.d.) 1–23.

[86] Y. Weihuang, S. Jingzhi, W. Jianpu, S. Xiaonan, C. Bingchen, P. Namphung, Z. Chenji, C. Yu, W. Yanlong, C. Chunxiao, Electrically tunable valley-light emitting diode (vLED) based on CVD-grown monolayer WS2, Nano Lett. 16 (n.d.) 1560–1567.

[87] N. Sheung Mei, W. Hon Fai, W. Wang Cheung, T. Choon Kiat, C. Sin Yuk, M. Chee Leung, L. Gui Jun, D. Qing Chen, L. Chi Wah, WS2 nanotube formation by sulphurization: Effect of precursor tungsten film thickness and stress, Mater. Chem. Phys. 181 (n.d.) 352–358.

[88] C. J.-W., D. Z. R., O. F. S., WS2 thin films by metal organic chemical vapor deposition, J. Cryst. Growth. 186 (n.d.) 137–150.

[89] C. Claire J., P. Ivan P., P. Emily S., Atmospheric pressure chemical vapour deposition of WS2 thin films on glass, Polyhedron. 22 (n.d.) 1499–1505. https://doi.org/10.1016/S0277-5387(03)00194-3.

[90] Y. Seungmin, N. Dip K., R. R., K. Tae Hyun, S. Bonggeun, J. Yujin, B. Jong-Seong, H. Jeong Woo, K. Soo-Hyun, K. Hyungjun, Low-temperature direct synthesis of high quality WS2 thin films by plasma-enhanced atomic layer deposition for energy related applications, Appl. Surf. Sci. 459 (n.d.) 596–605.

[91] G. Benjamin, M. Ankit Nalin, B. Hugo, S. Quentin, M. Johan, F. Alexis, C. Thierry, N. Thomas, V. Patrick, V. Wilfried, H. Marc, R. Iuliana, C. Matty, D. Annelies, Nucleation mechanism during WS_2 plasma enhanced atomic layer deposition on amorphous Al_2O_3 and sapphire substrates, J. Vac. Sci. Technol. A Vacuum, Surfaces, Film. 36 (n.d.) 01A105. https://doi.org/10.1116/1.5003361.

[92] S. Erik, S. Erik, S. Jill, N. Harald, K. Tomas, J. Staffan, J. Ulf, N. Tomas, Mechanisms for compositional variations of coatings sputtered from a WS2 target, Surf. Coatings Technol. 252 (n.d.) 186–190.

[93] E. K., Preparation routes based on magnetron sputtering for tungsten disulfide (WS2) films for thin-film solar cells, Phys. status solidi. 245 (n.d.) 1745–1760. https://doi.org/10.1002/pssb.200879545.

[94] G. Florian, Z. Victor, C. Cécile, S. Anke, G. Marta, V. Aymeric, B. Pierre, B. Odile, S. Bernard, M. Marie-Blandine, WS2 2D Semiconductor Down to Monolayers by Pulsed-Laser Deposition for Large-Scale Integration in Electronics and Spintronics Circuits, ACS Appl. Nano Mater. 3 (n.d.) 7908–7916.

[95] S. Matteo, R. Cristy Leonor Azanza, S. Paolo, E. Raju, M. Antonio, O. Michele, M. Rachel, Effect of annealing and nanostructuring on pulsed laser deposited WS2 for HER catalysis, Appl. Catal. A Gen. 510 (n.d.) 156–160.

[96] A. Salman, H. Mohammad, A. Abdulaziz, A. Ahmed, A. Fahhad H., PLD grown polycrystalline tungsten disulphide (WS 2) films, J. Mater. 2013 (n.d.) 603648.

[97] R. Urmilaben P., C. Bimin, I. Chukwudi, N. Gilbert, V. Andrey A., S. Nigel D., Growth of pulsed laser deposited few-layer WS2 films, J. Vac. Sci. Technol. A Vacuum, Surfaces, Film. 37 (n.d.) 051505.

[98] R. Urmila P., E. Justin, V. Andrey A., S. Nigel D., Extrinsic p-type doping of few layered WS2 films with niobium by pulsed laser deposition, Appl. Phys. Lett. 113 (n.d.) 062106.

[99] F. Huilong, Y. Yang, F. Xiujun, W. Gunuk, R. Gedeng, T. James M., Tungsten-based porous thin-films for electrocatalytic hydrogen generation, J. Mater. Chem. A. 3 (2015) 5798–5804. https://doi.org/10.1039/C4TA06938B.

[100] R. Urmilaben P., J. Jitendra Kumar, V. Andrey A., S. Nigel D., A photoelectron study of annealing induced changes to workfunction and majority carrier type in pulsed laser deposited few layer WS 2 films, J. Mater. Sci. Mater. Electron. 29 (n.d.) 20051–20056.

[101] J. Sanghyun, U. Nicolas, B. Helmuth, K. Alexey B., M. Alberto F., Mono- and Bilayer WS_2 Light-Emitting Transistors, Nano Lett. 14 (2014) 2019–2025. https://doi.org/10.1021/nl500171v.

[102] C. Yang, X. Run, Y. Zhihao, P. Yiming, O. Zhun-Yong, W. Xiaoxu, W. Junzhuan, N. Haiyan, N. Zhenhua, W. Yun, C. Tangsheng, S. Yi, W. Baigeng, Z. Gang, Z. Yong-Wei, W. Xinran, High-Performance Monolayer WS2 Field-Effect Transistors on High-κ Dielectrics, Adv. Mater. 27 (n.d.) 5230–5234. https://doi.org/10.1002/adma.201502222.

[103] H.L. Seung, L. Daeyeong, S.H. Wan, H. Euyheon, J. Debdeep, J.Y. Won, High-performance photocurrent generation from two-dimensional WS_2 field-effect transistors, Appl. Phys. Lett. 104 (2014) 193113. https://doi.org/10.1063/1.4878335.

[104] A. Adha Sukma, S.-F. Pablo, J. Hyun Goo, F. Kenjiro, A. Hiroki, High Mobility WS2 Transistors Realized by Multilayer Graphene Electrodes and Application to High Responsivity Flexible Photodetectors, Adv. Funct. Mater. 27 (n.d.) 1703448. https://doi.org/10.1002/adfm.201703448.

CHAPTER 3

EXPERIMENTAL PROCEDURES

3.1 Introduction

This chapter briefly discusses the basic principle of physical vapor deposition techniques applied for thin-film growth in this thesis, the fundamental principles of material characterization techniques used in this study, and procedures in the growth and preparation of thin films used.

3.2 Physical Vapor Deposition (PVD) Techniques

These are deposition processes involving the transportation of atomic or molecular constituents vaporized from a solid (target) or liquid. This processing requires an ultra-high vacuum or low pressure, and/or a directional plasma of vaporized matters to impinge on a substrate. PVD is effective in thin-film processing, also can be used in both elemental and complex compound growth. PVD can be categorized into high vacuum depositions (e.g. Pulse laser depositions and Molecular beam epitaxy), sputter, arc vapor deposition, and ion plating [1].

3.2.1 Pulsed Laser Deposition PLD:

PLD deposition processes involve a setup of a pulsed laser, optics, a high vacuum chamber, target material, and a substrate. The laser is optically focused onto a rotating target as shown in Figure 3.1. The ablation process generates a plume that consists of atoms, diatoms, and low mass matter in form of a plasma. Typical PLD laser operates in the UV range and should be in 10 – 50 nanoseconds pulse width. During the PLD process, a series of events occur: Rapid heating and vaporization of the target, a high pressure region from adiabatic expansion from the target surface, increase energy absorption of vapor to transform into plasma, and absorption of energy to accelerate plasma [2]. PLD processes are unique for their congruent ablation of atomic species from a target; therefore improved stoichiometry is achievable as energetic species

impinge on the substrate. Reactive deposition with ambient gas and growth of multilayer structure is attainable [3]. Introducing background gas during PLD growth aims at either generating a reaction or slowing down the kinetics of the ablated species from the target material. The resulting energetics of the ablated species is dependent on the wavelength of the laser as the wavelength influences the penetration depth of the photon. This has been studied in the PLD growth of carbon using ArF and KrF lasers [4]. While congruent ablation is achievable in most materials during PLD, a stoichiometric film is not promising because the vapor pressure of atomic species will vary on a heated substrate.

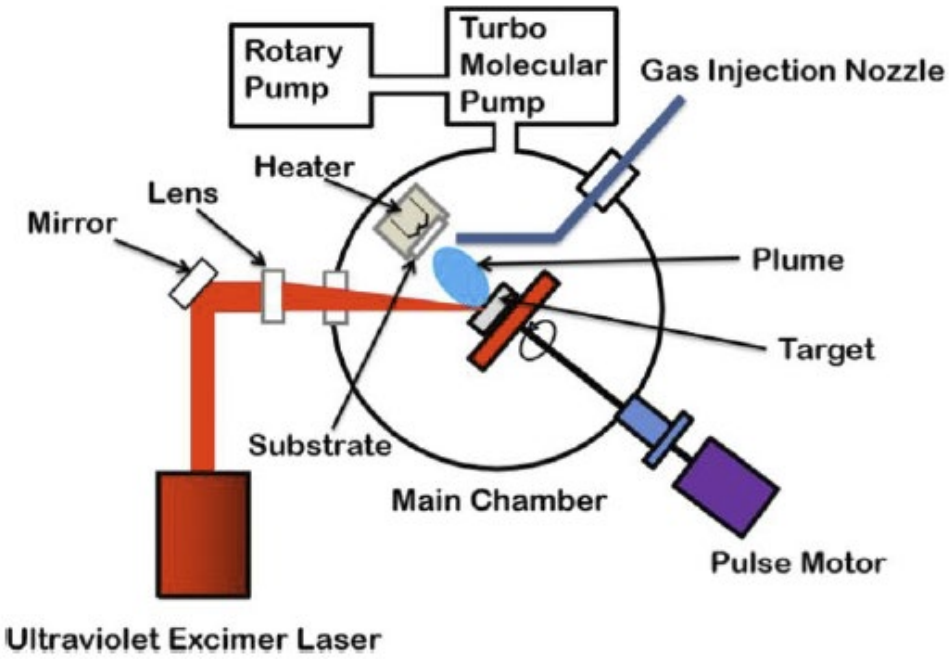

Figure 3.1: Schematic of PLD system [5].

PLD technique application includes the growth of complex compounds [6], epitaxial surfaces and interfaces, electronics, and others.

3.2.2 Radio Frequency Magnetron Sputtering:

The sputtering process is the ejection of particles from a target material by the energetic impingement of ionized gas. In the sputtering deposition, the ejected species attained kinetic

energy that accelerated to the substrate and confinement of the deposition chamber. Sputtering deposition starts by evacuating the sputter chamber to a base pressure of 10^{-6} Torr or lower. The purpose of chamber evacuation is to achieve low pressure to facilitate plasma formation with the transport of ions and electrons in space. This step also evacuates the system from undesirable impurities trapped in the deposition chamber. After a base pressure is accomplished, pure gas is backfilled at pressures in the range of 1 - 100 mTorr. The backfilled gas is the source of generating energetic ions during sputtering. The sputtering system includes a chamber, a target with negative potential, and a grounded substrate. Because an electric field is generated between the negatively biased target and positively charged ions in the plasma, the electric field drives the ions to the target surface, therefore, causing energetic bombardment.

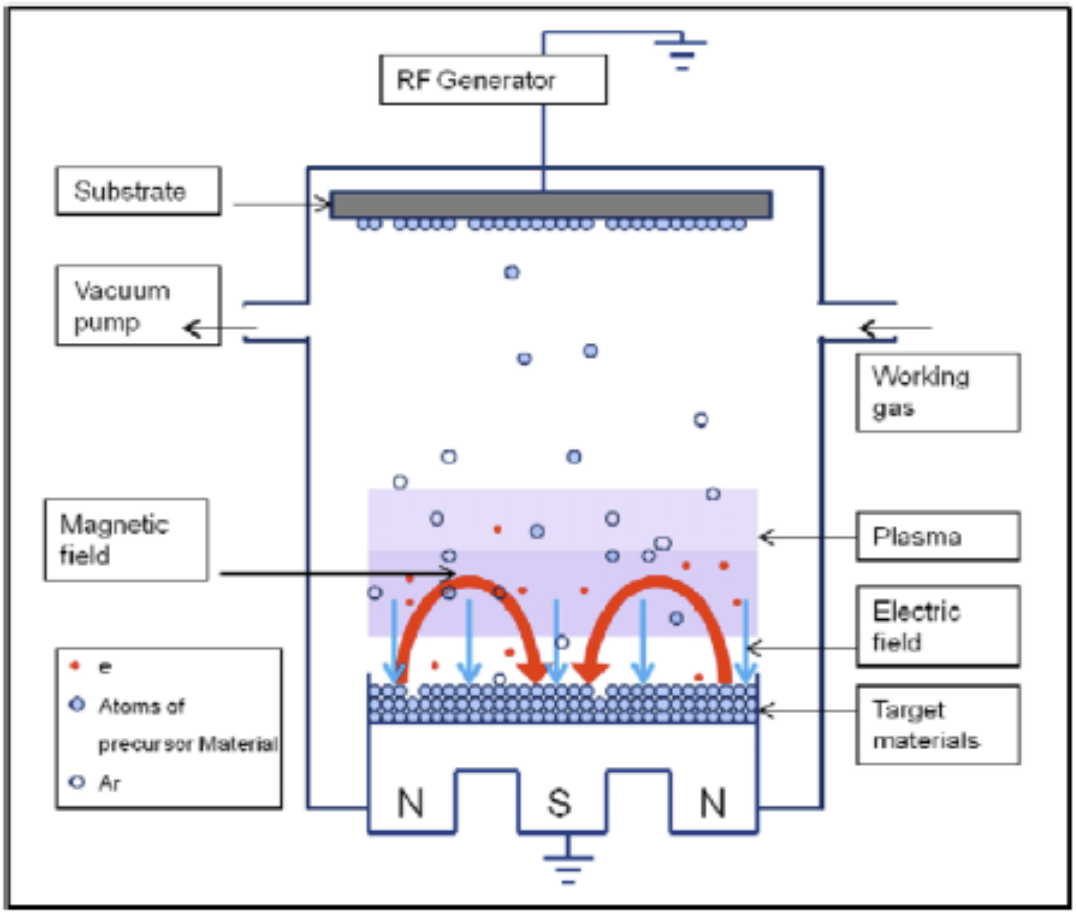

Figure 3.2: Schematic of rf magnetron sputtering system [7].

Radio frequency sputtering typically operates at frequencies ranging from 0.5 – 30 MHz. The commercial rf generator operates at 13.56 MHz. Rf sputtering requires a capacitively coupled target to the plasma; therefore, both insulators and conductors can be sputtered using this technique. The capacitive coupling during rf sputtering allows for alternating positive and negative potential on surfaces. This prevents charge buildup on the surface of the target as in the case of DC sputtering. The presence of a magnet in rf magnetron sputtering (Figure 3.2) creates a magnetic field that interacts with the electrically charged particles in the generated plasma. This increases plasma density and deposition rate. RF magnetron sputtering offers the advantage of synthesizing nonconducting films, large area depositions, dense films, good film uniformity, and adhesion to the substrate.

3.2.3 Thermal Evaporation

Thermal evaporation is a process whereby atoms and/molecules are vaporized on a substrate by applying thermal energy to the source material in a vacuum environment. Thermal energy may be supplied by high energy electron bombardment, resistive of material, radiative heating from a high energy source, or heating with a laser. This process requires a reasonable vacuum to allow for a long mean free path of the vaporized matter to impinge on the substrate. As shown in Figure 3.3, thermal evaporation by resistive heating is dependent on the vapor pressure of the material being evaporated. Resistive heating is used to vaporize materials below 1500^{o}C. The evaporated material is placed in a high-temperature boat made of Mo, Ta, or W.

The vapor pressure is thermodynamically in equilibrium with the solid or liquid surface of a material in a closed system at a given temperature. Figure 3.4 shows a chart of the vapor pressures of elements. For metals used in this dissertation (i.e. Al, Ag, and Au), the temperature required for evaporation fall between 600 – 1000^{o}C at a vapor pressure of 10^{-6} Torr.

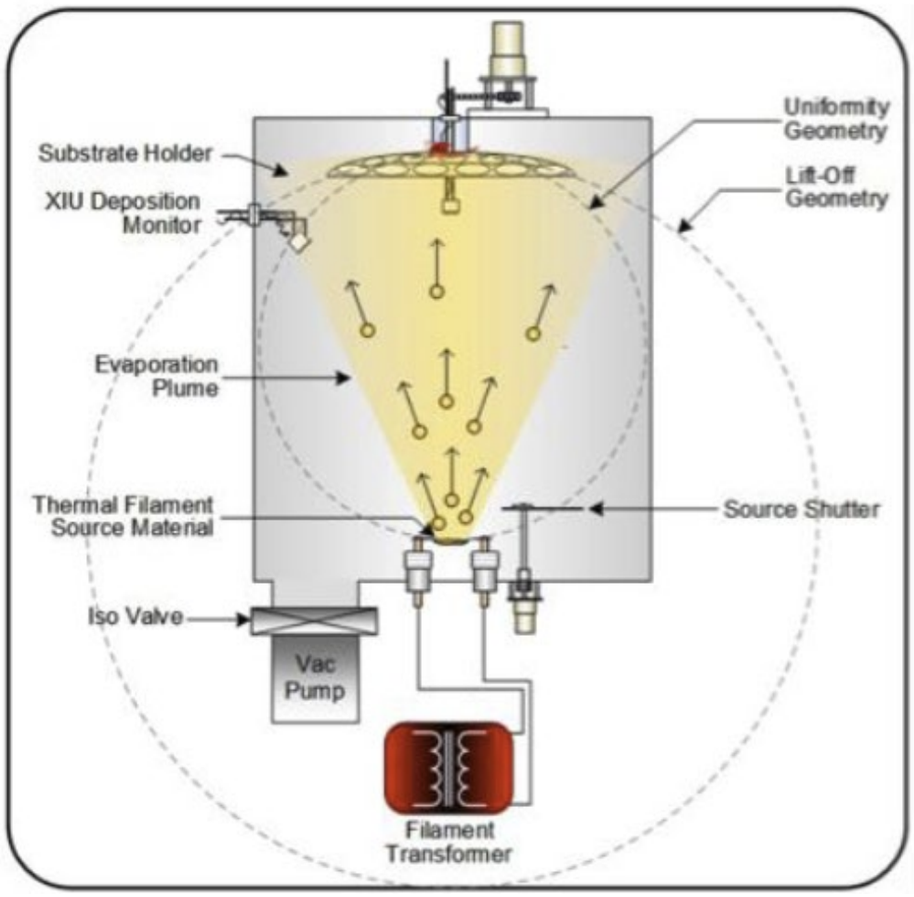

Figure 3.3: Schematic of thermal evaporation system. Source: http://www.semicore.com/news/71-thin-film-deposition-thermal-evaporation

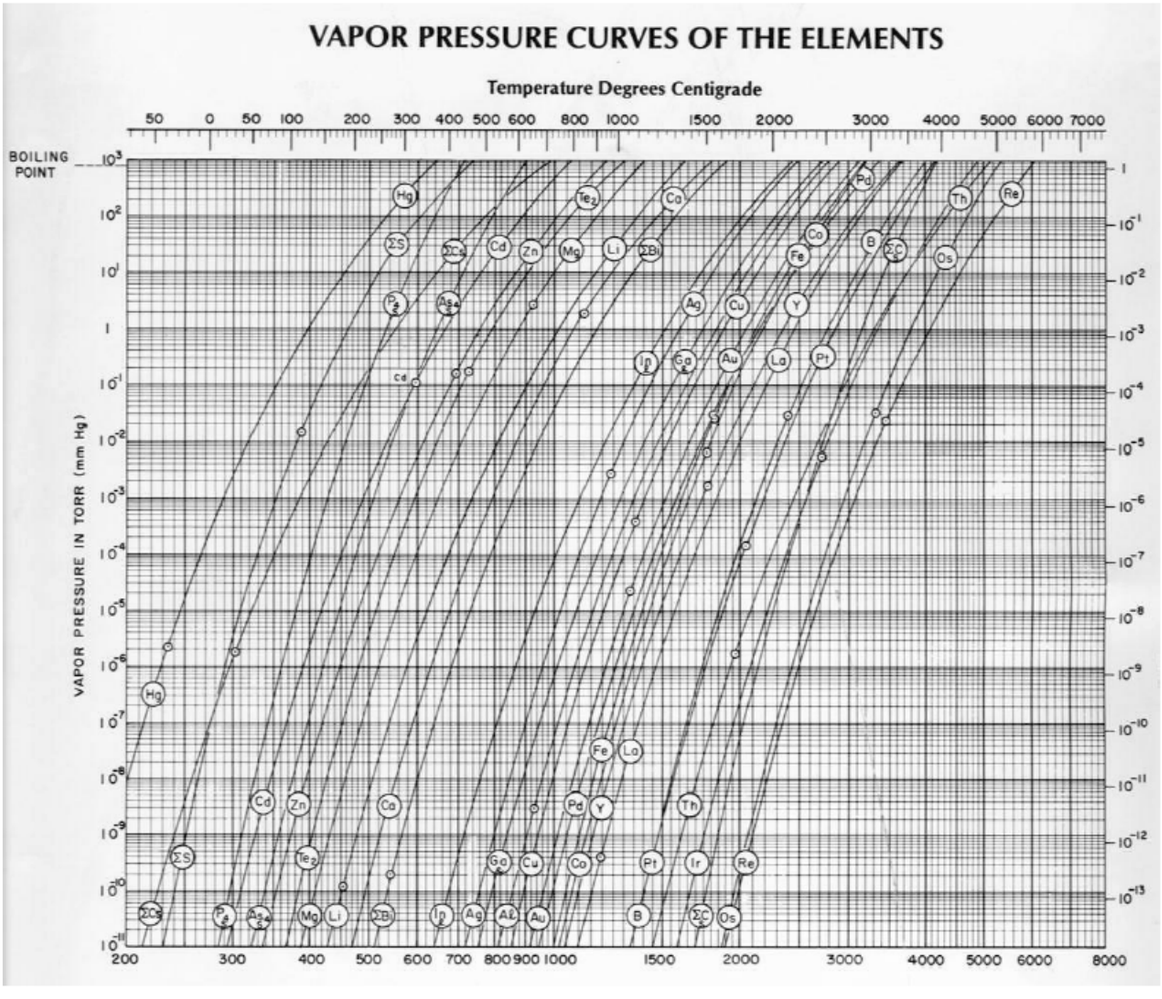

Figure 3.4: Vapor pressure of elements. Source: https://www.hubnames.com/wp-content/uploads/2016/03/vapor4.jpg

3.3 Characterization Techniques

In this section, material characterization techniques applied in this work are briefly described. The description includes the principles, basic mechanism, and instrumentation. Techniques applied in this work discussed here include XRD, XPS, Raman Spectroscopy, AFM, Spectroscopy Ellipsometer, Hall measurement, and Photoluminescence.

3.3.1 X-ray Diffraction Spectroscopy (XRD)

XRD technique characterizes material structure. This is a non-destructive technique that requires simple sample preparation. The principle of XRD is from Bragg's law: $n\lambda = 2d \sin \theta$; where: n is an integer and is the order of reflection, λ is the wavelength of the x-ray source ranges between 0.7 – 2 Å, d is the interplanar spacing and θ is Bragg's angle. Figure 3.5 describes x-ray interaction with a solid plane. When an x-ray interacts with a material, part of it gets absorbed, transmitted, or diffracted. XRD measures the intensity of the diffracted x-ray. The angle of diffraction is twice Bragg's angle. XRD techniques can determine strain states, orientation, and structural defects in thin films.

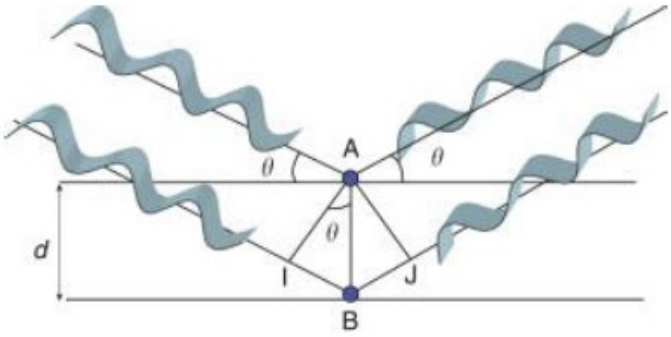

Figure 3.5: Schematic of Bragg's law. Source: https://www.sciencedirect.com/science/article/pii/B9780123744135003596

3.3.2 X-ray Photoelectron Spectroscopy (XPS)

Fundamental to XPS analysis is the photoelectric effect. XPS is a non-destructive

technique for surface analysis. The penetration depth ranges between 5 – 50 Å. In this process, an incident x-ray source of energy $\hbar w$ up to 10 KeV is absorbed in the material. This absorbed energy is high enough to break the binding energy E_b of the bound electron, and the electron gains kinetic energy E_k to break loose from the material: $E_k = \hbar w - E_b - \varphi_s$. where φ_s is instrument workfunction. The unique binding energy of elements makes XPS a technique for chemical analysis. With the available ranges of photon energy that fall between the UV and x-ray wavelengths, this technique can be used for the analysis of inner shell electrons and as well less tightly bound electrons of the outer shell.

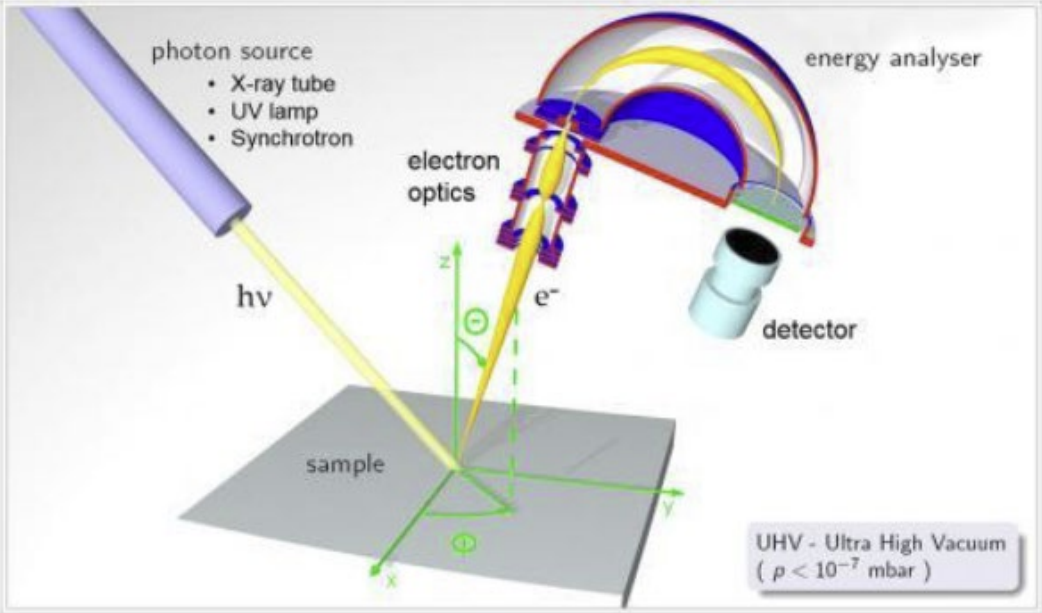

Figure 3.6: Schematics of XPS. Source: https://ywcmatsci.yale.edu/xps

As illustrated in Figure 3.6, XPS setup comprises of an x-ray source usually a monochromatic Mg or Al kα source, a sample mount, electron optics, analyzer, and a detector. The electron optics/lenses slow down ejected electrons before arriving at the analyzer; this, in turn, improves energy resolution. The energy of a photoelectron is determined in an analyzer, and it determines the deflection of a photoelectron in an electrostatic or magnetic field. A commonly used analyzer is a hemispherically shaped unit composed of two concentric sectors with applied potential,

where no change in potential occurs when an electron passes through [8]. Electrons at the exit end of the analyzer are collected and multiplied by a channeltron which amplifies the electron count transmitted to the computer.

3.3.3 Atomic Force Microscopy (AFM)

AFM techniques use an atomically sharp tip mounted on a cantilever to scan across the surface of materials to capture images of the topography. In this work, the cantilever tip is Si with Al coated backside, and scans were set to tapping mode. The force constant of the cantilever is 40 N/m. Atomic interaction between sample and tip results in a deflection of the tip from repulsive van der Waal forces. As illustrated in Figure 3.7, the light from a diode laser is reflected from the backside of the cantilever. The reflected light is captured on a photodiode. A piezoelectric transducer is used to scan and maintain a constant tip to sample distance. Benefits of AFM include highly resolved topographies, profilometries, and phase scans.

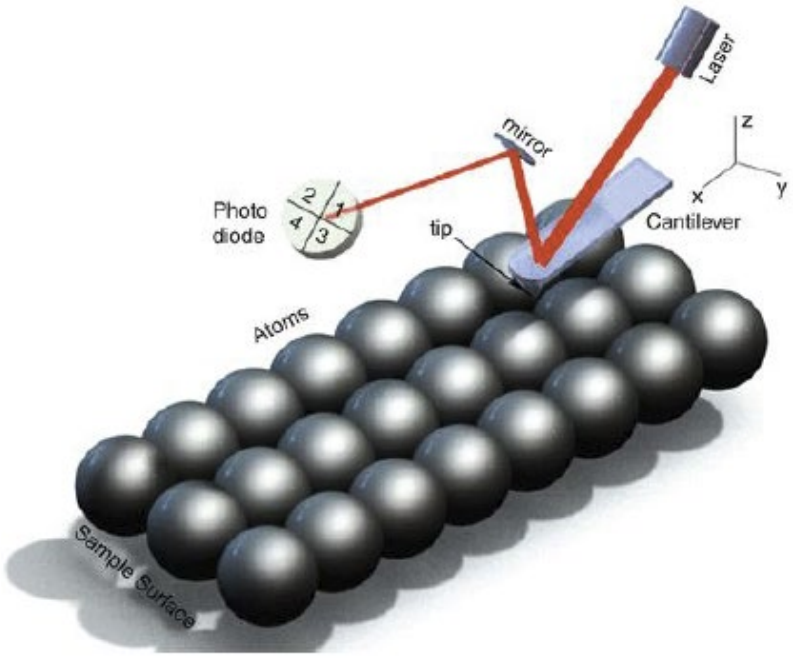

Figure 3.7: AFM Schematics. Source: https://media.springernature.com/lw785/springer-static/image/prt%3A978-0-387-92897-5%2F1/MediaObjects/978-0-387-92897-5_1_Part_Fig1-1213_HTML.gif

3.3.4 Raman Spectroscopy

Raman spectroscopy is based on the principle of Raman scattering. It is used in structural and stress analysis in films. Also by varying the wavelength of the light source, profiling can be achieved with this technique. In this technique, a monochromatic light interacts with the chemical bonding and lattice of a material. During this process, light is scattered from the surface of the sample. A significant amount of the light is radiated away from the sample at the same frequency as the light source. This is designated the Rayleigh line. The Raman and Brillouin lines are reradiated light with frequencies lower than the light source. Raman lines arise from the vibrations of optical phonons in the structure of materials while Brillouin lines are a result of acoustic phonons. The Raman scattering consists of the stokes and anti-stoke shift. In the stokes shift, the Raman line is emitted at lower energy while the vice-versa occurs in the case of an anti-stoke shift. A double monochromator is used to reject the Rayleigh scattering.

3.3.5 Photoluminescence Spectroscopy (PL)

PL is a non-invasive technique that is used to qualitatively study defect or impurity levels in materials. Materials emit light at specific wavelengths and intensity as a result of optical stimulation. The high sensitivity of PL can detect impurity traces in materials. During a PL measurement, light excites an electron from an initial state to a higher state. At a relatively high state, the electron relaxes non-radiatively to a lower excited state like the bottom of the conduction band. Further relaxation back to the ground states termed recombination results in light emission in the case of luminescent materials. In semiconductors, PL is capable of detecting electrons bounded to a hole, i.e. excitons, and other defect levels.

3.3.6 Hall Measurement

The Hall measurement technique is applicable in obtaining conductivity, carrier

concentration, and mobility of a conducting material. This results from the hall effect as described in Figure 3.8 [9]. Hall effect is described by applied magnetic field perpendicular to the direction of the current produces a voltage perpendicular to both the magnetic field and current applied. This results in carrier deflection. The applied magnetic field induces a Lorentz force described by the equation: $\mathbf{F} = q(\mathbf{E} + \mathbf{v} \times \mathbf{B})$, where **F** is the Lorentz force, **E** is the electric field, **v** is the velocity of charge carrier, **B** is the magnetic field applied and q is the charge of a particle. The deflection of carriers (holes and electrons) induces a potential difference which results in a measure of the Hall voltage V_H. Contacts on samples were made using the acceptable Van der Pauw technique described in Figure 3.9(b) [10].

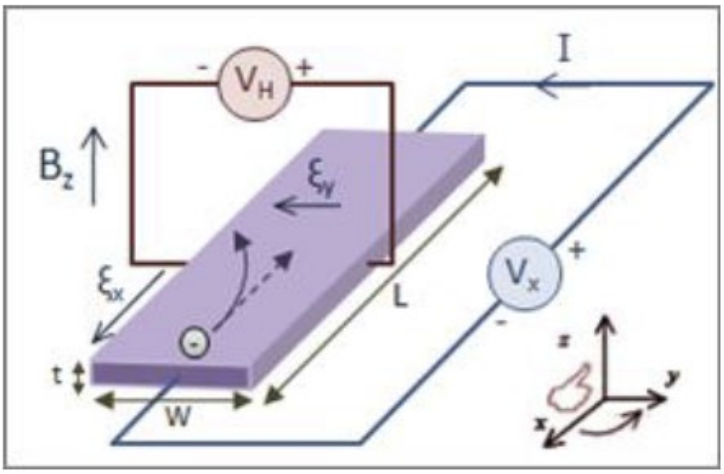

Figure 3.8: Schematics of Hall effect. Source: https://en.wikipedia.org/wiki/Hall_effect

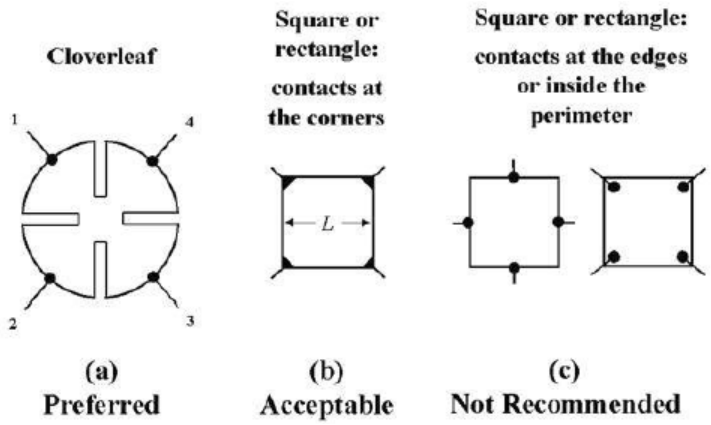

Figure 3.9: Van der Pauw technique. Source: Van der Pauw method - Wikipedia

A good sample setup for Hall measurement would require ohmic contact achieved, sample thickness uniformity, accurate measurement of thickness, and also for photoconductive sample, a dark current measurement.

3.3.7 Spectroscopy Ellipsometry

Ellipsometry is a non-destructive, contactless technique used to characterize the thickness, optical, and dielectric properties of a material. An ellipsometer setup comprises a light source, a linear polarizer, a retarder, the sample, an analyzer, and a detector. Its principle as illustrated in Figure 3.10 is based on the change in polarization of an incident light after it is reflected from a sample at an oblique angle. Ellipsometry determines the complex reflection ratio ρ of material; $\rho = \frac{R_p}{R_s} = \tan(\Psi)\, e^{j\Delta}$. Where: R_p is the ratio of the reflected and incident parallel component of the electric field, R_s is the ratio of the reflected and incident vertical component of the electric field, Ψ is the ellipsometry variable which measures the amplitude ratio ($0^o \leq \Psi \leq 90^o$), Δ is a measure of the phase change ($0^o \leq \Delta \leq 360^o$), and $j = (-1)^{1/2}$. Optical properties, n, and k can be extracted by applying Fresnel's equations [11].

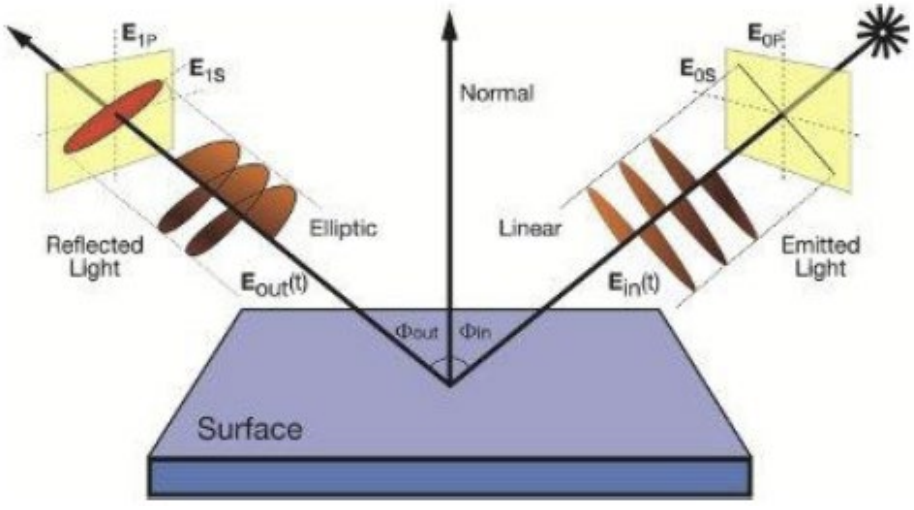

Figure 3.10: Schematic of the principle of Ellipsometry. Source: https://media.americanlaboratory.com/m/20/article/138874-fig1.jpg

3.4 ZnO Film Growth

ZnO thin films were grown at room temperature on flexible Corning Willow glass by radio frequency magnetron sputtering using a 5 cm diameter high purity commercial ZnO target (Kurt Lesker 99.999%), and a 13 cm source to substrate separation. Before growth, the substrates were ultrasonically cleaned with acetone and methanol, separately, for 10 minutes then blown dry by nitrogen gas. The base pressure of the deposition system was 1.5×10^{-6} Torr.

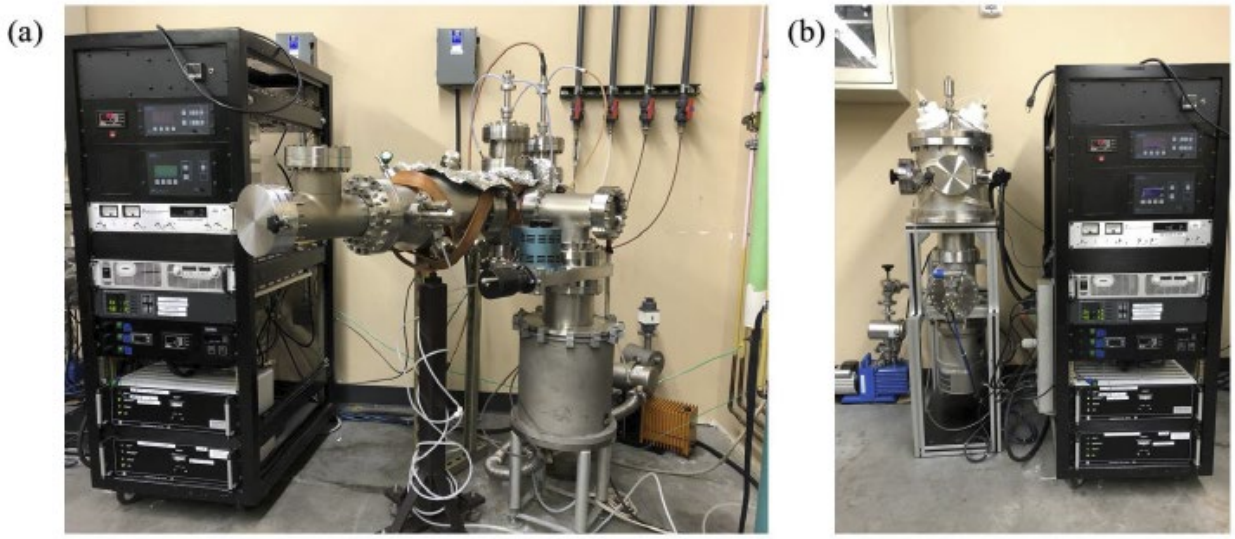

Figure 3.11: PVD systems: (a) rf magnetron sputtering, (b) Metal evaporator.

Figure 3.11(a) shows the image of the sputtering system used in this work. Sputtering was performed for 40 minutes at powers of 40 W, 100 W, and 120 W at constant argon working pressure of 3 mTorr, and the second set of samples was prepared at a constant power of 100 W while the working pressure was varied at 3 mTorr, 6 mTorr, and 9 mTorr. These conditions produced films in the 500-600 nm range. Film thickness was determined with a Veeco Dektak 150 stylus profilometer. Electrical measurements were performed using an Ecopia HMS5000 Hall measurement system. Optical properties were obtained using a Shimadzu UV-1800 UV–Vis spectrophotometer and a reconfigurable photoluminescence system that has been previously described. A PHI 5000 Versaprobe X-ray photoelectron spectroscopy (XPS) spectrometer with

monochromatic 1,486.6 eV Al Kα radiation was used for chemical analysis. The spectral position was calibrated using the C 1s peak at 284.8 eV, and the energy resolution was 0.1 eV. Crystallinity was evaluated using the 1.54Å Cu Kα1 line of a Rigaku Ultima III X-ray powder diffraction (XRD).

3.5 *a*-BO_xN_y Film Growth

The studied transparent MIS structures consisted of glass/ITO/*a*-BO_xN_y/ZnO stacks where the ITO layer is considered metallic due to its degenerate electron concentration of 6×10^{20} cm^{-3}, and ohmic contact to the ZnO semiconductor was achieved using thermally evaporated 7.85×10^{-3} cm^2 Ag pads. The metal evaporator system is as shown in Fig. 3.11 (b). Before use, the commercial ITO coated glass substrates were ultrasonically cleaned in acetone and methanol separately for 10 min, rinsed in DI water, then blown dry with nitrogen gas. The rf magnetron sputtering conditions for the ZnO and *a*-BO_xN_y layers were separately optimized before implementation in MIS structures for electrical studies. The base pressure of the deposition chamber was 1.5×10^{-6} Torr and substrates were mounted at a fixed position without rotation. The *a*-BO_xN_y films were grown at room temperature with a 45° off-axis target to substrate separation of 2.5 cm. The working gas was semiconductor-grade nitrogen, and the commercially available BN target (from Plasmaterials Inc) was 5 cm in diameter and 99.5 % pure. The power was kept constant at 284 W, while pressures of 2, 5, 10, and 15 mTorr were used. All of the *a*-BO_xN_y films studied were 34 (±4) nm. The ZnO films in the MIS structures were ~22 nm and were also grown by rf magnetron sputtering without substrate heating at 100 W in 9 mTorr of argon gas as has been detailed elsewhere. These films exhibited transparency of 85% and typical electron concentrations of 10^{18} cm^{-3}. The breakdown behavior of the *a*-BO_xN_y films was studied using MIM structures consisting of *a*-BO_xN_y films sandwiched between ITO and ~50 nm of

thermally evaporated Ag. Film thickness was determined with a Veeco Dektak 150 stylus profilometer. Electrical measurements were performed using an Ecopia HMS5000 Hall measurement system, a Keithley 2420 source-measure unit integrated with LabVIEW, a capacitance meter, and an Agilent 4294A precision impedance analyzer. Bandgaps were determined from absorbance data obtained using a Shimadzu UV-1800 UV–Vis spectrophotometer, and verified by ellipsometry using a J.A. Woollam Variable Angle Spectroscopic Ellipsometer (VASE). A PHI 5000 Versaprobe X-ray photoelectron spectrometer with monochromatic 1,486.6 eV Al Kα radiation was used for XPS chemical analysis. The structure was evaluated using the 1.54 Å Cu Kα1 line of a Rigaku Ultima III x-ray diffraction (XRD) system with conventional θ-2θ scans and a 2º glancing angle scan. Surface topography was characterized using a Bruker Nanoscope® V AFM.

3.6 WS_2 Film Growth

Few layer WS_2 films were grown using a polycrystalline WS_2 target purchased from Kurt J. Lesker and an in-house fabricated target. The in-house fabricated target was made by ball mixing 99.98% Sulphur powder and 99% WS_2 powder (both purchased from Aldrich) for 24 hrs on a roller mill. After thorough mixing, the mixture was pressed in a die at 70ºC for another 24 hrs [12]. The in-house made target is sulfur-rich with an atomic ratio of Sulfur to Tungsten S/W ~5:1. Before deposition, quartz and ITO/glass substrates were ultrasonically cleaned in acetone and methanol for 10 min separately and rinsed in DI water. After rinsing, substrates were nitrogen blown to dry and immediately mounted in the chamber with the in-house made target. The deposition chamber was baked out for 12 hrs and a base pressure of 10^{-6} Torr was achieved. Figure 3.12 shows the actual chamber setup.

Figure 3.12: PLD System.

Here the PLD chamber window is positioned in line with the laser output. A lens is used to focus the laser onto the target. Substrates temperature ranged from room temperature to 400^{o}C before deposition and the target was pre-ablated to clean its surface. During deposition, the target was rotated at 10 rpm. A 25 ns pulse, 248 nm KrF line excimer laser manufactured by Lambda Physik was the source of target ablation. Power density and frequency were set to 0.5 J/cm^2 and 10 Hz respectively during film depositions. After deposition films were allowed to achieve atmospheric temperature under vacuum in 1 hr. Chemical characterization was done using a PHI 5000 Versaprobe X-ray photoelectron spectrometer (XPS) with monochromatic 1,486.6 eV Al Kα radiation. Structure characterization was carried out using the 1.54 Å Cu Kα1 line of a Rigaku Ultima III x-ray diffraction (XRD) system at a 0.5^{o} glancing angle scan. Raman vibration

was measured using a 532 nm Renishaw RA100 spectroscopy. The Ecopia HMS5000 Hall measurement system was used to measure the carrier properties of grown WS_2 films. A Keithley 2420 source-measure unit integrated with LabVIEW was used to measure the current-voltage characteristics of the Metal-Insulator-Semiconductor (MIS) structure. Capacitance and conductance measurements were done using an Agilent 4294A precision impedance analyzer. A Bruker Nanoscope® V AFM was used to investigate film topography.

3.7 References

[1] M. Donald M., Handbook of physical vapor deposition (PVD) processing, William Andrew, n.d.

[2] L. Douglas H., G. D. B., P. A. A., N. D. P., R. C. M., Synthesis of novel thin-film materials by pulsed laser deposition, Science (80-.). 273 (n.d.) 898–903.

[3] H.M. Christen, G. Eres, Recent advances in pulsed-laser deposition of complex oxides, J. Phys. Condens. Matter. 20 (2008). https://doi.org/10.1088/0953-8984/20/26/264005.

[4] P. A. A., G. D. B., J.J. G. E., M. M. M., Comparative diagnostics of ArF-and KrF-laser generated carbon plumes used for amorphous diamond-like carbon film deposition, Appl. Surf. Sci. 96 (n.d.) 859–865.

[5] M. Khalid Bin, K. Pushpendra, M. Mushtaq Ahmad, S. Jai, A comprehensive tutorial on the pulsed laser deposition technique and developments in the fabrication of low dimensional systems and nanostructures, Emergent Mater. (n.d.) 1–18.

[6] H.M. Christen, Pulsed Laser Deposition of YBa2Cu3o7-x For Coated Conductors Applications: Current Status and Cost Issues, To Be Publ. “Next Gener. High Temp. Supercond. Wires” A. Goyal (Ed.), Kluwer Acad. Publ. (2001).

[7] R. Bosco, J. V. Van Den Beucken, S. Leeuwenburgh, J. Jansen, Surface engineering for bone implants: A trend from passive to active surfaces, Coatings. 2 (2012) 95–119. https://doi.org/10.3390/coatings2030095.

[8] F. Leonard C., M. James W., Fundamentals of surface and thin film analysis, North Holland, Elsevier Sci. Publ. P. O. Box 211, 1000 AE Amsterdam, Netherlands, 1986. (n.d.).

[9] On a New Action of the Magnet on Electric Currents Author (s): E . H . Hall Published by : The Johns Hopkins University Press Stable URL : https://www.jstor.org/stable/2369245 On a New Action of the JIa19flet onz Electric Currents . SOMETIME during the , 2 (1879) 287–292.

[10] Y. Sun, J. Shi, Q. Meng, Measurement of sheet resistance of cross microareas using a modified van der Pauw method, Semicond. Sci. Technol. 11 (1996) 805–811. https://doi.org/10.1088/0268-1242/11/5/025.

[11] J. Skaar, Fresnel equations and the refractive index of active media, Phys. Rev. E - Stat. Nonlinear, Soft Matter Phys. 73 (2006) 1–7. https://doi.org/10.1103/PhysRevE.73.026605.

[12] R. Urmila P., E. Justin, V. Andrey A., S. Nigel D., Extrinsic p-type doping of few layered WS2 films with niobium by pulsed laser deposition, Appl. Phys. Lett. 113 (n.d.) 062106.

CHAPTER 4

LOW TEMPERATURE GROWTH OF ZnO THIN FILMS*

4.1 Objective:

Determine the processing conditions for low-temperature RF magnetron sputtered ZnO with optimal topography, chemistry, structure, optical, and semiconducting properties for evaluation in MIS structure for potential use as a channel material in transparent thin film transistors. Perform structural, chemical, electrical, and optical characterization as previously described.

4.2 XRD Result:

Figure 4.1 (a) shows the measured XRD patterns for films grown at 40, 100, 120 W at a constant working pressure of 3 mTorr, while 1(c) represents XRD data for films grown at 3, 6, and 9 mTorr at a constant sputtering power density of 100 W. The films were hexagonal and nanocrystalline, where predominant (002) growth was observed only for sputtering at 40 W. More orientations appeared as the deposition power was increased. The (002) peak location shifted toward larger 2θ values with increasing power (instrument resolution was set to 0.05º/step) [Figure 4.1(b)]; it increased from 33.72º at 40 W to 33.86º at 100 W, and further to 34.02º at 120 W, and thus approached the value for relaxed bulk ZnO [1]. This shift has been correlated with a reduction in internal stresses [2,3] and the relaxation is possibly driven by more energetic peening and local temperature increases of the growing films due to the power density increase. A similar shift with increasing deposition temperature has been reported [4]. In

* Significant amounts of this chapter are reproduced from Chukwudi E. Iheomamere, Corey L. Arnold, Urmilaben P. Rathod, Khalil D. Omotosho, Andrey A. Voevodin, Nigel D. Shepherd, (2021), Bonding and stoichiometry in low-energy radio frequency magnetron sputtered ZnO thin films on flexible substrate, Vacuum, 183, 109869. https://doi.org/10.1016/j.vacuum.2020.109869https://doi.org/10.1016/j.vacuum.2020.109869, with permission from Elsevier.

general, the XRD shows that for the higher power settings, multiple orientations nucleate and grow simultaneously; which is consistent with the increase of the deposition flux density and the insufficiency of substrate heating to accelerate surface diffusion, coalescence, and ripening. A closer examination of Figure 4.1(a), reveals that the intensity of the (002) decreases as the sputtering power increases [5], and conversely as seen in 1(c), the (002) plane became more prominent with increasing working pressure, although texturing is not observed. Lower sputtering power leads to a reduction in the overall flux density of the arriving species and can be expected to provide more time for their surface diffusion. Furthermore, increased pressures in rf sputtering lead to a higher density of the working gas and probability of its ionization, while also slowing the kinetic energies of sputtered Zn, O, and ZnO species by collisions. Since ZnO (002) planes are the most densely packed and thermodynamically preferred in the hexagonal structure, it is reasonable that (002) growth is favorable under the reduced power and higher working pressures. This correlates with previous reports on sputtered ZnO films, where increased pressure led to more pronounced (002) texturing [6][7].

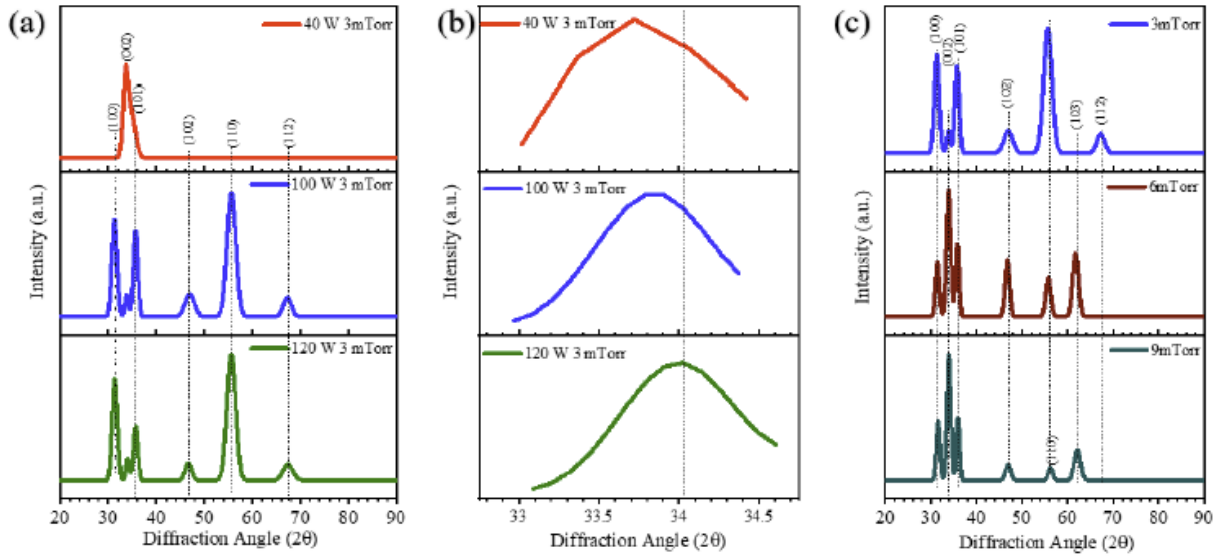

Figure 4.1: (a) XRD spectra as a function of sputtering power at a constant 3 mTorr working pressure, (b) Detailed view of the (002) peak shift as a function of sputtering power, (c) XRD spectra as a function of working pressure at a constant 100 W sputtering power.

4.3 AFM Result

AFM images in Figure 4.2show films are nanoparticles size. Increasing the deposition power show an increase in particle sizes. This suggests that energy generated from the plasma transfers to atoms arriving at the substrate. At higher energies, atomic species acquire energy from plasma and increased radiative heat transfer to promote the diffusion of impinging atoms on the substrate. It is expected that the mean free path of sputtered species and the momentum of atomic impingement play significant roles in films morphologies, more energetic conditions will increase atomic bombardment at the substrate.

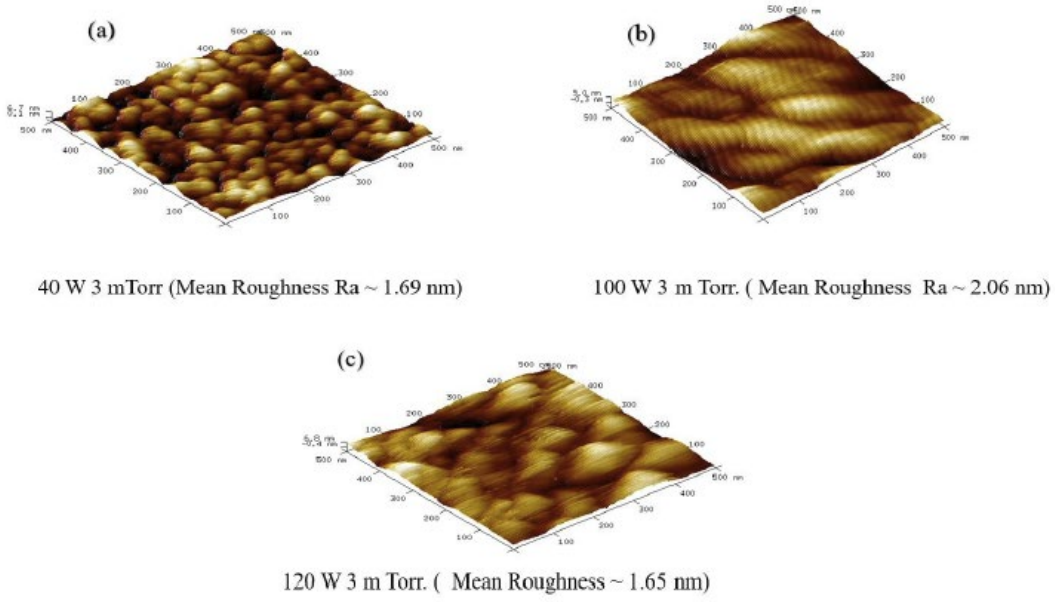

Figure 4.2: AFM images of ZnO films grown at various rf power.

4.4 Electrical Measurement:

The correlations between processing conditions and obtained electrical properties are summarized in Figures 4.3 and 4.4, and Tables 4.1 and 4.2. The data shows that the highest carrier concentration, conductivity, and mobility were obtained with the *least* dense and energetic growth conditions, that is, at the lowest sputtering power, or the highest working

pressure. These findings were not expected because native n-type conduction in ZnO is known to be due to oxygen vacancies (or Zn interstitials) [8] which act as donors, and more of these defects can be expected from processing under more energetic conditions. XPS studies were therefore performed to develop more insight into the chemical origins of this behavior.

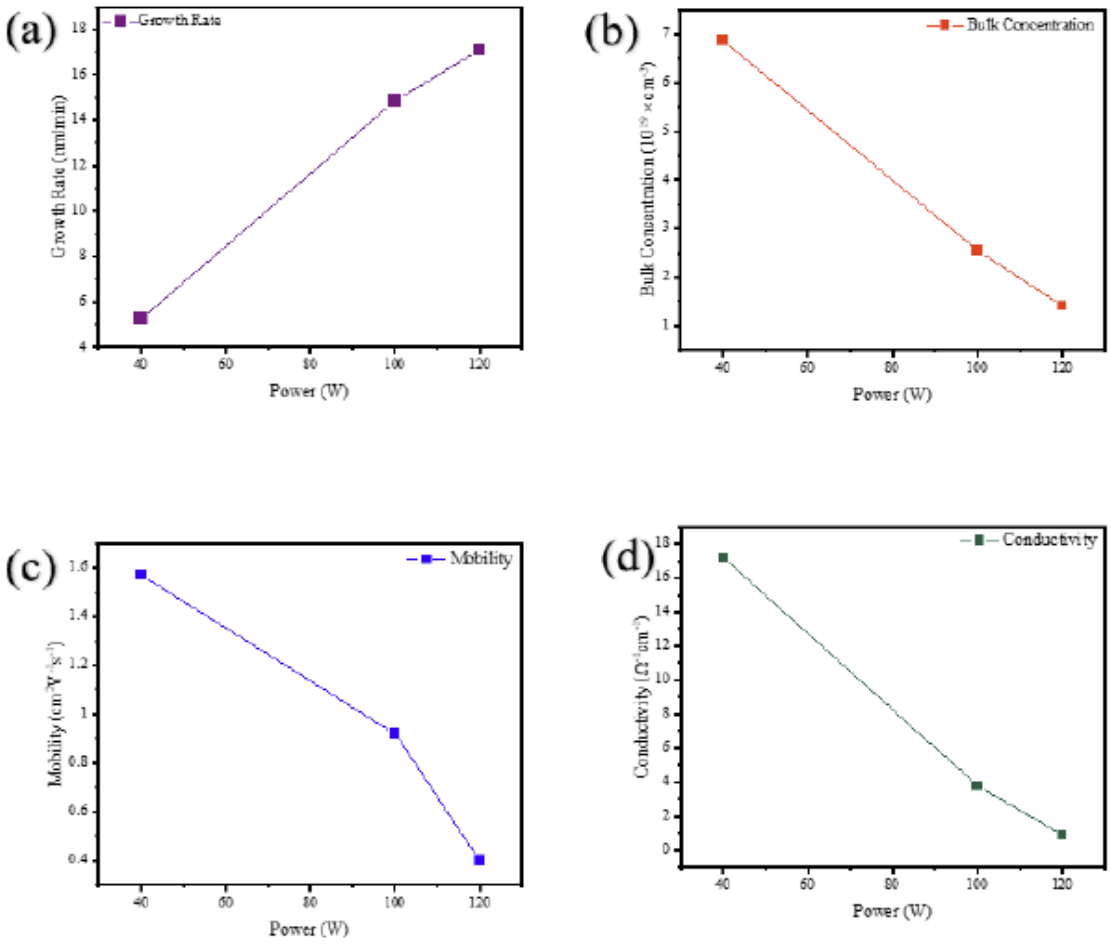

Figure 4.3: Growth rate, carrier concentration, mobility, and conductivity of ZnO films: (a - d) as a function of power at a working pressure of 3 mTorr.

Table 4.1: Properties as a function of power at a constant pressure of 3 mTorr

Power (W)	Thickness (nm)	Bulk carrier concentration $\times 10^{19}$(cm^{-3})	Conductivity ($\Omega^{-1}cm^{-1}$)	Mobility ($cm^2V^{-1}s^{-1}$)	Absorption edge (eV)
40	499	-6.9	17	1.6	3.32
100	505	-2.6	4	0.9	3.20
120	616	-1.4	1	0.4	3.24

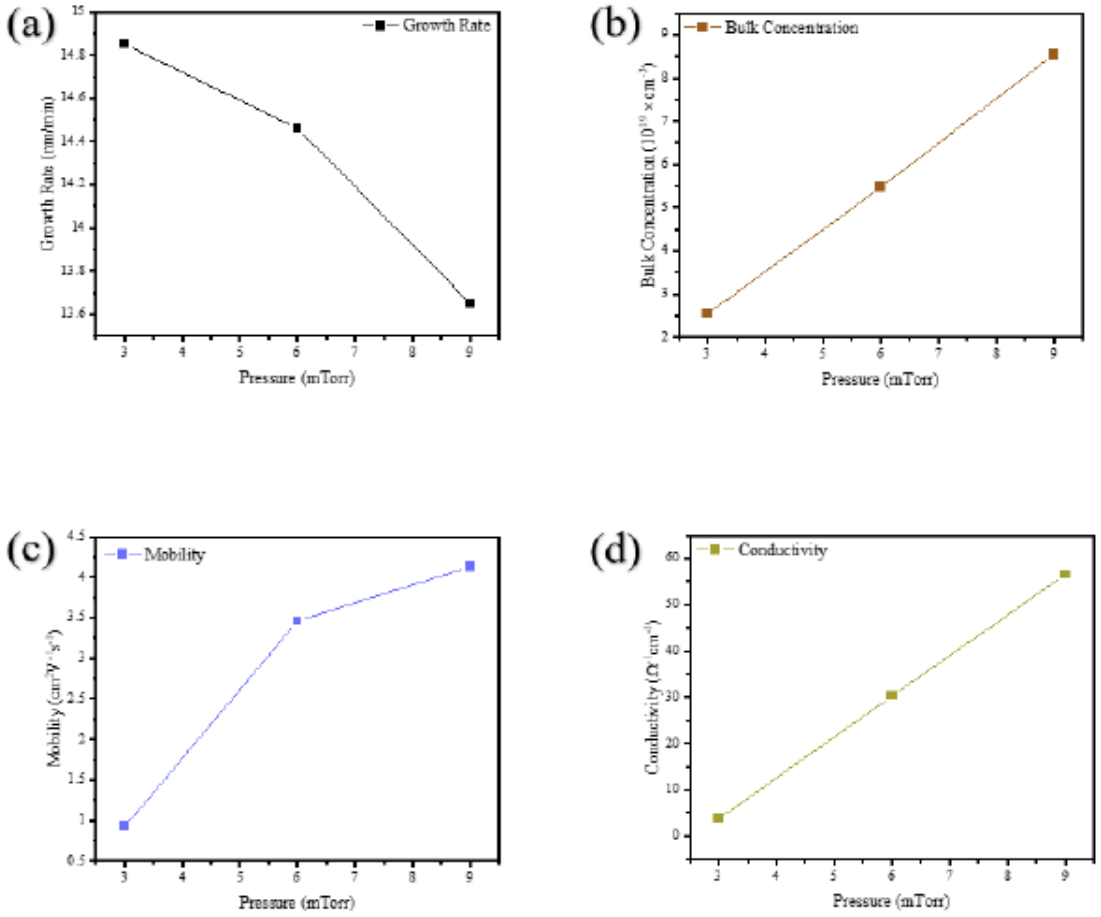

Figure 4.4: Growth rate, carrier concentration, mobility, and conductivity of ZnO films: (a – d) as a function of working pressure at a power of 100 W.

Table 4.2: Properties as a function of deposition pressure at a constant power of 100 W

Working pressure (mTorr)	Thickness (nm)	Bulk carrier concentration $\times 10^{19}$ (cm^{-3})	Conductivity ($\Omega^{-1}cm^{-1}$)	Mobility ($cm^2V^{-1}s^{-1}$)	Absorption edge (eV)
9	510	-8.6	57	4.1	3.32
6	564	-5.5	30	3.5	3.30
3	505	-2.6	4	0.9	3.20

4.5 XPS Analysis

Figures 4.5 and 4.6 show the measured XPS spectra for the processing power and working pressure experiments, respectively. Zn was only observed in the Zn^{+2} oxidation state at

a binding energy of 1021.4 eV [4] whereas asymmetry was observed in the oxygen signal indicating that more than one oxygen species was contributing. Deconvolution of O1s XPS spectra shows oxygen stoichiometrically bonded to Zn (O-Zn) with binding energy 530 eV [9] non-stoichiometrically bonded oxygen with Zn (V_o) at a binding energy 531 eV [10] and O1s (OH, C-O, O-O) surface oxygen with binding energies of 532 eV and above [9–12]. Tables 4.3 and 4.4 summarize the XPS results. The data in Table 4.3 show that as sputtering power increased, the amount of stoichiometric O-Zn bonding increased; while the oxygen deficient bonding, meaning oxygen vacancies (V_O) decreased. As shown in Figure 4.6 and Table 3.4, as the working pressure increased the fraction of stoichiometric O-Zn bonds decreased while the oxygen deficient bonding increased. Under equilibrium conditions, it is expected that $V_o^{2\bullet}$ should increase with a decrease in partial pressure of oxygen as depicted in the defect equation: ($ZnO \rightarrow ZnO_{(1-x)} + \frac{x}{2}O_2(gas) + xV_o^{2\bullet} + 2xe'$). The existence of n-type behavior in the ZnO films is due to the non-stoichiometry in the grown films.

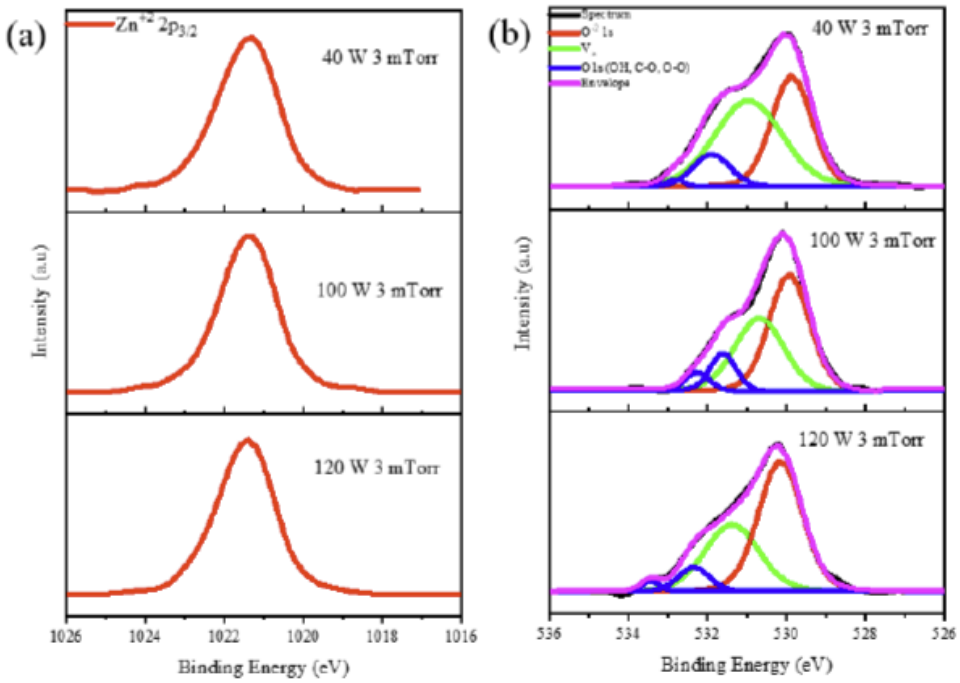

Figure 4.5: XPS for ZnO films grown at varied powers, (a) Zn $2p_{3/2}$, (b) O 1s.

Table 4.3: Composition of ZnO films as a function of sputtering power.

Sputtering power (W)	Zn^{2+} 2p (%)	Stoichiometric O-Zn (%)	Non-stoichiometric oxygen (%)	O1s (OH, C-O, O-O) oxygen (%)
40	58.8	15.9	20.6	4.7
100	58.8	20.0	15.2	6.0
120	59.6	22.5	14.2	3.7

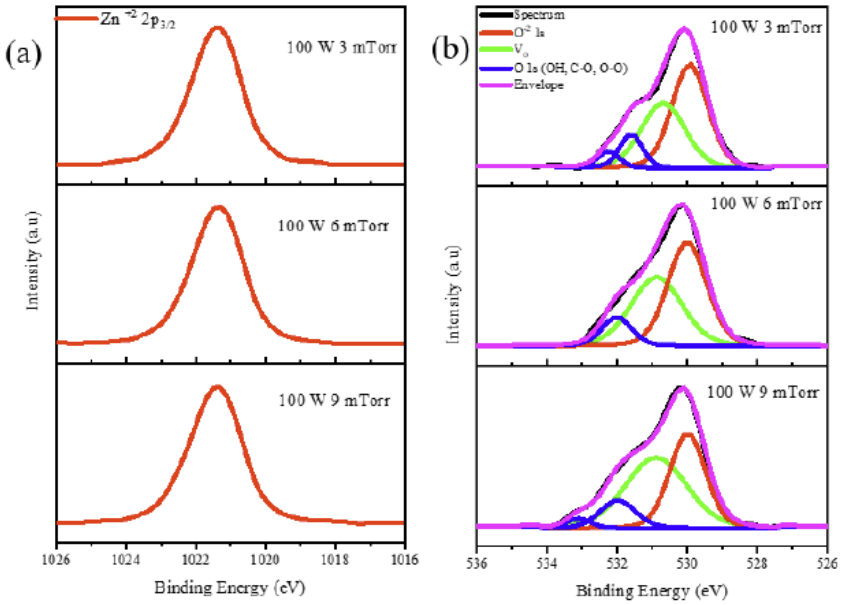

Figure 4.6: XPS for ZnO films grown at varied working pressure; (a) Zn $2p_{3/2}$, (b) O 1s.

Table 4.4: Composition of ZnO films as a function of working pressure.

Working pressure (mTorr)	Zn^{2+} 2p (%)	Stoichiometric O-Zn (%)	Non-stoichiometric oxygen (%)	O 1s (OH, C-O, O-O) oxygen (%)
9	61.0	14.8	18.9	5.4
6	61.0	18.8	16.2	4.0
3	58.8	20.0	15.2	6.0

4.6 Optical Characterization

As shown in Figure 4.7, photoluminescence (PL) measurements of the films show a good qualitative correlation between the intensity of the peak at ~464 nm (2.67 eV), which is related to oxygen vacancies [13,14] and the free carrier concentration. This is consistent with the XPS

findings previously discussed and summarized in Figures 4.5 and 4.6 as well as Tables 4.3 and 4.4. However, another peak at ~424 nm (2.92 eV) that is associated with Zn_i [15,16] is present in all samples. Thus, while oxygen vacancies are dominant, Zn interstitials (Zn_i) are also likely contributors to the observed n-type conduction. The absorption edge was observed to blue shift with conditions that increased the carrier concentration as can be discerned from the Tauc plots in Figure 4.8. The increase in the absorption energy is likely due to a Burstein-Moss shift with increasing carrier degeneracy as has been previously shown to occur in ZnO with degenerate levels of free carrier concentrations [2,17,18]. The samples exhibited an average of 85% transmissivity as Figure 4.9 shows.

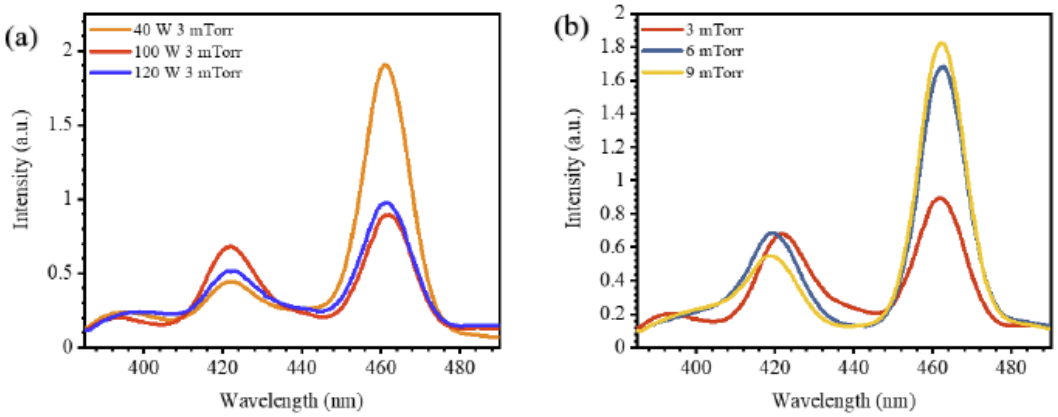

Figure 4.7: (a) PL spectra as a function of sputtering power, (b) PL spectra as a function of working pressure.

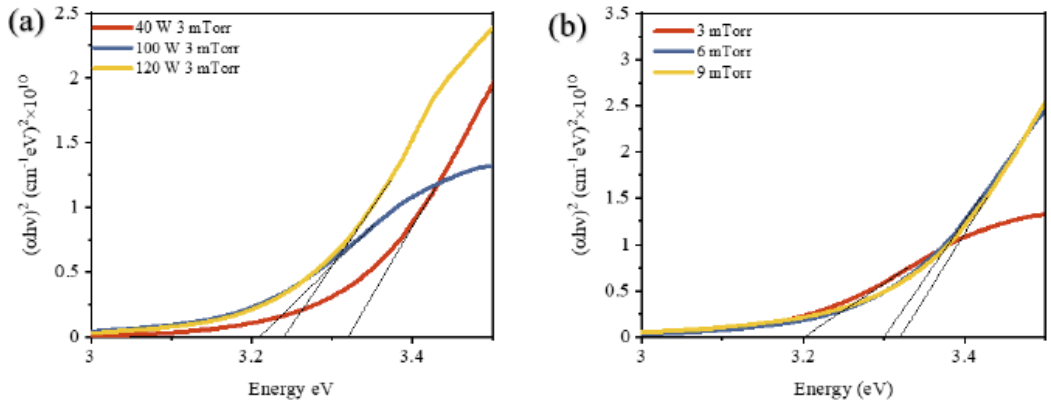

Figure 4.8: Tauc plots for the produced ZnO films as a function of (a) sputtering power, (b) working pressure.

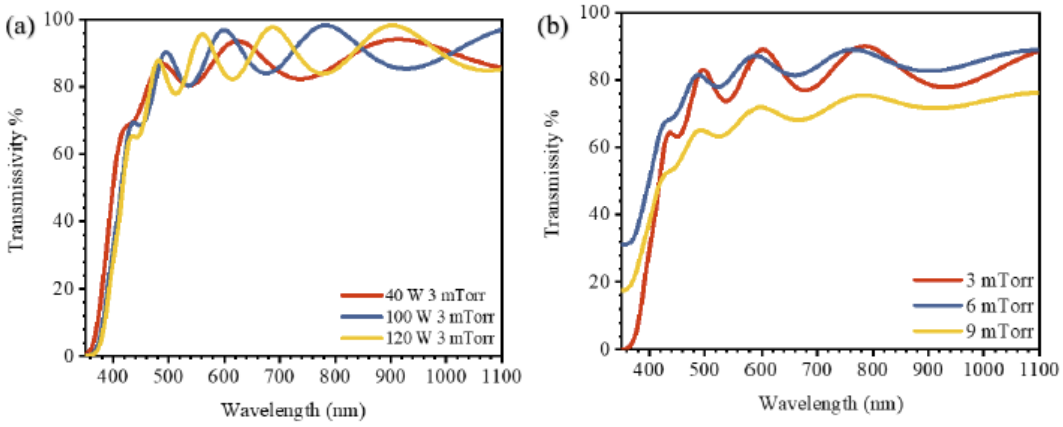

Figure 4.9: Transmittance spectra for the produced ZnO films (a) varied power, (b) varied pressure.

4.7 Conclusion

The results indicate that the usual behaviors of increasing oxygen desorption, non-stoichiometry, and conductivity observed with increasing deposition power under typical growth conditions [19,20] are not universally applicable. XPS analysis showed that in the range of low sputtering power with unheated substrates studied in this work, increasing the power density *increased* the fraction of oxygen that was stoichiometrically bonded. An accompanying decrease in the vacancy concentration and decrease in carrier concentration and conductivity was observed. Likewise, when the deposition pressure decreased, corresponding to fewer inelastic collisions in the plasma and more energetic species arriving at the unheated substrate, the fraction of stoichiometrically bonded oxygen increased, and a concomitant decrease in the carrier concentration was observed. These findings suggest that atomic peening and energy transfer from the plasma are necessary supplies of energy for bonding and film formation. The XRD indicates that without the benefit of active substrate heating to drive surface diffusion and mobility, the conditions of higher deposited atom flux and higher energy produce more stable nuclei which grow with multiple orientations, resulting in nanocrystalline films without (002)

texturing. Since the films that showed the highest fraction of stoichiometrically bonded oxygen also exhibited the lowest electron mobility, it is speculated that point defect scattering (vacancies) is not the dominant carrier scattering mechanism. More careful study of the temperature dependence of mobility is required to develop further insight. The results reflect that low energy RF magnetron sputtering without substrate heating can be used to directly grow conductive, optically transparent ZnO thin films on flexible substrates with potential for flexible device applications.

4.8 References

[1] J. Chennupati, P. Stephen J., Zinc oxide bulk, thin films and nanostructures: processing, properties, and applications, Elsevier, n.d.

[2] J. Jitendra Kumar, S.-O. Reinaldo, D. Jincheng, S. Nigel D., Semiconductor to metal transition in degenerate ZnO: Al films and the impact on its carrier scattering mechanisms and bandgap for OLED applications, J. Mater. Sci. Mater. Electron. 25 (n.d.) 1492–1498. https://doi.org/10.1007/s10854-014-1758-9.

[3] M. Rashmi, S. K., G. Vinay, Influence of stress on the structural and dielectric properties of rf magnetron sputtered zinc oxide thin film, J. Appl. Phys. 103 (n.d.) 094903. https://doi.org/10.1063/1.2903531.

[4] S. F. K., L. G. X., L. W. J., S. B. C., The role of oxygen vacancies in epitaxial-deposited ZnO thin films, J. Appl. Phys. 101 (n.d.) 053106. https://doi.org/10.1063/1.2437122.

[5] K. Kyoung-Kook, S. Jae-Hoon, J. Hyung-Jin, C. Won-Kook, P. Seong-Ju, S. Jong-Han, L. Jeong-Yong, Photoluminescence and heteroepitaxy of ZnO on sapphire substrate (0001) grown by rf magnetron sputtering, J. Vac. Sci. Technol. A Vacuum, Surfaces, Film. 18 (n.d.) 2864–2868. https://doi.org/10.1116/1.1318192.

[6] R. A.N., S. P.J., H. J.J., M. C., B. J.E., V. A.A., Microstructure of ZnO thin films deposited by high power impulse magnetron sputtering, Thin Solid Films. 579 (n.d.) 30–37. https://doi.org/10.1016/j.tsf.2015.02.048.

[7] Y. Shiliu, L. Jieni, S. Mandar M., L. Ming, W. Haiqian, Oxygen interstitial mediated effective doping of Al in ZnO: Al films prepared by magnetron sputtering, Mater. Lett. 179 (n.d.) 146–149.

[8] J. Anderson, W. Chris G. Van de, Fundamentals of zinc oxide as a semiconductor, Reports Prog. Phys. 72 (n.d.) 126501. https://doi.org/10.1088/0034-4885/72/12/126501.

[9] L. Xinyi, W. Yunlan, L. Weifeng, J. Guoshun, Z. Changfei, Study of oxygen vacancies′ influence on the lattice parameter in ZnO thin film, Mater. Lett. 85 (n.d.) 25–28. https://doi.org/10.1016/j.matlet.2012.06.107.

[10] P. Natalie O. V., H. Ian, R. Akshay, W. Mark W. B., D. Caterina, M. Rajaram Sakharam, B. James S., L. Rami R. M., G. Neil C., M. Hidetoshi, F. Richard H., S. Henry J., W. Mark E., Efficient ZnO Nanowire Solid-State Dye-Sensitized Solar Cells Using Organic Dyes and Core−shell Nanostructures, J. Phys. Chem. C. 113 (2009) 18515–18522. https://doi.org/10.1021/jp904919r.

[11] L. Sih-Sian, S. Yan-Kuin, Improvement of the performance in Cr-doped ZnO memory devices *via* control of oxygen defects, RSC Adv. 9 (n.d.) 2941–2947. https://doi.org/10.1039/C8RA10112D.

[12] F. Wenchun, W. Alan S., G. Eric, Interfacial bonding and morphological control of electropolymerized polythiophene films on ZnO, J. Phys. Chem. C. 117 (n.d.) 9852–9863.

[13] K. Saurabh, S. K., Residual stress and defect content in magnetron sputtered ZnO films grown on unheated glass substrates, Curr. Appl. Phys. 16 (n.d.) 748–756.

[14] X. Cai-Ling, Q. Dong-Huan, L. Hua, G. Yun, X. Tao, L. Hu-Lin, Low-temperature growth and optical properties of radial ZnO nanowires, Mater. Lett. 58 (n.d.) 3976–3979. https://doi.org/10.1016/j.matlet.2004.08.026.

[15] J. B. J., I. S., L. S. Yl, Violet and UV luminescence emitted from ZnO thin films grown on sapphire by pulsed laser deposition, Thin Solid Films. 366 (n.d.) 107–110.

[16] H. Deng-Lu, Z. Rui-Bin, W. Yan-Yan, Z. Cong-Mian, P. Cheng-Fu, T. Gui-De, Room temperature ferromagnetism in Ni-doped ZnO films, Curr. Appl. Phys. 10 (n.d.) 124–128.

[17] Y. N. Rajeswari, B. A. Chandra, Burstein–Moss shift and room temperature near-band-edge luminescence in lithium-doped zinc oxide, Appl. Phys. A. 103 (n.d.) 33–42.

[18] C. P. K., D. G. C., G. K. P., The simple analysis of the Burstein–Moss shift in degenerate n-type semiconductors, Phys. B Condens. Matter. 339 (n.d.) 198–203.

[19] L. Y.M., H. W.S., L. W.Y., Y. J.S., Effect of RF power on optical and electrical properties of ZnO thin film by magnetron sputtering, Mater. Chem. Phys. 72 (n.d.) 269–272. https://doi.org/10.1016/S0254-0584(01)00450-3.

[20] A. C. R., L. R. J., T. T. C., The effect of rf power on reactively sputtered zinc oxide, J. Appl. Phys. 51 (n.d.) 6405–6410. https://doi.org/10.1063/1.327585.

CHAPTER 5

LOW TEMPERATURE GROWTH OF *a*-BO_xN_y*

5.1 Objective

Optimize the RF magnetron sputtering growth conditions for low-temperature a-BOxNy and determine the correlations between chemistry, surface topography, dielectric breakdown strength, optical bandgap, and charge transport mechanisms.

5.2 Structure and Surface Topography

The growth rate of the *a*-BO_xN_y films was observed to decrease with increasing deposition pressure as is shown in Figure 5.1. As the sputtering pressure increases the mean free path of sputtered species decreases due to increased inelastic scattering between sputtered constituents of the target and the sputtering gas [1–3], and it is also possible that the sputter yield decreased. Both factors decrease the concentration of sputtered species that arrive at the substrate, and therefore the growth rate. XRD measurements using both θ-2θ and 2° glancing angle scans revealed that the deposited *a*-BO_xN_y films were amorphous.

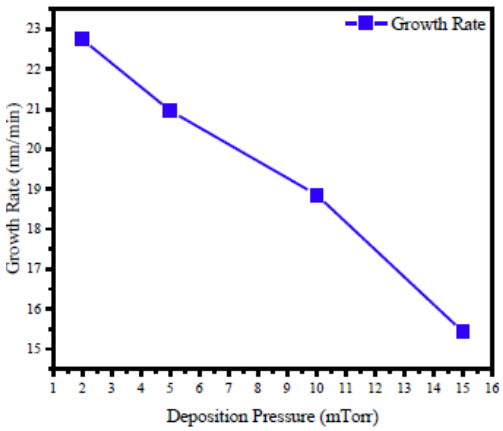

Figure 5.1: *a*-BO_xN_y growth rate dependence on deposition pressure.

* Significant amounts of this chapter are reproduced from Chukwudi E. Iheomamere, Corey L. Arnold, Jason Summers, Richard F. Reidy, Andrey A. Voevodin, Nigel D. Shepherd, Characterization of RF magnetron sputtered a-BOxNy/ZnO MIS structures for transparent electronics. Under peer-review with Journal of Materials Science: Materials in Electronics.

AFM surface topography images and the corresponding arithmetic averaged roughness (Ra) of the films grown at 2, 5, 10, and 15 mTorr are presented in Figure 5.2. The images reveal that as the pressure increased from 2 to 15 mTorr the roughness decreased from 3.4 nm to 0.2 nm, and a reduction in pinholes as seen in films grown at 2 and 5 mTorr with none observed at 10 and 15 mTorr within the AFM scan length. It is possible that at lower growth pressures when the flux of sputtered atoms is high, that without the benefit of much time for surface diffusion atoms "pile up" and cluster where they land on the unheated substrates, resulting in the observed surface characteristics. Another possibility is because of the longer mean free path of energetic ions and atoms impinging growing films at lower working pressures; highly energetic bombardment would cause damage to the growing film, therefore enhancing roughness. Studies have shown that the average energy deposited per atom affects microstructures [4]. Pinholes were observed in all of the films grown at 2 mTorr, which resulted in electrical shorts that precluded accurate determination of their breakdown strength.

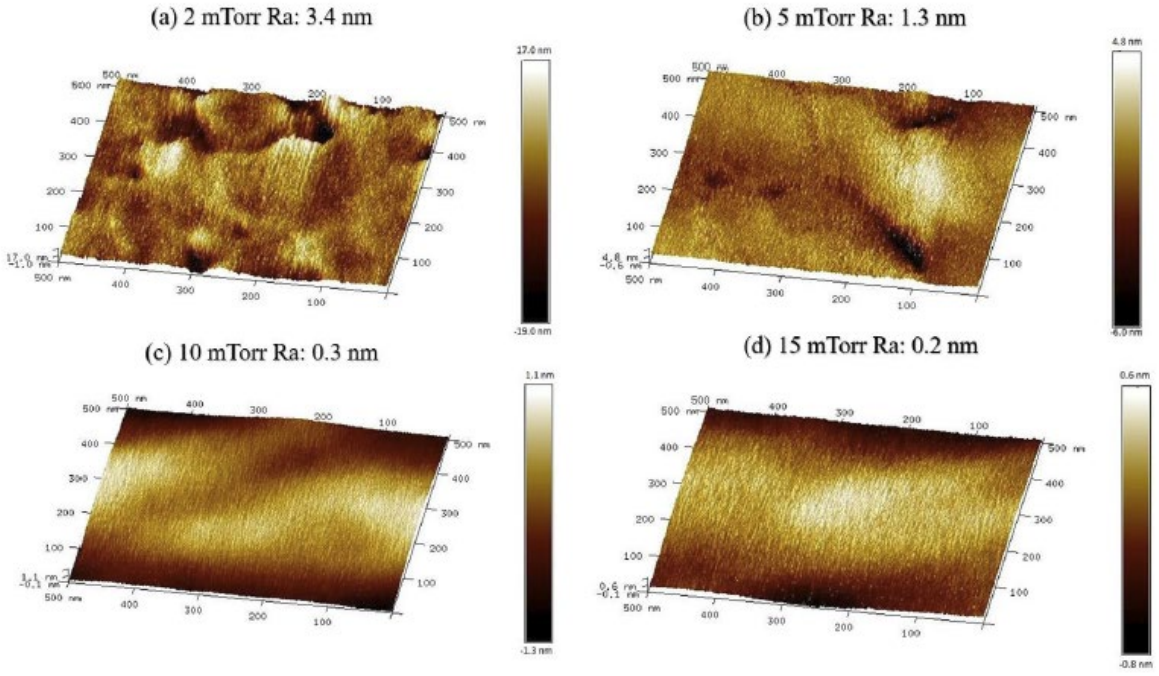

Figure 5.2: AFM images of the grown films show the obtained surface topography at various deposition pressures.

5.3 Chemical Analysis

The effect of processing conditions on the chemistry and stoichiometry of films grown at 2 – 15 mTorr were investigated using XPS, which revealed that the oxygen content increased with deposition pressure. The deconvoluted B1s peaks located at a binding energy of 189.8 eV and N1s peaks at 397.3 eV shown in Figure 5.3 are associated with sp^2 bonded B^{+3} and N^{-3} oxidation states in BN, respectively [5–9]. The B1s and N1s peaks at binding energies of 191.0 eV and 398.5 eV, respectively, are associated with boron-oxynitride (*a*-BO_xN_y) [10,11].

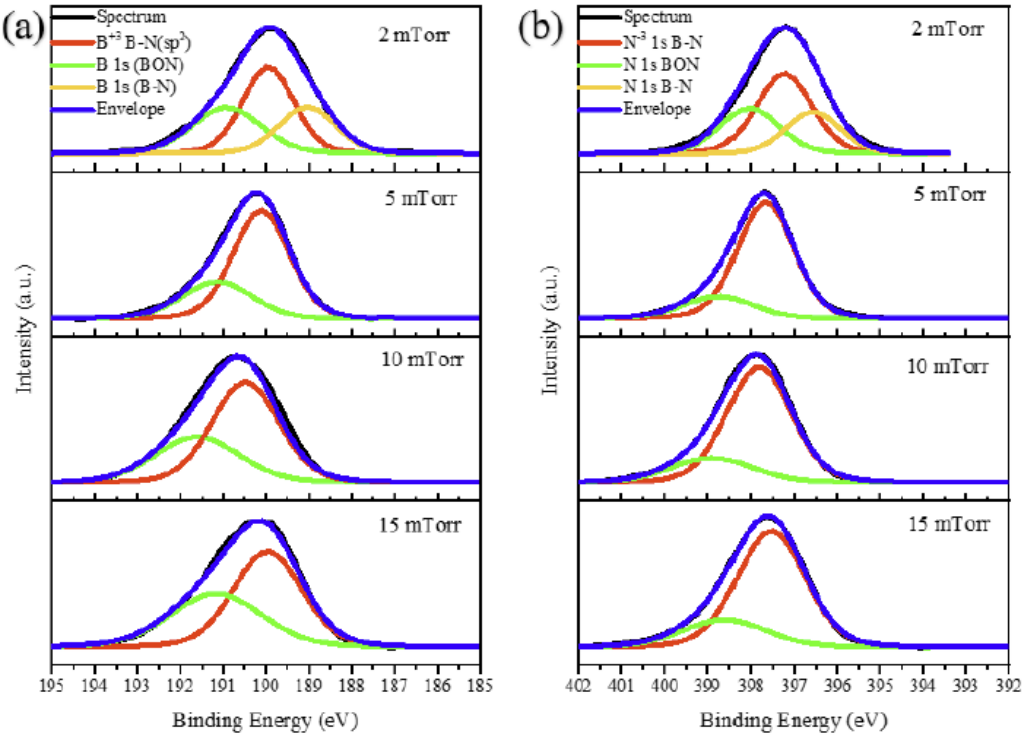

Figure 5.3: XPS spectra showing (a) B1s and (b) N1s as a function of pressure.

Also, for 2 mTorr process films, B1s and N1s peaks located at lower binding energies of 188.8 and 396 eV have been assigned to Nitrogen deficit BN species [12]. This indicates that oxygen is chemically bonded to boron in the films. The ratio of B 1s bonding in BN relative to that in BO_xN_y, together with the ratio of N 1s in BN to that in BO_xN_y are depicted as a function of the deposition pressure in Figure 5.4 and summarized inTable 5.1. Table 5.2 reports the atomic

percentage of B and N in the BN and BON films, respectively, as well as the percentage of oxygen which increased with the growth pressure. Increasing the pressure increases the amount of oxygen contaminant transported to the plasma vicinity.

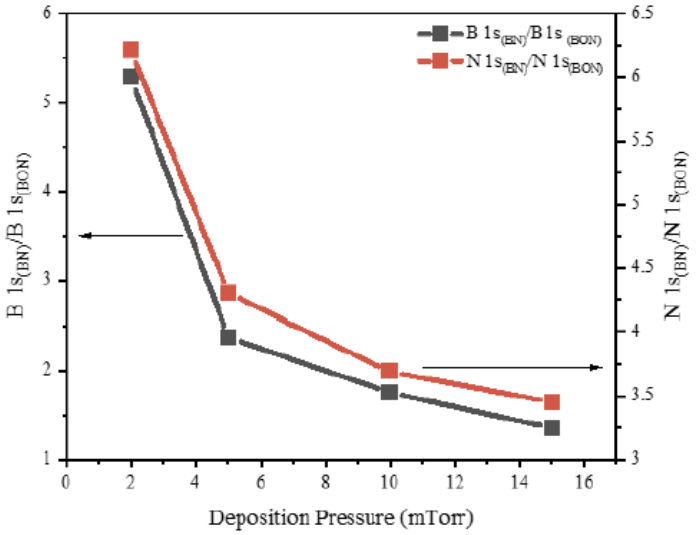

Figure 5.4: Elemental ratios of B1s and N1s in BN/BON as a function of deposition pressure.

Table 5.1: Atomic ratios of B1s and N1s in BN and BON as a function of deposition pressure.

Deposition Pressure (mTorr)	B 1s$_{(BN)}$/B1s$_{(BON)}$	N1s$_{(BN)}$/N1s$_{(BON)}$
2	5.28	6.21
5	2.37	4.30
10	1.75	3.69
15	1.35	3.45

Table 5.2: Percentage of B, N, O in BN and BON as a function of deposition pressure.

Deposition Pressure (mTorr)	B 1s (BN)		B 1s (BON)	N 1s (BN)		N 1s (BON)	O 1s
	Sp^2	N Deficit		Sp^2	N Deficit		
2	23	13	7	24	13	6	14
5	29	0	12	35	0	8	16
10	25	0	15	29	0	8	23
15	21	0	17	29	0	8	25

5.4 Electrical/Optical Characterization

As shown in Figure 5.5(a), J-E (I-V) measurements performed on films processed at 5 mTorr in MIM structures consisting of ITO/*a*-BO_xN_y/Ag stacks reveal quasi-ohmic characteristics, which we ascribe to through shorts associated with pinholes in films processed at these low working pressures.

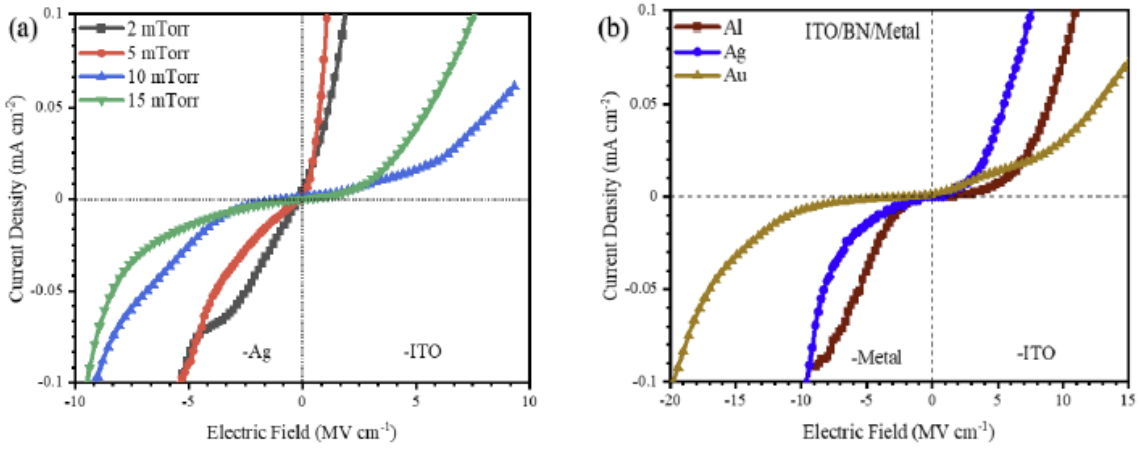

Figure 5.5: (a) Current density vs electric field for *a*-BO_xN_y as a function of deposition pressure showing breakdown behavior, (b) Current density vs electric field with electrode change.

This is likely compounded by local field enhancement due to higher surface roughness and asperities (Fig. 5.2 a and b). At higher processing pressures of 10 and 15 mTorr, pinholes are not observed and the surface roughness decreased significantly (Fig. 5.2 c and d). Maximum breakdown fields of 5 and 8 MV cm^{-1} were obtained for films grown at 10 and 15 mTorr respectively (Figure 5.5a). This compares to 7.3 MV/cm reported for a-BN [6]. To investigate the asymmetry in the J-E plot, electrode types were varied on one end of the MIM structure shown in Figure 5.5(b), field strength shows to be dependent on the metal contact type that was thermally evaporated. By injecting electrons from the metal contacts (Au, Ag, or Al) a difference in breakdown strength is observed. It is suspected that in addition to the deposition method, the

various workfunction or diffusivity of metal into the insulator are possible contributing factors in asymmetric breakdown curves.

Fits of the measured J-E data to the conduction mechanisms did not produce an unambiguous assignment of the transport process. For films grown 10 and 15 mTorr shown in Figures 5.6 and 5.7, show a combination of field enhanced Schottky emission and Frenkel-Poole mechanism [13,14] [15]. Better fittings suggest that field enhanced Schottky emission is the dominant conduction mechanism. A change in slope fittings is suspected to be influenced by the change in properties (eg. dielectric constants, temperature, or trap concentrations) as the electric field increases in the insulator. Multiple conduction mechanisms can contribute in the same field range as reported in the literature, [16]. The totality of this analysis indicates that transport is complex with several mechanisms contributing to the observed behavior.

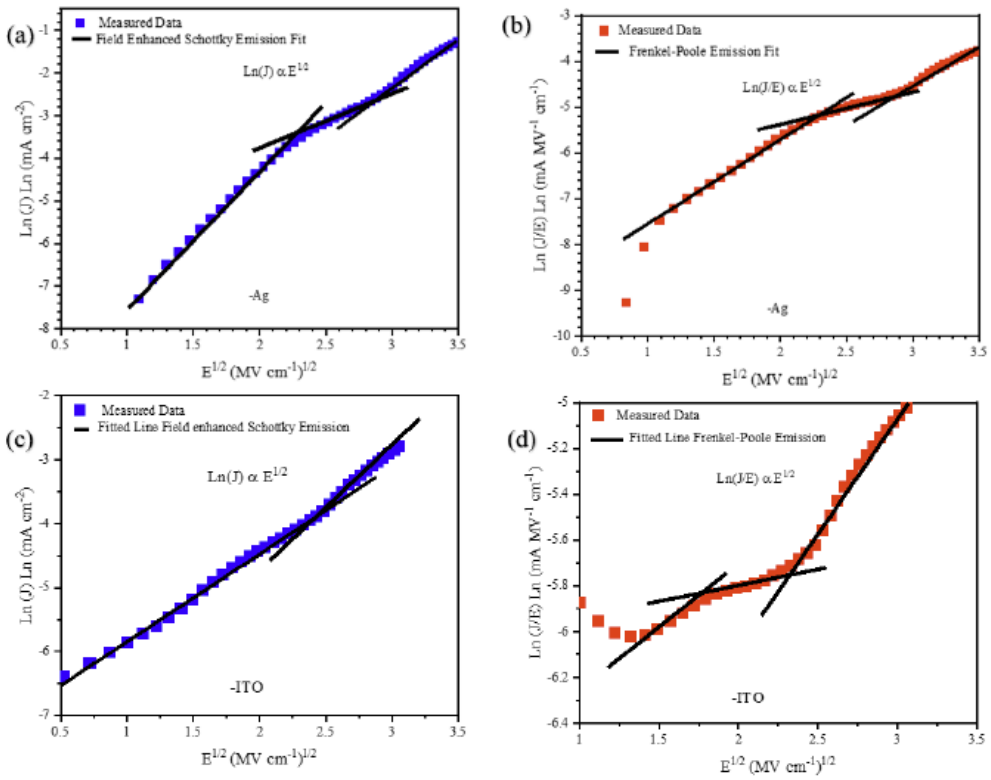

Figure 5.6: Data fits in the various field ranges for 10 mTorr suggesting (a,c) Field enhanced Schottky emission at low field, and (b,d) Frenkel-Poole emission in the intermediate range.

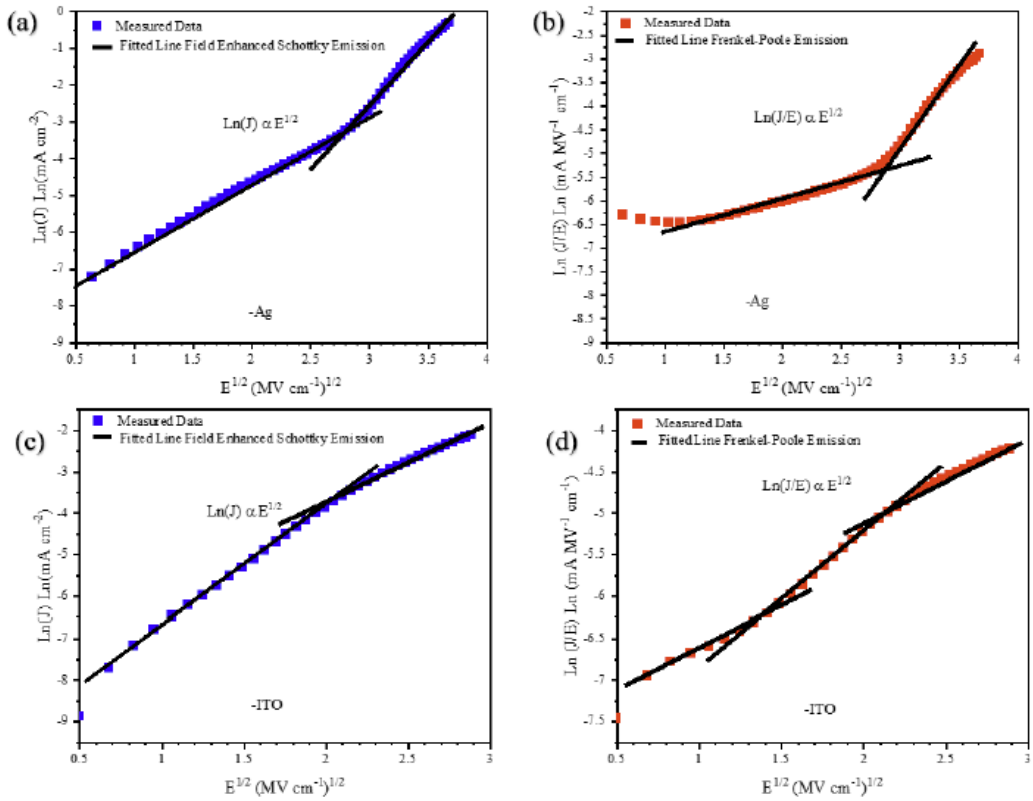

Figure 5.7: Data fits in the various field ranges for 15 mTorr suggesting (a,c) Field enhanced Schottky emission at low field, (b,d) Frenkel-Poole emission in the intermediate range.

It is noted that the breakdown curves are asymmetrical, with smaller breakdown fields being observed with electron injection from the ITO. The workfunction values for ITO are reported to be 4.4 to 4.8 eV [17,18] and 4.2 to 4.7 eV for Ag [19], which are in the same range and provide an approximately symmetric structure. We speculate that the observed difference is due to processing: the *a*-BO_xN_y is RF plasma sputter deposited onto the ITO which likely creates a distribution of defects and traps that facilitate enhanced thermionic field emission. In contrast, the Ag is thermally evaporated onto the *a*-BO_xN_y, a process that is much less energetic and likely to result in fewer generated defects and traps at the *a*-BO_xN_y/Ag interface. The effect of sputtering has previously been predicted to generate a rougher electrode/dielectric interface or regions of thin dielectric materials [20,21]. The 10 and 15 mTorr processed *a*-BO_xN_y exhibited static dielectric constant values ranging from 3.26 to 3.58.

The Tauc plot: $(\propto h\nu)^{\frac{1}{n}} = B(h\nu - E_g)$ shows the relation between photon energy and absorption where the bandgap of the material can be extrapolated [22,23], where α is the absorption coefficient, h is plank's constant, v is the photon frequency, E_g is the bandgap, B is a constant and n is ½ or 2 for direct and indirect transitions respectively. Tauc plot in Figure 5.8 (a) and (b) reveals an indirect bandgap of 3.9 and 3.3 eV for a-BO_xN_y films that were grown on quartz at 15 and 10 mTorr respectively. Indicating transparency over the full visible range. To verify the bandgap, ellipsometry was performed on films grown at 15 mTorr a-BO_xN_y grown on Si. As shown in Figure 5.9(a), excellent fits to the measured data were obtained using a Tauc-Lorentz model. The model is Kramer-Kronig consistent and the quality of the model was calculated using the equation:

$$MSE = \sqrt{\frac{1}{3n-m}\sum_{i=1}^{n}[(N_{Ei} - N_{Gi})^2 + (C_{Ei} - C_{Gi})^2 + (S_{Ei} - S_{Gi})^2]} \times 1000.$$

where: *MSE* = Mean Square Error; n = number of wavelengths, m = number of fit parameter, N = Cos(2Ψ), C = Sin(2Ψ)Cos(Δ), S = Sin(2Ψ)Sin(Δ), parameters with subscript E and G represent measured and model data respectively [24]. An *MSE* value of 7 was calculated for the Tauc-Lorentz model. The Tauc plot from the absorption coefficients obtained from the imaginary part of the refractive index also reveals a bandgap of 3.9 eV as depicted in Figure 5.9(c).

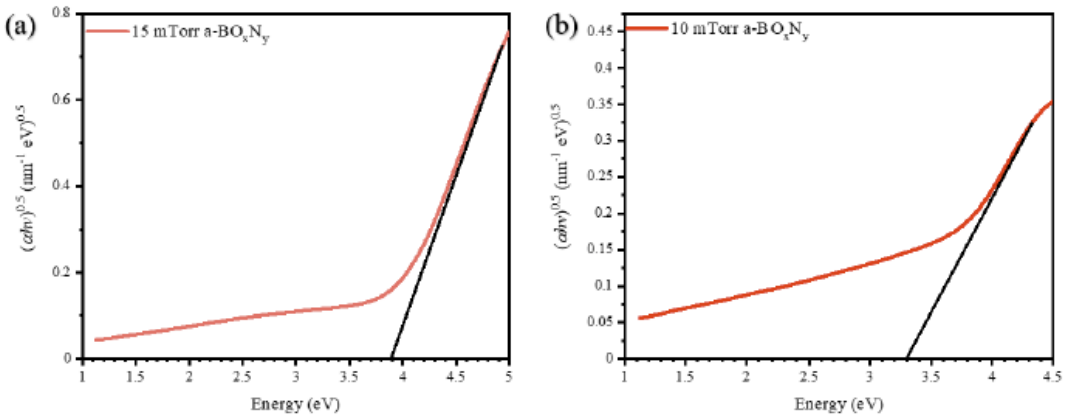

Figure 5.8: Tauc plot a-BO_xN_y: (a) 15 mTorr, (b): 10 mTorr.

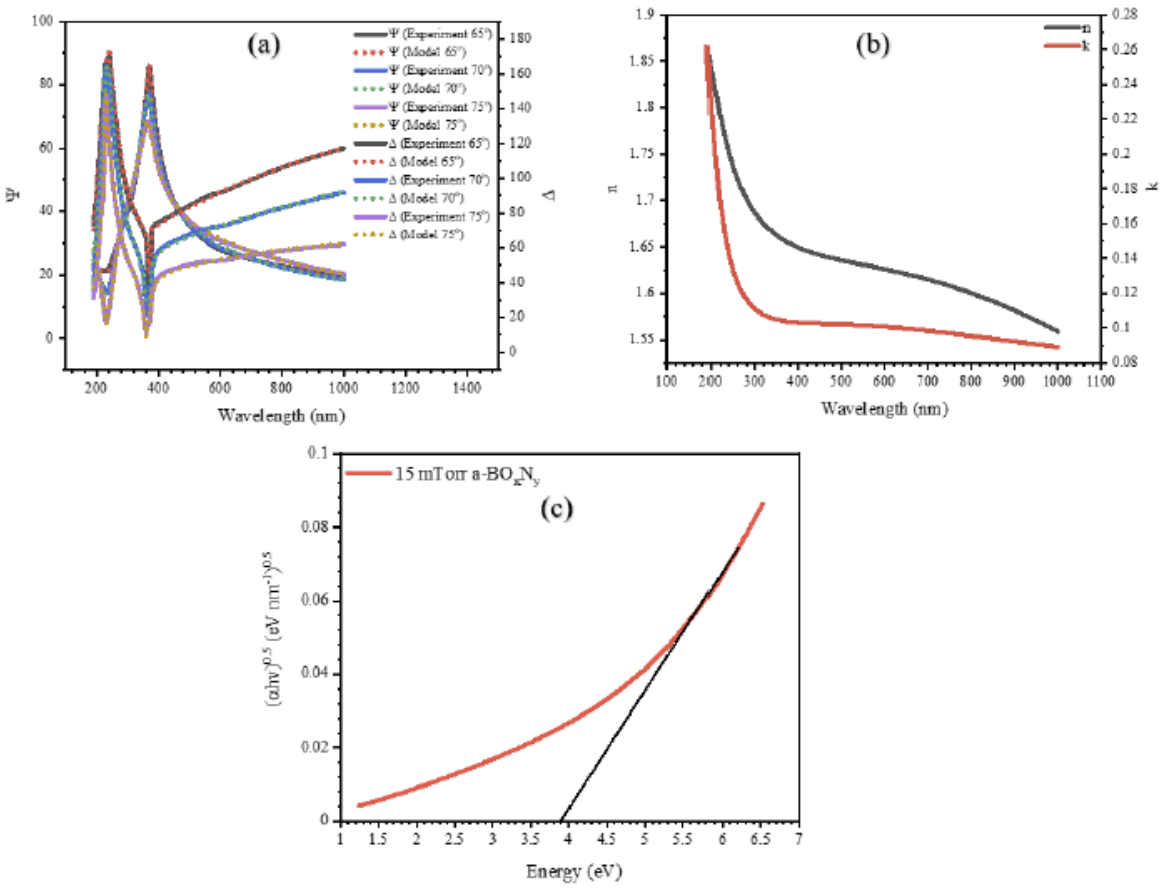

Figure 5.9: (a) Spectroscopic ellipsometry data and Tauc-Lorentz model fit, (b) optical constants (c) Tauc plot using the absorption coefficients determined from *k*.

5.5 Conclusion

Amorphous BO_xN_y films with breakdown strength in the same range as that of *a*-BN were obtained by RF magnetron sputtering without substrate heating. The films were pinhole-free and exhibited good surface topography at the higher deposition pressures used. The charge transport mechanism was observed to be complex and field-dependent, with indicators of field-enhanced Schottky emission and Frenkel–Poole emission being present. Spectroscopic ellipsometry using a Tauc-Lorentz model confirmed a 3.9 eV bandgap determined from optical absorption measurements of 15 mTorr grown films. The results show the potential of low-temperature RF magnetron sputtering and *a*-BO_xN_y for use in transparent electronics.

5.6 References

[1] S. Peter, Theory of sputtering. I. Sputtering yield of amorphous and polycrystalline targets, Phys. Rev. 184 (n.d.) 383.

[2] M. D. M., S. A. A., Effect of scattering of sputtered atoms on the growth rate of films fabricated by magnetron sputtering, Tech. Phys. Lett. 43 (n.d.) 814–816.

[3] H. J. C., W. C. E., Pressure effects in planar magnetron sputter deposition, J. Vac. Sci. Technol. A. 4 (n.d.) 408–412. https://doi.org/10.1116/1.573892.

[4] P. I., A. F., G. J. E., H. L., S. J.-E., Average energy deposited per atom: A universal parameter for describing ion-assisted film growth?, Appl. Phys. Lett. 63 (n.d.) 36–38. https://doi.org/10.1063/1.109742.

[5] G. Nicholas R., M. Christopher, J. Michael L., H. Jianjun, H. Phillip T., H. Al M., B. Austin T., G. Christopher A., D. Michael F., M. Michael E., H. Drew M., F. Timothy S., V. Andrey A., Amorphous Boron Nitride: A Universal, Ultrathin Dielectric For 2D Nanoelectronics, Adv. Funct. Mater. 26 (n.d.) 2640–2647. https://doi.org/https://doi.org/10.1002/adfm.201505455.

[6] H. Seokmo, L. Chang-Seok, L. Min-Hyun, L. Yeongdong, M. Kyung Yeol, K. Gwangwoo, Y. Seong In, I. Kyuwook, K. Ki-Jeong, S. Tae Joo, Ultralow-dielectric-constant amorphous boron nitride, Nature. 582 (n.d.) 511–514.

[7] G. Nicholas R., W. Adam R., M. Christopher, B. John E., H. Jianjun, G. Jamie J., V. Andrey A., F. Timothy S., Thermal conductance at nanoscale amorphous boron nitride/metal interfaces, Surf. Coatings Technol. 397 (n.d.) 126017. https://doi.org/10.1016/j.surfcoat.2020.126017.

[8] J. A-Rang, H. Seokmo, H. Chohee, Y. Seong In, K. Gwangwoo, J. Hu Young, S. Tae Joo, P. Sung O., W. Kester, K. Sang Kyu, P. Noejung, Y. Kwangnam, C. Eunjip, M. Artem, W. Freddie, N. Kostya S., L. Hyunseob, S. Hyeon Suk, Wafer-Scale and Wrinkle-Free Epitaxial Growth of Single-Orientated Multilayer Hexagonal Boron Nitride on Sapphire, Nano Lett. 16 (2016) 3360–3366. https://doi.org/10.1021/acs.nanolett.6b01051.

[9] K. Gwangwoo, J. A-Rang, J. Hu Young, L. Zonghoon, K. Dae Joon, S. Hyeon Suk, Growth of High-Crystalline, Single-Layer Hexagonal Boron Nitride on Recyclable Platinum Foil, Nano Lett. 13 (2013) 1834–1839. https://doi.org/10.1021/nl400559s.

[10] S. Seung-Wan, L. Ki-Chang, P. Ho-Young, High-performance flexible all-solid-state microbatteries based on solid electrolyte of lithium boron oxynitride, J. Power Sources. 328 (n.d.) 311–317. https://doi.org/10.1016/j.jpowsour.2016.07.114.

[11] R. Junkai, M. Luca, E. Stefano, C. Carlo Maria, C. Laura, G. Gaetano, I. Plinio, Boron oxynitride two-colour fluorescent dots and their incorporation in a hybrid organic-inorganic film, J. Colloid Interface Sci. 560 (n.d.) 398–406. https://doi.org/10.1016/j.jcis.2019.10.020.

[12] C. Guimon, D. Gonbeau, G. Pfister-Guillouzo, O. Dugne, A. Guette, R. Naslain, M. Lahaye, XPS study of BN thin films deposited by CVD on SiC plane substrates, Surf. Interface Anal. 16 (1990) 440–445. https://doi.org/10.1002/sia.740160191.

[13] V. V. V., G. V. A., E. V. M., L. V. E., E. F. L., Structure and electrophysical properties of boron nitride thin films, Phys. Status Solidi. 34 (1976) 85–94. https://doi.org/10.1002/pssa.2210340106.

[14] R. Myron J., R. James F., Preparation and Properties of Thin Film Boron Nitride, J. Electrochem. Soc. 115 (n.d.) 423. https://doi.org/10.1149/1.2411238.

[15] S. W., H. H.L., Amorphous BN films produced in a double-plasma reactor for semiconductor applications, Solid. State. Electron. 26 (n.d.) 931–939. https://doi.org/10.1016/0038-1101(83)90069-2.

[16] C. Yu-Ting, C. Ting-Chang, Y. Po-Chun, H. Jheng-Jie, T. Hsueh-Chih, H. Hui-Chun, Y. Jyun-Bao, C. Ann-Kuo, G. Der-Shin, T. Ming-Jinn, Improvement of Resistive Switching Characteristics by Thermally Assisted Forming Process for $$\backslash$hbox ${$SiO$}$ _ ${$2$}$ $-Based Structure, IEEE Electron Device Lett. 34 (n.d.) 226–228.

[17] P. Yongsup, C. V., G. Yongli, H. Bing R., T. Ching Wan, Work function of indium tin oxide transparent conductor measured by photoelectron spectroscopy, Appl. Phys. Lett. 68 (n.d.) 2699–2701.

[18] S. Kiyoshi, I. Hisao, O. Yukio, S. Kazuhiko, Dependence of indium–tin–oxide work function on surface cleaning method as studied by ultraviolet and x-ray photoemission spectroscopies, J. Appl. Phys. 87 (n.d.) 295–298.

[19] D. A. W., M. C. H. B., Work function measurements on (100) and (110) surfaces of silver, Phys. Status Solidi. 27 (n.d.) 223–230.

[20] C. E. William, A. Nasir, K. Christopher C., C. John F., K. Douglas A., G. Brady J., W. John F., Advancing MIM Electronics: Amorphous Metal Electrodes, Adv. Mater. 23 (n.d.) 74–78. https://doi.org/10.1002/adma.201002678.

[21] K. Subramanian, S. Elias, B. Shekhar, Effects of dielectric thickness and contact area on current–voltage characteristics of thin film metal–insulator–metal diodes, Thin Solid Films. 516 (n.d.) 2244–2250.

[22] T. J., G. Radu, V. Anina, Optical properties and electronic structure of amorphous germanium, Phys. Status Solidi. 15 (n.d.) 627–637.

[23] T. J., Optical properties and electronic structure of amorphous Ge and Si, Mater. Res. Bull. 3 (n.d.) 37–46. https://doi.org/10.1016/0025-5408(68)90023-8.

[24] T. Harland, I. Eugene A., Handbook of ellipsometry, William Andrew, n.d.

CHAPTER 6

LOW TEMPERATURE GROWTH OF 2H – WS_2

6.1 Objective

Optimize the pulsed laser deposition growth conditions for low-temperature, few-layer WS_2 and determine the correlations between chemistry, surface topography, crystallinity, and electrical properties.

6.2 XRD Analysis

XRD results of films grown on quartz substrate at 10^{-6} Torr and varied substrate temperature shown in Figure 6.1(a) show a drive to (002) as the more textured plane with temperature increase. Figure 6.1(b) shows films grown at a substrate temperature of 400° with varied argon chamber pressure, XRD patterns suggest all grown films are 2H-WS_2 and all patterns are identical regardless of target chemistry.

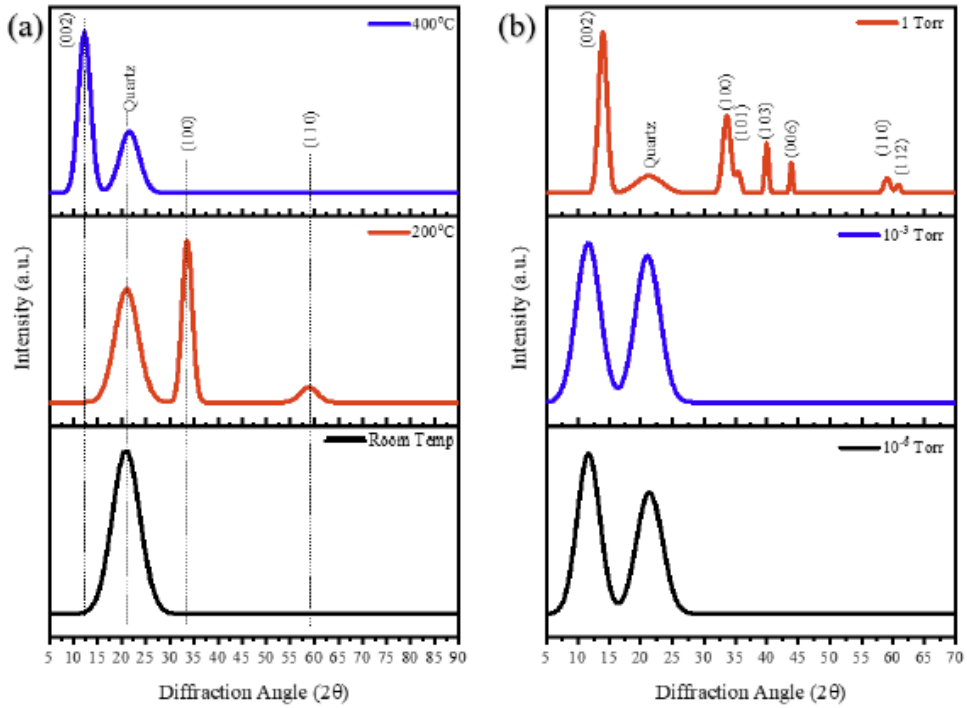

Figure 6.1: XRD pattern of 2H-WS_2 (a) varied substrate temperature, (b) varied argon chamber pressure.

It is observed that as chamber pressure increased during growth, the (002) shifted to a higher diffraction angle, a (002) shift from 12° for 10^{-6} Torr sample to 14.1° for 1 Torr sample is observed which suggest relaxation on films due to internal stresses [1]. In addition to the diffraction angle shift observed, a reduction in FWHM of the (002) plane is observed as pressure increased, from 4.8° in 10^{-6} Torr grown films to 2.1° in 1 Torr grown films. This finding suggests pressure-induced crystallinity in WS_2 films [2].

6.3 Raman Analysis

Raman activities shown in Figure 6.2 corroborate the XRD finding of 2H-WS_2. The PLD deposited 2H-WS_2 shows Raman active lattice vibrations: out-of-plane A_{1g} at 419 cm^{-1}, and in-plane E^1_{2g} at 360 cm^{-1}. Second-order resonance was also observed at 352 cm^{-1} and 239 cm^{-1} are assigned 2LA(M) and A_{1g}(M)-LA respectively [3,4]. Higher-order resonance at 324 cm^{-1} and 302 cm^{-1} are assigned 2LA-E^2_{2g} and 2LA-$2E^2_{2g}$ respectively [3,5]. A separation of 62 cm^{-1} between 2LA and A_{1g} is similar to reported in PLD grown 2H-WS_2 which suggests few layers [6,7].

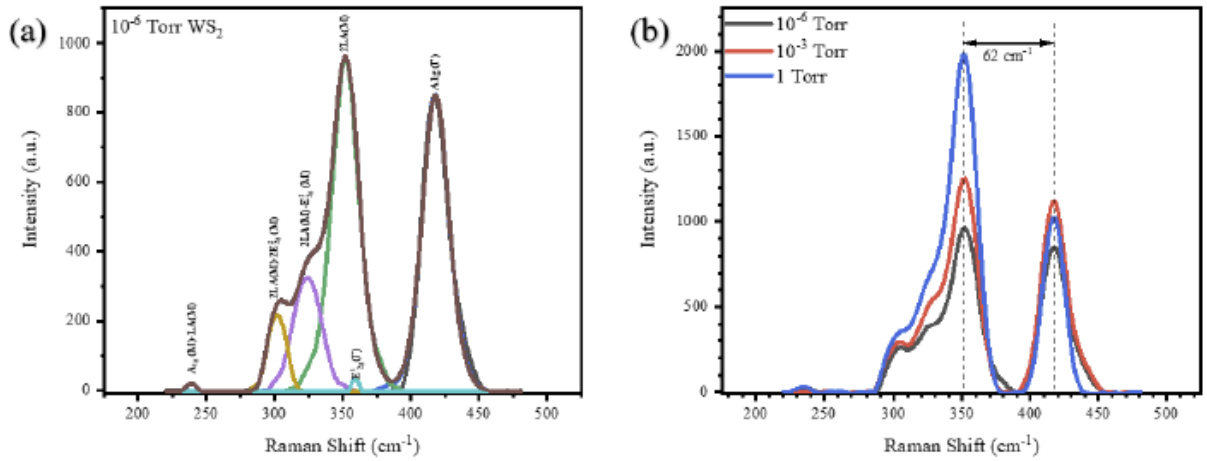

Figure 6.2: Raman vibration of 2H-WS_2 (a) Deconvoluted Raman spectrum, (b) Raman spectrum at varied growth pressure.

6.4 XPS Analysis/Electrical Dependence

Chemical analysis using X-ray photoelectron spectroscopy XPS technique shows core element scan for W 4f and S 2p spectrum for varied deposition pressure as shown in Figure 6.3.

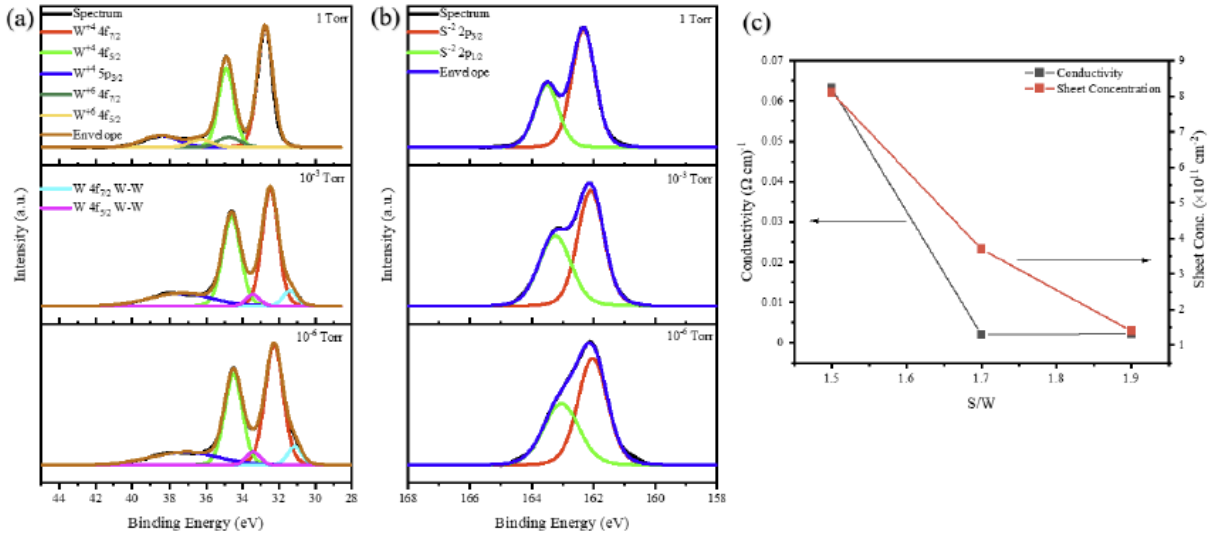

Figure 6.3: (a), (b) XPS spectra of varied argon chamber pressure from S/W 2:1 Target, (c) S/W atomic ratio as a function of electrical properties.

The depositions were carried out from the commercially bought S/W 2:1 WS_2 target. The W spectrum comprises a doublet with a 2.2 eV separation between W $4f_{7/2}$ and W $4f_{5/2}$ [8]. For all films, W peak assigned as W^{+4} $4f_{7/2}$ with the corresponding binding energy of 32.2 eV [9,10] is assigned to W-S bond in WS_2. For films grown at 10^{-6} and 10^{-3} Torr show W peak located at a lower binding energy of 31.2 eV, this peak is assigned to W-W bond [7]. It is also observed that the W-W peak vanishes for films grown at 1 Torr which suggests an improved S/W ratio as pressure increased. At 1 Torr a new W peak assigned W^{+6} $4f_{7/2}$ at a binding energy of 35.0 eV. This peak has been assigned to W in WO_3. The presence of O atoms at the higher chamber pressure grown WS_2 films suggests argon gas flow promotes the transportation of O-atoms during the growth process. These O-atoms could be sourced from impurities in gas, OH groups, and H_2O molecules trapped on the walls of the chamber. The sulfur spectrum comprises a

doublet with a 1.2 eV separation between S $2p_{3/2}$ and S $2p_{1/2}$. For all films, peaks assigned to S^{-2} $2p_{3/2}$ at a binding energy of 162 eV have been assigned to S-W bond in WS_2 [11,12]. The S/W ratio increased from 1.5 in 10^{-6} Torr films to 1.9 in 1 Torr grown films and an observed decrease in sheet carrier concentration and conductivity values of films as pressure increases shown in fig.3(c) plot. Hall measurements of films show *n*-type carriers with atomic S/W ratios of 1.9 and less, while films of S/W ratios above 2.0 are *p*-type. This is consistent with previous reports[13].

6.5 Surface Topography by AFM

Surface topology using AFM as shown in Figure 6.4 suggests films are nanoparticles, but as argon pressure was set to 1 Torr larger particles sizes were observed; which may also relate to literature reports on fullerene-like particle formation[14]. It is speculated that high processing pressure promotes the coalescence of nanoparticles to form larger observed surface particles. Also, large-scale synthesis of 3D fullerene has been successfully achieved at atmospheric pressure using CVD technique [15].

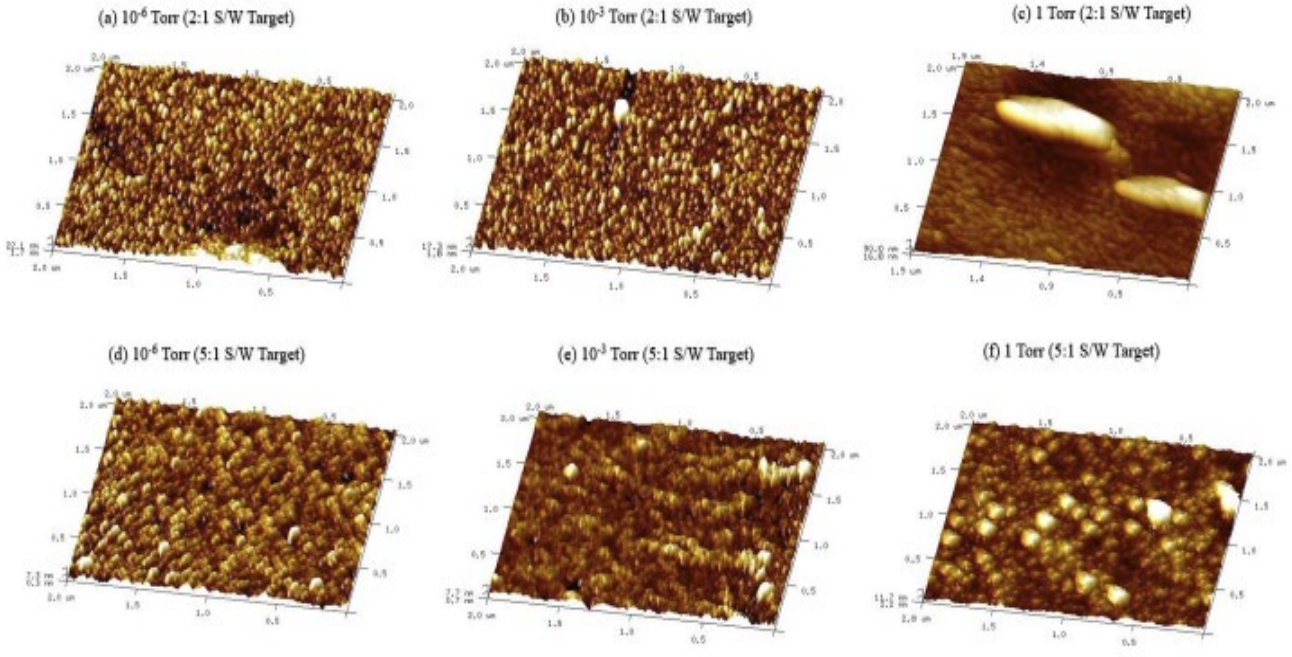

Figure 6.4: AFM Images of WS_2 films at varied pressure.

6.6 Analysis of 2H-WS_2 Grown of *a*-BO_xN_y

XPS and XRD characterization was conducted to investigate the chemical and structural stability of a WS_2 film grown on 34 nm *a*-BO_xN_y as shown in Figure 6.5.

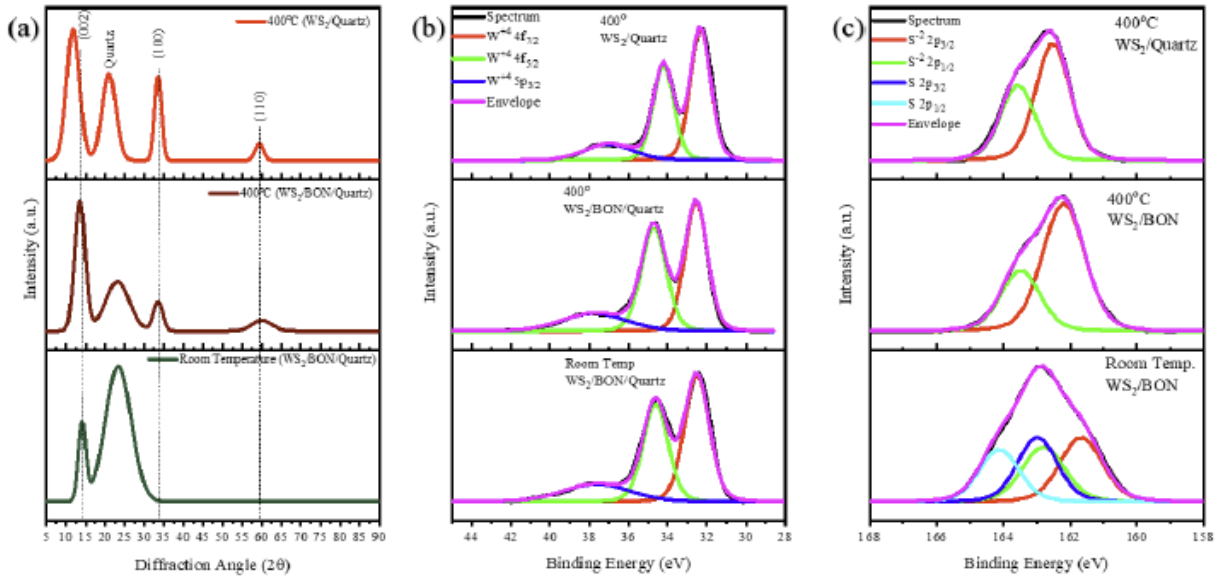

Figure 6.5: XRD, XPS of WS_2 on *a*-BO_xN_y: (a) XRD, (b) XPS W 4f spectrum, (c) XPS S 2p spectrum.

XPS and XRD data were compared to films deposited at 10^{-3} Torr, 400ºC WS_2 on quartz using the sulfur-rich target as mentioned earlier. For films grown at 400ºC on both quartz and *a*-BO_xN_y, XPS spectra did not show a variation in binding energy suggesting no change in oxidation states as in fig. 5 (b) and (c). Nevertheless, a slight increase in the S/W ratio of 2.5 is observed in 400ºC grown film on *a*-BO_xN_y as compared to quartz 2.1. A S/W ratio of 5.2 is obtained for films grown at room temperature on *a*-BO_xN_y. For WS_2 films deposited at room temperature, an extra XPS S 2p doublet assigned S $2p_{3/2}$ at a binding energy of 163 eV, the peak is assigned to S-S bonding because of the S-rich target used in growth. Also, unlike WS_2 deposited at room temperature on quartz which is amorphous, WS_2 films of *a*-BO_xN_y show the emerging (002) plane. XRD data reveal a shift from 12º to 13.7º diffraction angle for films grown on *a*-BO_xN_y. This suggests a more relaxed film from internal stresses. A reduction in

FWHM from 3.9° to 3° is observed for films grown on quartz and *a*-BO_xN_y respectively as shown in Figure 6.5(a). These findings suggest improved chemistry and structure are attainable for 2H-WS_2 deposited on *a*-BO_xN_y.

6.7 Conclusion

PLD processing of WS_2 shows temperature-dependent crystalline orientation. Films are hexagonal and the (002) peaks became more pronounced as substrate temperature increased to 400°C. Chemical analysis shows that the S/W ratio increases with increased growth pressure. High argon chamber pressure is expected to mitigate S desorption from growing films into the vacuum. Electrical measurements show that carrier concentration and conductivity decrease with increasing growth pressure. Thermodynamic equilibrium conditions suggest that as S desorbs from the film, the S vacancy increases. Each sulfur vacancy is speculated to contribute 2 electrons to the conduction band; therefore, for every vacancy that is occupied by an S atom it is speculated that carrier concentration will reduce by 2 electrons: $WS_2 - \frac{x}{2}S_{2(gas)} = WS_{(2-x)} + xV^{\cdot\cdot} + 2xe^{-}$. XRD shows the relaxation of films from internal stresses with increased pressure on both films grown on quartz and *a*-BO_xN_y substrate. This could be attributed to the slower growth process resulting from increased inelastic collisions at higher chamber pressure, allowing atoms time to occupy lattice positions with less residual stress. 2H-WS_2 deposited on *a*-BO_xN_y shows an improved S/W ratio and structure when compared to samples grown on quartz which is likely associated with a better film adhesion between WS_2 on *a*-BO_xN_y.

6.8 References

[1] U. T, Microstructural parameters from X-ray diffraction peak broadening, Scr. Mater. 51 (n.d.) 777–781. https://doi.org/10.1016/j.scriptamat.2004.05.007.

[2] K. Yusuf, G. Emre, Growth Control of WS2: From 2D Layer by Layer to 3D Vertical Standing Nanowalls, ACS Appl. Mater. Interfaces. 12 (n.d.) 15785–15792.

[3] S. C., C. F., F. M., A. M., Second-order Raman effects, inelastic neutron scattering and lattice dynamics in 2H-WS2, Chem. Phys. 150 (n.d.) 281–293.

[4] M. A. A., P. P., D. G., A. S., K. L., M. D. K., Second-order resonant Raman scattering in single-layer tungsten disulfide WS 2, Phys. Rev. B. 89 (n.d.) 245442.

[5] W. Longfei, van H. Arno J. F., D. Nelson Y., G. Lu, R. Marie-Ingrid, F. Heiner, D.L. Nora H., H. Emiel J. M., H. Jan P., Enhancing the electrocatalytic activity of 2H-WS $_2$ for hydrogen evolution *via* defect engineering, Phys. Chem. Chem. Phys. 21 (n.d.) 6071–6079. https://doi.org/10.1039/C9CP00722A.

[6] T. Kun, B. Karthikeyan, T. Ashutosh, Growth of two-dimensional WS2 thin films by pulsed laser deposition technique, Thin Solid Films. 668 (n.d.) 69–73. https://doi.org/10.1016/j.tsf.2018.10.015.

[7] R. Urmilaben P., C. Bimin, I. Chukwudi, N. Gilbert, V. Andrey A., S. Nigel D., Growth of pulsed laser deposited few-layer WS2 films, J. Vac. Sci. Technol. A Vacuum, Surfaces, Film. 37 (n.d.) 051505.

[8] C. Jill, K.J. Roger C., Handbook of X-ray photoelectron spectroscopy, Perkin-Elmer Corp. 40 (n.d.) 221.

[9] O. J, B. J. C, K. A, P. J, Photoconductive WS2 thin films obtained from a multilayer Ni/W/S…W/S structure, Appl. Surf. Sci. 120 (n.d.) 1–8. https://doi.org/10.1016/S0169-4332(97)00253-5.

[10] M. David J., Core-level spectra of powdered tungsten disulfide, WS $_2$, Surf. Sci. Spectra. 25 (n.d.) 014002. https://doi.org/10.1116/1.5030093.

[11] L. Xiaogan, L. Xiaoxin, L. Zhi, W. Jing, Z. Jianwei, WS2 nanoflakes based selective ammonia sensors at room temperature, Sensors Actuators B Chem. 240 (n.d.) 273–277. https://doi.org/10.1016/j.snb.2016.08.163.

[12] W. K. C., L. X., C. J., E. D. T., W. P. C., M. K. A. R., Surface and friction characterization of MoS2 and WS2 third body thin films under simulated wheel/rail rolling–sliding contact, Wear. 264 (n.d.) 526–534. https://doi.org/10.1016/j.wear.2007.04.004.

[13] R. Urmilaben P., J. Jitendra Kumar, V. Andrey A., S. Nigel D., A photoelectron study of annealing induced changes to workfunction and majority carrier type in pulsed laser deposited few layer WS 2 films, J. Mater. Sci. Mater. Electron. 29 (n.d.) 20051–20056.

[14] R. L., L. V., L. I., V. Yu., N. O., L. M., P.-B. R., F. Y., T. R., Tribological properties of WS2 nanoparticles under mixed lubrication, Wear. 255 (n.d.) 785–793. https://doi.org/10.1016/S0043-1648(03)00044-9.

[15] L. Xiao-Lin, G. Jian-Ping, L. Ya-Dong, Atmospheric pressure chemical vapor deposition: an alternative route to large-scale MoS2 and WS2 inorganic fullerene-like nanostructures and nanoflowers, Chem. Eur. J. 10 (n.d.) 6163–6171.

CHAPTER 7

INTERFACIAL ANALYSIS OF ITO/*a*-BO_xN_y/ZnO/Ag AND ITO/*a*-BN/WS_2/Ag MIS STRUCTURE

7.1 Objective

Growth of ITO/*a*-BO_xN_y/ZnO/Ag and ITO/*a*-BN/WS_2/Ag MIS Structure by PVD technique, measure and calculate the current density (J) – voltage (V), Capacitance (C) - Voltage (V), Conductance (G) – Voltage (V), Interface trapped charge concentration (N_{it}) and interface state density (N_{ss}).

7.2 ITO/*a*-BO_xN_y/ZnO/Ag MIS Structure

To verify if 15 mTorr grown *a*-BO_xN_y films is of comparable quality as a dielectric insulator in MISCAP and associated FET devices; the design of a simple MIS structure with our already established ZnO as the semiconductor was done to investigate accumulation, depletion, and inversion regions as expected in a simple MISCAP. MIS structure of ITO/*a*-BO_xN_y/ZnO/Ag during strong inversion Figure 7.1, for which a minimum criterion when; $V_s = 2\phi_f$ can be applied. We have estimated from the equation:

$$W_{max} = \left\{\frac{2\epsilon_s (2\phi_f)}{eN_d}\right\}^{0.5} \text{ and } \phi_f = V_t \ln\left(\frac{N_d}{N_i}\right)$$

[a thickness for ZnO to achieve complete inversion is $t_{ZnO} \leq 37$ nm]

where W_{max}: Space Charge Layer, V_s: Surface potential, ϕ_f: Fermi Potential, N_d: Extrinsic Carrier Concentration = 10^{18}cm^{-3}, N_i: Intrinsic Carrier Concentration < 10^6 cm^{-3}, ϵ_s: permittivity of semiconductor = 8.66(8.85×10^{-14}) F/cm, *e*: charge of electron, V_t: thermal voltage = k_BT/e = 0.026 V, k_B: Boltzmann Constant and *T* is Temperature in Kelvin.

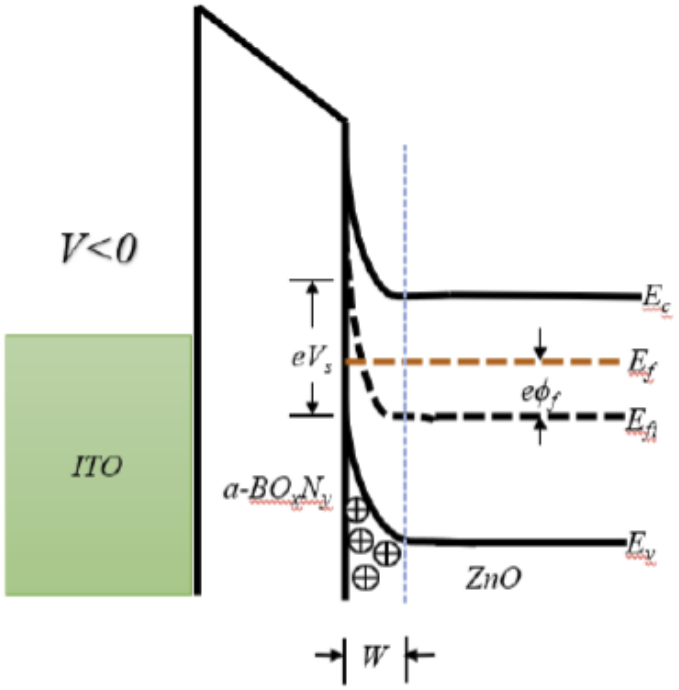

Figure 7.1: Schematics of Inversion mode in ITO/ *a*-BO_xN_y /ZnO MIS Structure.

Using relation: $C_i = C_{acc} = \varepsilon_{BON}\varepsilon_o A/t_{BON}$; where C_i = Insulator Capacitance, C_{acc} = Capacitance at accumulation, ε_{BON} = Dielectric constant BN, ε_o = Permittivity in vacuum, A = contact area, t_{BON} = thickness of *a*-BO_xN_y. We look at an MIS capacitor of 15 mTorr grown BN with a thickness of ≈35 nm and ZnO thickness of ≈22 nm. MIS structures consisting of ITO/*a*-BO_xN_y/ZnO/Ag stacks were then fabricated to evaluate the interface trap concentration and interface state density using C-V and G-V measurements. C-V and G-V were measured at an AC oscillation of 20 mV at a 100 kHz frequency. The *a*-BO_xN_y films grown at 15 mTorr were studied because this processing condition exhibited the highest breakdown strength and smoothest surface topography as discussed above.

Figure 7.2 shows an AFM image of ZnO RF sputtered of *a*-BO_xN_y which supports low temperature grown ZnO films are nanoparticles. The surface morphology is consistent with low energetics sputtering of ZnO films on glass substrates as reported in chapter 4.

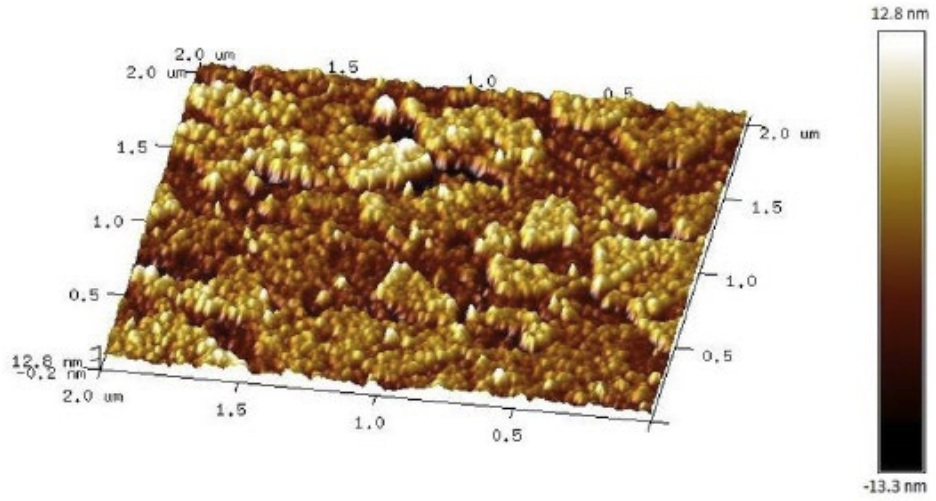

Figure 7.2: AFM Images of ZnO RF sputtered on *a*-BO_xN_y.

As stated earlier, the *a*-BO_xN_y layer was ~34 nm. The interface trap concentration (N_{it}) was calculated using,

$$N_{it} = \frac{C_i \Delta V_f}{eA},$$

while the interface state density (N_{ss}) was calculated from,

$$N_{ss} = \frac{2}{eA}\left[\frac{G_{m\,Max}/_{W}}{\left(G_{m\,Max}/_{W C_i}\right)^2 + \left(1 - C_m/_{C_i}\right)^2}\right]$$

using the Hill and Coleman approximation method [1] where the maximum value of parallel conductance (G_{mMax}) and its corresponding capacitance (C_m) is taken from the measurements (Figure 7.3d), and C_i is taken to be the insulator capacitance in accumulation (Figure 7.3a). The approximate has a 25 – 30% error. In the preceding, A = contact area, e = the electron charge, and ΔV_f = shift in flat band voltage. Biasing from -2 V to 5 V (fig 3a) and then back to -2 V (Figure 7.3b) and a normalized plot as is shown in fig. 3 (c), revealed a ΔV_f of 0.1 V. This positive shift is influenced by negative fixed charges at the bulk of the insulator or the *a*-BO_xN_y/ZnO interface [2] resulting in calculated interface trap concentration $N_{it} = 7.3 \times 10^{10}$ cm^{-2}.

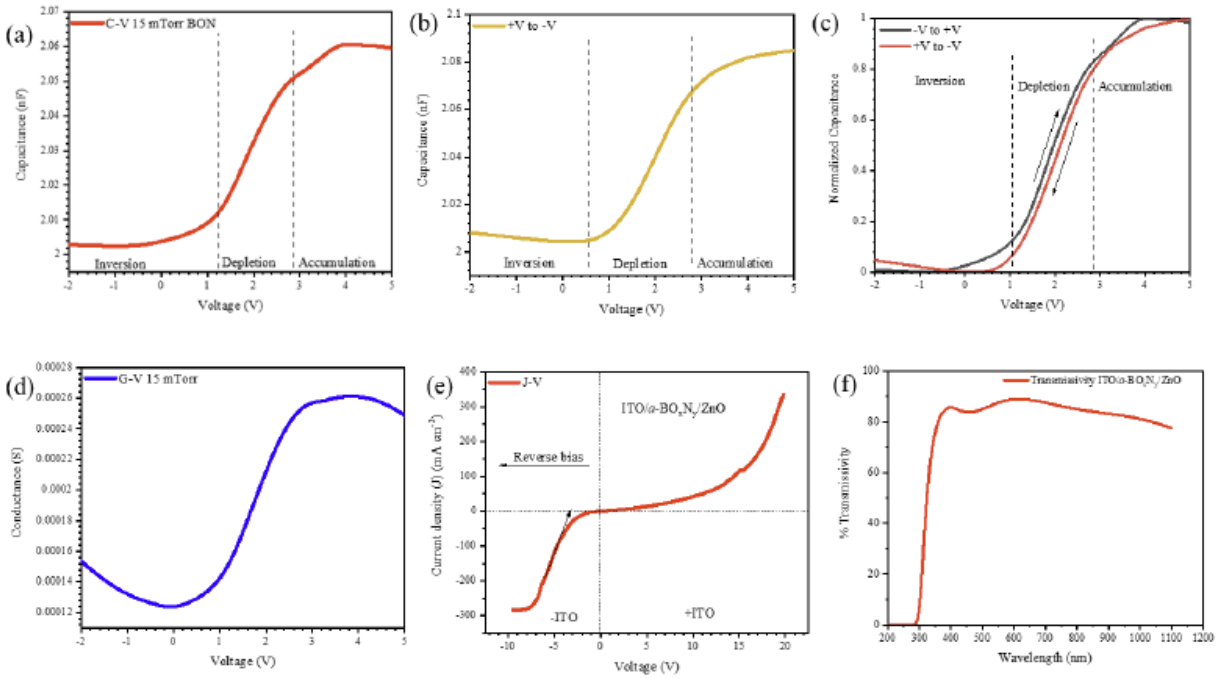

Figure 7.3: (a)-2 to +5 V, and (b) +5 to -2 V, 3 (c) normalized (a) and (b) C-V measured at 100 kHz, 20 mV AC oscillation, (d) is the corresponding G-V curve for (a), (e) I-V characteristics, (f) transmissivity of ITO/*a*-BO_xN_y/ZnO.

This value falls within the range: $7 \times 10^{11} - 5 \times 10^{9}$ cm^{-2} reported for SiO_2/Si interface [3]. Also, with a maximum parallel conductance value of 0.00026 S from Figure 7.3(c) and a corresponding capacitance value of 2.05 nF, the calculated interface state density $N_{ss} = 7.5 \times 10^{12}$ eV^{-1} cm^{-2}. An interface state density $N_{ss} = 1.1 \times 10^{12}$ eV^{-1} cm^{-2} at a C-V, G-V frequency of 500 kHz. These values compare to $10^{11} - 10^{12}$ eV^{-1} cm^{-2} in Au/BN/InP [2,4,5] MIS structures grown by plasma-enhanced vapor chemical deposition at 320ºC, and $10^{11} - 10^{13}$ eV^{-1} cm^{-2} in Al/SiO_2/p-Si assemblies for SiO_2 grown by dry oxidation at 900ºC [6], or RF sputtering SiO_2 [7]. Comparable values of reported suggest that in transistor application, *a*-BO_xN_y/ZnO structure will operate with similarities as already established SiO_2 or related BN-based structure. Also, a minimal to no shift in flat band voltage improves transistors' reliability by diminishing current leakages, power consumption, etc. Roughly 2 V was required to switch the *a*-BO_xN_y/ZnO interface from inversion to accumulation. We expect that reducing the free carrier concentration

of the ZnO layer would decrease the voltage to transition from inversion to accumulation. A plot of current density vs voltage shown in Figure 7.3(e) depicts rectifying behavior with a reverse bias breakdown strength of ~3.5 V. Figure 7.3(f) reveals the transmissivity of the ITO/*a*-BO_xN_y/ZnO stack was ~85% in the visible spectral range and as well span to 1100 nm near-infrared region. Transmissivity of this value depicts high see-through in application to transparent electronics.

7.3 ITO/*a*-BO_xN_y/WS_2/Ag MIS Structures

Figure 7.4 (a) and (d) show electrical characterizations of ITO/*a*-BO_xN_y/WS_2/Ag MIS structures of p and n WS_2 channels respectively. Hall measurement shows a carrier concentration of 8.60 x 10^{11} cm^{-2} and 1.47 x 10^{13} cm^{-2} for the n and p-channel respectively. Capacitance and conductance measurements were done at 100 kHz and an AC oscillation of 20 mV. From Figure 7.4 (a) and (d), Capacitance – Voltage (C – V) measurement shows regions transitioning from accumulation to inversion typical to an MIS capacitor. Approximately 4 V is required to switch from inversion to accumulation in n and p-channel MIS structures. A ΔV_f = 0.3 V shift was observed from C - V curves were from ITO/*a*-BO_xN_y/WS_2/Ag MIS structures. An interface trapped charge concentration (N_{it}) of 3.2 × 10^{10} and 1.6 × 10^{12} were calculated using n and p WS_2 respectively. Interface state densities (N_{ss}) of 1.6 × 10^{12} eV^{-1} cm^{-2} and 6.5 × 10^{12} eV^{-1} cm^{-2} was calculated for n and p-channel MIS structure respectively. Figure 7.4 (b) and (e) show the normalized capacitance for voltage sweep from -V to +V and vice versa for p and n WS_2 respectively. The low value shift of ΔV_f = 0.3 V is likely attributed to the nature of the BN-base insulators free of dangling bonds [8]. Figure 7.4 (c) and (f) depict the current density vs voltage (J-V) characteristics which confirm rectifying behavior. A reverse bias of these structures from 0 V shows a breakdown strength of 3.8 V and 2.5 V for p and n type WS_2 channel materials.

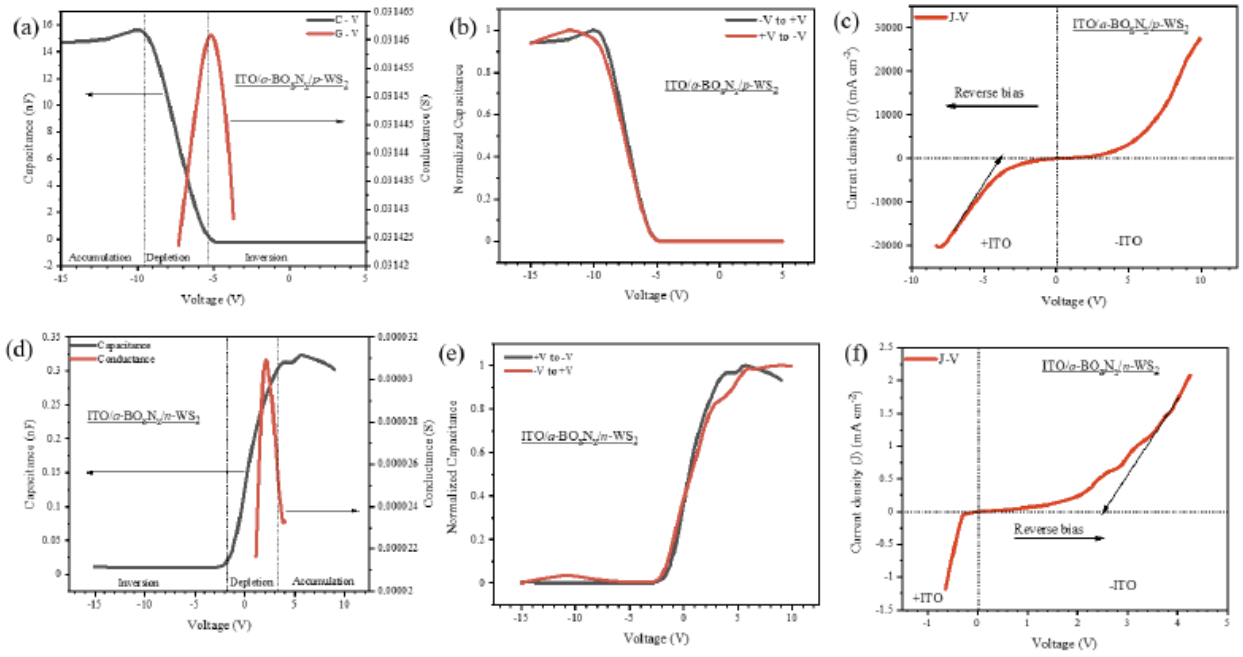

Figure 7.4: Electrical data of ITO/*a*-BO_xN_y/WS_2/Ag structure, (a),(d) C-V, G-V (b),(e) Normalized C-V for +V to -V sweep and vice versa (c),(f) Current/Voltage characteristic .

7.4 Comparison of ITO/*a*-BO_xN_y/ZnO/Ag and ITO/*a*-BN/WS_2/Ag MIS Structure

Table 7.1 shows the comparison of *a*-BO_xN_y based MIS structure using ZnO and WS_2. The result shows overall low trapped charges and interface states. This is likely due to diminished dangling bonds present at the *a*-BO_xN_y and as well in WS_2 as reported in the literature [9]. Studies have shown that dangling bonds serve as charge trapping centers [10].

Table 7.1: Comparison of ITO/*a*-BO_xN_y/ZnO/Ag and ITO/*a*-BN/WS_2/Ag MIS Structure

Channel Type	Switch from Accumulation to Inversion (V)	Trapped/Oxide Charge Conc. N_{it} (cm^{-2})	Interface state density. N_{ss} (eV^{-1} cm^{-2})
n - ZnO	2	7.3×10^{10}	7.5×10^{12}
n - WS_2	4	3.2×10^{10}	1.6×10^{12}
p - WS_2	4	1.6×10^{12}	6.5×10^{12}

7.5 Conclusion

a-BO_xN_y base MIS structure shows good enough transparency for device fabrication.

Overall low trap and density of state. WS_2 used as channel material has a lower N_{ss} value as compared to ZnO. Results of ITO/*a*-BO_xN_y/ZnO/Ag and ITO/*a*-BN/WS_2/Ag MIS Structure show promising potential in transparent and thin-film transistors.

7.6 References

[1] H. W.A., C. C.C., A single-frequency approximation for interface-state density determination, Solid. State. Electron. 23 (n.d.) 987–993. https://doi.org/10.1016/0038-1101(80)90064-7.

[2] B. A., van der P. P. J., B. J. G. M., S. J., L. B., Plasma enhanced chemical vapor deposition and characterization of boron nitride gate insulators on InP, J. Appl. Phys. 70 (1991) 4366–4370. https://doi.org/10.1063/1.349118.

[3] S. N., S. M., H. M., K. A., S. T., Improvement of SiO2/Si interface by low-temperature annealing in wet atmosphere, Appl. Phys. Lett. 66 (n.d.) 2107–2109. https://doi.org/10.1063/1.113918.

[4] K. A., B. A., L. E., An improved high frequency CV method for interface state analysis on MIS structures, Solid. State. Electron. 41 (n.d.) 635–641.

[5] B. A., B. O., B. M., L. B., V. der P. P. J., S. J., Plasma enhanced chemical vapour deposition of boron nitride onto InP, Thin Solid Films. 241 (n.d.) 278–281.

[6] T. A., A. Ş, B. M. M., Temperature and frequency dependent electrical and dielectric properties of Al/SiO2/p-Si (MOS) structure, Microelectron. Eng. 81 (n.d.) 140–149.

[7] X. Hong, H. Shihua, Frequency and voltage dependency of interface states and series resistance in Al/SiO2/p-Si MOS structure, Mater. Sci. Semicond. Process. 13 (n.d.) 395–399.

[8] D. Cory R., Y. Andrea F., M. Inanc, L. Chris, W. Lei, S. Sebastian, W. Kenji, T. Takashi, K. Phillip, S. Kenneth L., Boron nitride substrates for high-quality graphene electronics, Nat. Nanotechnol. 5 (n.d.) 722–726.

[9] R. Wu, Q. Tao, W. Dang, Y. Liu, B. Li, J. Li, B. Zhao, Z. Zhang, H. Ma, G. Sun, X. Duan, X. Duan, R. Wu, W. Dang, J. Li, B. Zhao, Z. Zhang, H. Ma, G. Sun, X. Duan, Q. Tao, Y. Liu, B. Li, FULL PAPER www.afm-journal.de 1806611 (1 of 7) van der Waals Epitaxial Growth of Atomically Thin 2D Metals on Dangling-Bond-Free WSe 2 and WS 2, (2019). https://doi.org/10.1002/adfm.201806611.

[10] M. Choi, A. Janotti, C.G. Van De Walle, Native point defects and dangling bonds in a-Al 2 O 3, (n.d.). https://doi.org/10.1063/1.4784114.

CHAPTER 8

CONCLUSION AND FUTURE WORK

8.1 Conclusion

The results of this work demonstrate that the PVD growth processes and properties of ZnO, WS_2, and *a*-BO_xN_y, are good candidates for the synthesis of metal-insulator-semiconductor structures using ZnO and WS_2 as channel materials. This is done by optimized growth processes and showing a capacitance-voltage switch from accumulation to inversion in ITO/*a*-BO_xN_y/ZnO and ITO/*a*-BO_xN_y/WS_2 MIS structures.

ZnO synthesized at low temperature using RF magnetron sputtering showed dependency on properties with processing conditions. Low energetic sputtering conditions for ZnO, i.e. lower sputtering power or high argon background gas, result in deposited films with increased (002) XRD orientation, films become more oxygen deficit, AFM image morphology shows smaller clusters, electrical measurements using Hall effect reveal increased carrier concentration and an increase in Burstein-Moss shift as compared to the higher energetic depositions,

Studies of *a*-BO_xN_y deposited using RF magnetron sputtering with varied nitrogen background pressure ranging 2 – 15 mTorr show that the film surface roughness improved and pinholes were eliminated as the deposition pressure increased. Analysis of the current density dependence on the electric field of the *a*-BO_xN_y films suggests field-enhanced Schottky emission and/or Frenkel-Poole emission mechanisms at lower and intermediate electric fields, while space-charge-limited conduction is observed at high fields. The highest breakdown strength obtained was 8 MV cm^{-1} for 15 mTorr process films. The 15 mTorr growth conditions also yielded the largest bandgap of 3.9 eV which was calculated using indirect transition Tauc equation from measured spectroscopic ellipsometry and UV-vis spectroscopy data.

For WS_2 films grown on both quartz and *a*-BO_xN_y at variable temperatures, the XRD analysis show (002) planes becoming more textured at 400 ^oC, In addition, AFM surface morphology images show nano-particles at lower chamber pressure. At an increased chamber pressure of 1 Torr, the formation of larger clusters of particles is observed. Chemical analysis reveals improved sulfur to tungsten ratio as pressure increases. WS_2 grown on *a*-BO_xN_y shows better chemistry and structure as compared to WS_2 on a quartz substrate.

The characterized MIS structures made with investigated ZnO and WS_2 semiconductor materials show promising properties for electronic applications. An interface trap concentration N_{it} of 7.3×10^{10} cm^{-2}, and interface state density N_{ss} of 7.5×10^{12} eV^{-1} cm^{-2} were measured for transparent ITO/*a*-BO_xN_y/ZnO MIS structures, and approximately 2 V was required to switch the *a*-BO_xN_y/ZnO interface from accumulation to inversion. Using WS_2 as channel material, approximately 4 V is required to switch from inversion to accumulation in n and p-channel MIS structure. Interface state densities (N_{ss}) of 1.6×10^{12} eV^{-1} cm^{-2} and 6.5×10^{12} eV^{-1} cm^{-2} was calculated for n and p-channel MIS structure respectively. This study shows promising potential for the application of the investigated research materials and structures in transparent electronics.

8.2 Future Work

This work has developed PVD processing conditions for ITO/*a*-BO_xN_y/ZnO and ITO/*a*-BO_xN_y/WS_2 as a potential structure for transparent electronic devices. Future work includes:

- Design and fabrication of bottom gated transparent transistors, using RF sputtered a-BOxNy as the insulator, RF sputtered ZnO, and few-layer PLD grown WS2 as channel materials.
- Incorporation of ITO/a-BOxNy/ZnO and ITO/a-BOxNy/WS2 based transistors into electronic devices.
- Further studies of ITO/a-BOxNy/ZnO and ITO/a-BOxNy/WS2 MIS structures for potential photoresponse and sensing applications.